UNIVERSITEIT VAN PRETORIA
UNIVERSITY OF PRETORIA
YUNIBESITHI YA PRETORIA
Denkleiers • Leading Minds • Dikgopolo tša Dihlalefi

A numerical study of self-sustained annealing

by

Jeremiah Lethoba

Submitted in partial fulfillment of the requirements for the degree

Master of Science (Physics)

in the Faculty of Natural and Agricultural Sciences

University of Pretoria
Pretoria
June 2019

Supervisor: **Prof. P A. Selyshchev**, Co-supervisor: **Dr P M. Bokov**

Abstract

The accumulation of various defects in the material structure during its exploitation poses the most important limit on its lifetime. One of the simplest and most effective methods for restoring the nominal properties of the materials is through thermal annealing. The annealing can be both homogeneous and heterogeneous, depending on the manner in which activation occurs. It is known that, under certain conditions, the heterogeneous annealing is self-sustaining and can propagate like a travelling wave, due to a nonlinear thermal-concentration feedback.

In this study numerical modelling of the heterogeneous annealing in a finite one-dimensional geometry was performed. To this end, a finite difference solver was implemented, verified and applied in our numerical experiments. The self-sustaining annealing process was initialized by adding heat to a localized region near the material surface at the initial moment. The evolution of temperature and defect distributions during the process of annealing was obtained for different initiating heat distributions and initial defect concentrations.

It was demonstrated that for large values of initiating energy, the annealing process develops as a wave, which propagates at a constant speed. For more moderate values of initiating energy, the interplay of the heterogeneous initial heat distribution and the spontaneous annealing leads to the appearance of the wave regime in the terminal part of the process. The time required for the number of defects in the material to fall below a given small fraction of their initial value is a measure of overall efficiency of the annealing process. The dependence of this time on the initial conditions and initial heating parameters was studied.

Keywords: annealing, homogeneous annealing, heterogeneous annealing, spontaneous annealing, thermal-concentration feedback, self-sustaining annealing.

Contents

1 **Introduction** **1**
- 1.1 Research Motivation and Theory . . . 1
  - 1.1.1 Defect Annealing . . . 2
  - 1.1.2 Defect Physical Properties . . . 2
- 1.2 Research Approach and Objective . . . 3
- 1.3 Overview . . . 3

2 **Literature Review** **5**
- 2.1 Point Defects: Interstitials and Vacancies . . . 5
- 2.2 Interstitial Sites . . . 5
  - 2.2.1 Number of atoms per unit cell . . . 6
  - 2.2.2 Octahedral sites . . . 6
  - 2.2.3 Tetrahedral sites . . . 7
- 2.3 Interstitials . . . 7
- 2.4 Vacancies . . . 7
- 2.5 Line Defects: Dislocations . . . 8
- 2.6 Planar Defects . . . 8
- 2.7 Volume Defects . . . 8
- 2.8 Defect Activation and Formation Energy Estimations . . . 9
  - 2.8.1 Thermodynamics of point defect formation . . . 9
  - 2.8.2 Cavity estimation of the vacancy energy of formation . . . 11
  - 2.8.3 Defect clusters . . . 12
- 2.9 Isothermal Annealing . . . 14
  - 2.9.1 Diffusion . . . 15
  - 2.9.2 The balance equations for point defects . . . 17
  - 2.9.3 Defect density: number of defects per unit volume . . . 20
- 2.10 Adiabatic Annealing . . . 21
  - 2.10.1 Homogeneous annealing . . . 21
  - 2.10.2 Heterogeneous annealing . . . 23
- 2.11 Self-Sustained Annealing Wave . . . 25

3 **Mathematical Model of Self-Sustained Annealing** **27**

4 **Methods for the Numerical Solution of the Problem** **31**
- 4.1 Discretisation of the Model in Space . . . 31
- 4.2 Time Integration Methods . . . 32
  - 4.2.1 Euler method . . . 34
  - 4.2.2 Theta method . . . 34
  - 4.2.3 Fourth-order Runge-Kutta method . . . 34

- 4.3 Stiffness . . . 35
- 4.4 Other Tools Used for Solving the Problem . . . 35
  - 4.4.1 The Maple PDE Solver, pdsolve . . . 36
  - 4.4.2 The Python ODE Solver, odeint . . . 36
  - 4.4.3 Summary of the Maple and Python tools . . . 37
- 4.5 Verification of Numerical Solutions . . . 37

5 Results and Discussion **39**
- 5.1 Self-Sustained Annealing in a Finite Sample . . . 39
- 5.2 Annealing for a Fixed Initiating Energy . . . 41
- 5.3 Self-Sustained Annealing for Different Initiating Temperatures . . . 46
- 5.4 Dependence of the Self-Sustained Annealing on the Heating Depth . . . 50
- 5.5 Impact of the Initial Values . . . 54
- 5.6 Annealing Time and Travelling Wave Velocity . . . 58
  - 5.6.1 Annealing time in the case of the homogeneous process . . . 58
  - 5.6.2 Annealing time in the case of the heterogeneous process . . . 60
  - 5.6.3 Velocity of the travelling wave . . . 62
- 5.7 Dependence of Annealing Time on the Initial Defect Density . . . 65
- 5.8 Influence of the Boundaries on the Travelling Wave . . . 68
- 5.9 The Travelling Wave at High Initial Temperatures . . . 72

6 Conclusion **79**

List of Figures

2.1 Face-centered cubic (fcc) lattice unit cell on the left, body-centered cubic (bcc) lattice unit cell in the center and hexagonal close packed (hcp) unit cell on the right. 6
2.2 Split interstitials in the bcc lattice in the ⟨111⟩ direction (left). Split interstitials in the bcc lattice in the ⟨110⟩ direction (center). Di-interstitials in the bcc lattice in the ⟨110⟩ direction (right). 7
2.3 Exchange (on the left) and ring (on the right) mechanisms of diffusion. 16
2.4 Vacancy (on the left) and interstitial (on the right) mechanisms of diffusion. 16
2.5 Collinear variant interstitialcy mechanism of diffusion (left). Non-collinear variant interstitialcy mechanism of diffusion (right). 16
2.6 Crowdion mechanism of diffusion. 17
2.7 Schematic of time evolution of the normalized density of defects in an irradiated material, before and after irradiation at a low temperature. 19
2.8 Schematic of the time evolution of normalized defect concentration for different interaction radii, $r_{\mathrm{iv},j}$, where $j = 1, 2, 3$. As expected, when the interaction radius is increased the probability for annihilation of interstitials and vacancies increases and the defect concentration decreases faster. 20
2.9 The decrease in defect density and increase in temperature in time in the process of spontaneous and homogeneous annealing. 23

3.1 Different distributions of the annealing initiating temperature. 27

4.1 For N_p intervals, we implement a discretisation that maps the defect density and temperature values, n_j and T_j, in the middle of the j-th interval. 31
4.2 The fourth-order Runge-Kutta method extends the number of function evaluation in the Euler method. The function is evaluated once at the initial point, twice at trial midpoints and once at a trial end points. These functions are then summed to produce the final point u_{i+1} (filled dot). 35
4.3 Comparison of solutions determined with analytic formula and numerically with the RK4 method for the normalised defect density (or fraction of remaining defects) dependence on time. 37
4.4 Comparison of solutions for the temperature profile determined numerically with the Explicit Euler, Runge-Kutta (4th order) methods and the `odeint` solver. The solutions show close similarity (left) with a negligible difference (right). 38

5.1 Schematic of the annealing wave front, propagating from the annealed material with an increased temperature to the damaged material with a lower temperature. Annealing happens predominantly in the area indicated as "annealing zone" [1]. . . 40

5.2 The temperature (solid line) and defect density (dashed line) profiles for an initiating temperature increase of $\Delta T = 200$ K over a heating depth of $\Delta x = 2$ mm calculated for different transient times from $t = 0.0$ s to $t = 4.17$ s. 41

5.3 The annealing of defects (bottom) near the initiation boundary and the temperature increase (top), as a result of the positive feedback, for different initiation temperature ΔT_m and heating depth Δx_m values under the condition $\Delta x_m \Delta T_m = \Delta x_{m'} \Delta T_{m'}$. The temperature and defect density profiles are given for $t = 0.0$ ms and $t = 0.5$ ms. . . . 42

5.4 The temperature (top) and defect density profiles (bottom) with the similar annealing initiation temperature distributions of Figure 5.3. The temperature and defect density profiles are given for $t = 0.0$ ms and $t = 100.0$ ms. 43

5.5 The temperature (top) and defect density profiles (bottom) with the similar annealing initiation temperature distributions of Figure 5.3. The temperature and defect density profiles are given for $t = 0.0$ ms and $t = 500.0$ ms. 44

5.6 The temperature (top) and defect density (bottom) propagation fronts for an initiating temperature increase of $\Delta T = 80$ K, with a heating depth of $\Delta x = 2$ mm for a maximum transient time interval of 11.85 s. 47

5.7 The temperature (top) and defect density (bottom) propagation fronts for an initiating temperature increase of $\Delta T = 120$ K, with a heating depth of $\Delta x = 2$ mm, calculated for a maximum transient time interval of 11.85 s. 47

5.8 The temperature (top) and defect density (bottom) propagation fronts for an initiating temperature increase of $\Delta T = 160$ K, with a heating depth of $\Delta x = 2$ mm, calculated for a maximum transient time interval of 8.85 s. 48

5.9 The temperature (top) and defect density (bottom) propagation fronts for an initiating temperature increase of $\Delta T = 240$ K, with a heating depth of $\Delta x = 2$ mm, calculated for a maximum transient time interval of 1.85 s. 48

5.10 The temperature (top) and defect density (bottom) propagation fronts for an initiating temperature increase of $\Delta T = 280$ K, with a heating depth of $\Delta x = 2$ mm, calculated for a maximum transient time interval of 1.85 s. 49

5.11 The temperature (top) and defect density (bottom) propagation fronts for an initiating temperature increase of $\Delta T = 400$ K, with a heating depth of $\Delta x = 2$ mm, calculated for a maximum transient time interval of 1.85 s. 49

5.12 The temperature (top) and defect density (bottom) propagation fronts for an initiating temperature increase of $\Delta T = 80$ K, with a heating depth of $\Delta x = 8$ mm, calculated for a maximum transient time interval of 1.85 s. 51

5.13 The temperature (top) and defect density (bottom) propagation fronts for a temperature increase of $\Delta T = 80$ K, with a heating depth of $\Delta x = 12$ mm, calculated for a maximum transient time interval of 1.85 s. 51

5.14 The temperature (top) and defect density (bottom) propagation fronts for a temperature increase of $\Delta T = 80$ K, with a heating depth of $\Delta x = 16$ mm, calculated for a maximum transient time interval of 1.85 s. 52

5.15 The temperature (top) and defect density (bottom) propagation fronts for a temperature increase of $\Delta T = 40$ K, with a heating depth of $\Delta x = 40$ mm, calculated for a maximum transient time interval of 1.85 s. 52

5.16 The temperature (top) and defect density (bottom) propagation fronts for a temperature increase of $\Delta T = 80$ K, with a heating depth of $\Delta x = 6$ mm, calculated for a maximum transient time interval of 4.85 s. 53

5.17 The temperature (top) and defect density (bottom) propagation fronts for a temperature increase of $\Delta T = 80\,\mathrm{K}$, with a heating depth of $\Delta x = 4\,\mathrm{mm}$, calculated for a maximum transient time interval of 8.85 s. 53
5.18 Results of our calculations showing that the annealing zone decreases in width when the initial defect density is increased. 54
5.19 The temperature and defect density profiles in the annealing zone between the un-annealed and annealed regions of the sample, calculated for $T_0 = 120\,\mathrm{K}$ and $\Theta_0 = 555.96\,\mathrm{K}$. 55
5.20 The temperature and defect density profiles in the annealing zone between the un-annealed and annealed regions of the sample for $T_0 = 300\,\mathrm{K}$ and $\Theta_0 = 555.96\,\mathrm{K}$ 56
5.21 Temperature and defect density profiles when the temperature propagation front is oscillating and the initial sample temperature is 120 K. 56
5.22 Temperature and defect density profiles for front for the non-oscillating temperature propagation front and for the initial sample temperature of 300 K. 57
5.23 The temperature propagation front changes in a complex manner when the initial temperature is $T_0 = 166.67\,\mathrm{K}$ and the maximum temperature increase from annealed defects is $\Theta_0 = 333.58\,\mathrm{K}$. 57
5.24 The time evolution of the fraction of remaining defects for some initial temperatures below and above the reference value of initial temperature of 300 K. 59
5.25 The time evolution of the fraction of remaining defects for different initial homogeneous defect density distributions. Here N' denotes the number of defects in the sample at any time for different initial defect densities, N'_0, and N_0 is the reference initial number of defects. 59
5.26 The annealing time dependence on the heating depth Δx for different initiation temperatures and for a sample of length $L = 13\,\mathrm{cm}$. 61
5.27 A zoom-in of Figure 5.26 at heating depths between 4 mm and 14 mm. 61
5.28 Schematic of annealing wave fronts, propagating from the annealed material to the damaged material in the travelling wave regime. 62
5.29 The time evolution of the fraction of remaining defects (left) and the corresponding obsolute time change of the fraction of remaining defects (right) with initiation temperature $\Delta T = 280\,\mathrm{K}$ and heating depth $\Delta x = 4\,\mathrm{mm}$ for a sample of length $L = 13\,\mathrm{cm}$. 63
5.30 The time evolution of the fraction of remaining defects for different initiating temperatures at a heating depth $\Delta x = 4\,\mathrm{mm}$ in a sample of length $L = 13\,\mathrm{cm}$ 64
5.31 The time evolution of the fraction of remaining defects in a sample of length $L = 13\,\mathrm{cm}$ when the heating depth is increased in the travelling wave regime . The initiating temperature for the experiment is $\Delta T = 200\,\mathrm{K}$. 64
5.32 The defect annealing times for different initial defect densities. The reference value is $n_0^{\mathrm{ref}} = 6.63 \times 10^{26}$ defects/m^3. 65
5.33 The evolution of the fraction of remaining defects in time for two different initial defect densities, n_0^{ref} and $2n_0^{\mathrm{ref}}$, with $n_0^{\mathrm{ref}} = 6.63 \times 10^{26}$ defects/m^3. 67
5.34 The temperature (top) and defects density (bottom) propagation fronts for a temperature increase of $\Delta T = 200\,\mathrm{K}$, with a heating depth of $\Delta x = 40\,\mathrm{mm}$ for a maximum transient time interval of 3.06 s. 68
5.35 The time evolution of the fraction of remaining defects in the sample for the initiation parameters, $\Delta x = 40\,\mathrm{mm}$ and $\Delta T = 200\,\mathrm{K}$, (left) and the zoom-in of the fraction of remaining defects in the first 16 ms of the transient (right). 69

5.36 The initial moments of the transient at the initiation region for the temperature (top) and defects density (bottom) profiles for a temperature increase of $\Delta T = 200\,\mathrm{K}$, with a heating depth of $\Delta x = 40\,\mathrm{mm}$ and at a maximum transient time interval of 15 ms. 70

5.37 A zoom-in of the fraction of remaining defects at the right boundary of the sample in the last seconds before the annealing time is reached (right). 70

5.38 A zoom-in of the fraction of remaining defects in the first few milliseconds of the transient(top). A zoom-in of the fraction of remaining defects before the annealing time is reached (bottom). 71

5.39 The temperature (top) and defect density (bottom) propagation fronts for initiating parameters $\Delta T = 300\,\mathrm{K}$ and $\Delta x = 2\,\mathrm{mm}$ for a maximum time of 3.85 s with regular time intervals between successive profiles of $\Delta t = 0.160\,\mathrm{s}$. The initial temperature is $T_0 = 300\,\mathrm{K}$. 73

5.40 The temperature (top) and defect density (bottom) propagation fronts for initiating parameters $\Delta T = 300\,\mathrm{K}$ and $\Delta x = 2\,\mathrm{mm}$ for a maximum time of 3.4 s with regular time intervals between successive profiles of $\Delta t = 0.142\,\mathrm{s}$. The initial temperature is $T_0 = 310\,\mathrm{K}$. 74

5.41 The temperature (top) and defect density (bottom) propagation fronts for initiating parameters $\Delta T = 300\,\mathrm{K}$ and $\Delta x = 2\,\mathrm{mm}$ for a maximum time of 3.0 s with regular time intervals between successive profiles of $\Delta t = 0.125\,\mathrm{s}$. The initial temperature is $T_0 = 320\,\mathrm{K}$. 74

5.42 The temperature (top) and defect density (bottom) propagation fronts for initiating parameters $\Delta T = 300\,\mathrm{K}$ and $\Delta x = 2\,\mathrm{mm}$ for a maximum time of 2.35 s with regular time intervals between successive profiles of $\Delta t = 0.097\,\mathrm{s}$. The initial temperature is $T_0 = 330\,\mathrm{K}$. 75

5.43 The temperature (top) and defect density (bottom) propagation fronts for initiating parameters $\Delta T = 300\,\mathrm{K}$ and $\Delta x = 2\,\mathrm{mm}$ for a maximum time of 1.5 s with regular time intervals between successive profiles of $\Delta t = 0.062\,\mathrm{s}$. The initial temperature is $T_0 = 340\,\mathrm{K}$. 75

5.44 The temperature (top) and defect density (bottom) propagation fronts for initiating parameters $\Delta T = 300\,\mathrm{K}$ and $\Delta x = 2\,\mathrm{mm}$ for a maximum time of 1.2 s with regular time intervals between successive profiles of $\Delta t = 0.05\,\mathrm{s}$. The initial temperature is $T_0 = 345\,\mathrm{K}$. 76

5.45 The temperature (top) and defect density (bottom) propagation fronts for initiating parameters $\Delta T = 300\,\mathrm{K}$ and $\Delta x = 2\,\mathrm{mm}$ for a maximum time of 1.0 s with regular time intervals between profiles of $\Delta t = 0.042\,\mathrm{s}$. The initial temperature is $T_0 = 350\,\mathrm{K}$. 76

5.46 The temperature (top) and defect density (bottom) propagation fronts for initiating parameters $\Delta T = 300\,\mathrm{K}$ and $\Delta x = 2\,\mathrm{mm}$ with regular time intervals of $\Delta t = 0.307\,\mathrm{s}$ between successive profiles (left). The corresponding fraction of remaining defects for the heterogeneous and homogeneous (and spontaneous) annealing cases (right). The initial temperature is $T_0 = 310\,\mathrm{K}$ and sample length is $L = 26\,\mathrm{cm}$. 77

5.47 The temperature (top) and defect density (bottom) propagation fronts for initiating parameters $\Delta T = 300\,\mathrm{K}$ and $\Delta x = 2\,\mathrm{mm}$ with regular time intervals of $\Delta t = 0.307\,\mathrm{s}$ between successive profiles (left). The corresponding fraction of remaining defects for the heterogeneous and homogeneous (and spontaneous) annealing cases (right). The initial temperature is $T_0 = 310\,\mathrm{K}$ and sample length is $L = 39\,\mathrm{cm}$. 78

5.48 The temperature (top) and defect density (bottom) propagation fronts for initiating parameters $\Delta T = 300\,\mathrm{K}$ and $\Delta x = 2\,\mathrm{mm}$ with regular time intervals of $\Delta t = 0.307\,\mathrm{s}$ between successive profiles (left). The corresponding fraction of remaining defects for the heterogeneous and homogeneous (and spontaneous) annealing cases (right). The initial temperature is $T_0 = 310\,\mathrm{K}$ and sample length is $L = 52\,\mathrm{cm}$. 78

List of Tables

3.1 Values of parameters used in our study. 29

5.1 Energy values for different initiation parameters: the study of the dependence of the self-sustained annealing on the initiating temperature for a given heating depth. 46
5.2 Energy values for different initiation parameters: the study of the dependence of the self-sustained annealing on the heating depth for given initiating temperatures. . 50
5.3 Initial temperature and the corresponding annealing times of the spontaneous homogeneous annealing and the activated heterogeneous annealing. 73

Acknowledgements

I would like to express my gratitude to my supervisors Prof. P.A. Selyshchev and Dr P.M. Bokov for introducing me to the subject of my dissertation and their expertise advice that helped to produce a rigorous analysis of my results. I would also like to thank the Department of Physics at the University of Pretoria for funding me to attend the conference for my conference paper. Last but not least I would like to thank my friends who work at Necsa in the Radiation and Reactor Theory group department for giving me free lifts to see my supervisor in the department; and Necsa for offering me Internet and PC services.

Nomenclature

Physical constants

Boltzmann constant: $k_B = 8.617 \times 10^{-5}$ eV/K

Elementary charge: $e = 1.602 \times 10^{-10}$ C

Reduced Planck constant: $\hbar = 1.054 \times 10^{-34}$ J s

Abbreviations

BCC body-centred cubic lattice

BD Backward Difference

CD Central Difference

EEM Explicit Euler Method

FCC face-centred cubic lattice

FD Forward Difference

IEM Implicit Euler Method

HCP hexagonal close packed lattice

IRK4 Implicit Runge-Kutta method of 4th order

ODE Ordinary Differential Equation

PDE Partial Differential Equation

RK4 explicit Runge-Kutta method of 4th order

Notations

a interatomic distance or lattice unit cell side length

A pre-exponential factor, equal to the lifetime of the cluster with zero binding energy

b Burgers vector

C_i concentration of interstitials

C_s concentration of sinks

C_v concentration of vacancies

D diffusion coefficient

D_i diffusion coefficient for interstitials

D_v diffusion coefficient for vacancies

E_a defect activation energy

E_a^i activation energy of interstitials

E_a^v activation energy of vacancies

E_f^b1 binding energy of a defect cluster with one interstitial

E_f^i energy of formation of interstitials

E_f^v energy of formation of vacancies

E_m^i migration energy of interstitials

E_m^v migration energy of vacancies

F Helmholtz free energy

G Gibbs free energy

h_x mesh size in spatial discretisation

H enthalpy

j index of a spatial interval: $j = 1, 2, \ldots, N_p$

k_L dislocation core

K_0 rate of production of defects

K_iv interstitial-vacancy recombination rate coefficient

K_is interstitial-sink recombination rate coefficient

K_vs vacancy-sink recombination rate coefficient

L sample length

n_0 initial defect density

n defect density in time and space

n^e equilibrium density of defects

N_0 total number of defects in the sample at $t = 0$

N number of defects in time

N_p number of intervals in a spatial mesh

N_s number of defect sites

r_a radius of a particular atom

r_0 atom displacement radius from a dislocation loop

r_iv interstitial-vacancy interaction radius

R radius of a dislocation loop or of a cavity

S entropy

t time

Δt time step size in temporal discretisation

T_0 initial value of temperature

T temperature in time and space

v propagation speed of travelling wave

V_i dilatational volume of interstitials

V_v dilatational volume of vacancies

w statistical weight

x position in space

Δx heating depth

α_k growth rate coefficient of a k-cluster

θ energy released per annealing of one defect

Θ_0 maximum thermal contribution from annealed defects

Θ thermal contribution from annealed defects in time

σ surface energy per unit area

ω_E natural angular frequency

ω_r vibration angular frequency

Ω atomic volume of a defect

Chapter 1

Introduction

1.1 Research Motivation and Theory

Over the service lifetime of structural materials, their properties deteriorate as a result of the formation of various defects in their crystal structure. Defects are formed under both steady and cyclic load, and under the influence of thermal and radiation exposure. The irradiation of a material with high-energy particles causes the formation of different types of defects in its crystalline lattice which affect the physical properties of the material. The defects that are generated by irradiation require a high energy of formation which means that their thermal generation is highly improbable. In cases where the physical properties of the material need to be maintained like, for example, materials that are involved in the operation of a nuclear facility, a mechanism for the restoration of the material properties is necessary.

One of the simplest and most effective methods for restoring the nominal properties of materials is through thermal annealing. Different types of defects are annealed at different temperatures, and the annealing rate increases strongly with temperature. Since the crystal with defects has increased energy, this energy is converted into thermal energy during the annealing of defects. This leads to an increase in the temperature of the material and acceleration of annealing. Thus, a thermal-concentration feedback is formed. Due to this thermal-concentration feedback, the annealing of defects can be carried out in various ways.

A common way of recovering the damaged material is by thermal annealing where the sample is heated, usually, by increasing the surface temperature of the sample and keeping it constant for some time [2]. This method of annealing, however, may come at a high cost of energy that may be required to anneal large samples and to maintain a homogeneous temperature distribution. To this end, a more efficient method of annealing is required. One of these is spreading self-sustaining annealing (also referred to as quasi-wave mode).

The present work is devoted to the numerical simulation of the self-sustained annealing, and the study of the influence of characteristics of the model such as the parameters of initiation of the quasi-wave mode, the initial density of defects, the formation energy of defects, etc. on its parameters, including propagation velocity and the shape of the wave front. The travelling wave of annealing has been studied in [3] and is referred to as the autowave. The studied model in [3] considers the propagation of the wave in an infinite sample with a uniform initial density of defects at absolute zero temperature. In our numeric simulations we consider the initiation of the wave in a sample in the form of a slab of finite length in one dimension and infinite length in lateral directions and we consider a base initial sample temperature at room temperature (300 K). In our sample the travelling wave is initiated by means of a thermal pulse which is achieved by increasing the temperature of the sample uniformly in a localised region of the sample at the boundary.

Since the initial temperature of sample is considered to be above absolute zero and the defect annealing rate is temperature dependent, the spontaneous annealing process takes place in the sample. If the initial temperature is high enough this spontaneous annealing may result in significant damping of the travelling wave. We also study this damping effect and at high initial temperatures.

1.1.1 Defect Annealing

Annealing is a set of relaxation processes leading to the restoration of the original properties of the material. These processes are thermally activated and the relaxation rate depends strongly on temperature. Since in practice material have a temperature above absolute zero, the annealing process will occur any time after or during irradiation. After irradiation, the radiation-induced material condition starts to relax toward equilibrium.

For defects to anneal, they must be provided with a specific amount of energy (depending on the defect type) which is referred to as the *activation energy*. However at a sufficiently low crystal temperature (after irradiation) the probability for a defect to obtain an energy amount that is comparable to the activation energy of the defect is very small, and annealing does not occur [3]. The state of the material after irradiation, in this case, remains metastable.

1.1.2 Defect Physical Properties

In our study we restrict our investigation to irradiation-induced defects in metals and consider the activation energy within the typical range. The physical properties of the defects depend on the types of metals (or alloys) that host them; the defect properties include their migration energy, their formation energy and their activation energy. These properties can be determined experimentally or numerically by computer simulations. When the defects anneal, they release an energy that is similar to their formation energy.

One example of the experimental determination of the defect physical properties is by *isochronous* annealing of the irradiation induced defects where the sample is subjected to different increasing temperature values for, usually, long periods of time [3]. The isochronous annealing experiment involves six sequential stages of annealing, namely: Stage I, which is associated with the recombination of Frenkel pairs (a type of point defect), which are located at small distances from each other, because of the mobility of interstitial atoms. Stage II, is associated with the movement of interstitial atoms to more distant sinks (such as grain boundaries, dislocations, dislocation loops, pores). Stage III is associated with the processes of defect cluster decay such as the release of interstitial atoms from impurity traps, these could be formed during Stage I or during the irradiation. Stage IV corresponds to the beginning of the migration of vacancies to sinks and the formation of vacancy clusters. Stage V is associated with the recrystallization process which involves an intensive migration of vacancies to the surface of the material. Stage VI annealing is detected in the melting temperature factor ranges of between 0.4 and 0.53, for bcc (body centred cubic) lattice structures, and between 0.33 and 0.45, for fcc (face centred cubic) lattice structures, when studying the change of strength characteristics in the process of annealing of irradiated metals. The activation energy of the annealing process in Stage VI is close to the activation energy of recrystallization of the metal. The activation energy of any particular process (migration of defects or defect cluster decay, for example) is identified, conventionally, by considering the temperature at which a change in a particular characteristic is observed.

1.2 Research Approach and Objective

Metals are heat conducting materials with a high thermal conductivity. The rate of heat transfer depends on the thermal conductivity. The transfer of heat leads to an increase of the temperature in the rest of the irradiated sample. The temperature increase caused a growth of the annealing rate. The temperature is further increased as a result of the thermal energy released by defects when they anneal, this positive feedback is referred to as the *thermal concentration feedback*.

In our study we take advantage of these two properties (thermal conductivity and the thermal concentration feedback) to device a way of annealing the defects in a metal that involves only heating of a localized region of the metal by means of a thermal pulse. With the right conditions, a *self-sustained annealing* wave may develop after some time during the annealing initiation process. By way of a numerical method, we diagnose the development of the self-sustained annealing wave (or travelling wave) and study the annealing time dependence on the annealing initiation distribution and on the defect density. From the annealing time the speed of annealing wave can also be determined.

1.3 Overview

In Chapter 2 we review the literature of irradiation induced defects and the derivation of their physical properties. We also review the existing analytic model for the self-propagating and self-sustained annealing wave. In Chapter 3 we provide a detailed explanation of the research approach and objective and we model the problem mathematically. In Chapter 4 we go through the detail of the numeric method used to produce our results and we discuss the results in Chapter 5. Finally, we conclude our study and discuss possible improvements to our model.

Chapter 2

Literature Review

Defects in a material can have enhancing properties, that make the material fit for a specified use, or they can have degrading effects. There are various types of defects that exist in a crystalline lattice and they are classified according to their dimensions D as follows:

- Point defects (0D): vacancies and interstitials;
- Line defects (1D): dislocation lines;
- Planar defects (2D): dislocation loops;
- Volume defects (3D): voids, bubbles, stacking fault tetrahedra.

In this chapter we review a theoretical background of the different types of defects in metals, we investigate the thermodynamics of their formation; their temporal and spatial dependence. We also review their formation into clusters and their interaction as clusters. Lastly, we review literature about the time, spatial and temperature dependence of the defects and several conditions under which they can anneal. Much of the theory review in this section is referenced from the work of Was, *Fundamentals of Radiation Materials Science*, 2007 and Selyshchev and Bokov, *Kinetics of Annealing: Basic relationships and nonlinear effects*, 2018.

2.1 Point Defects: Interstitials and Vacancies

Interstitial atoms or *interstitials* occur at positions in the crystal called *interstitial sites*. There are different number of sites for different lattice structures. In this section we introduce the number of sites for different lattice structures in metals and the different configuration of the interstitials and vacancies.

2.2 Interstitial Sites

Interstitial sites are irregular lattice positions that can be occupied by atoms called interstitial atoms or interstitials. For cubic crystal lattices, there are two broad classifications of interstitial sites, namely octahedral and tetrahedral sites [4]. An example of cubic crystal lattices is the fcc (face-centred cubic) lattice, shown in Figure 2.1 (left), which is cubic and is spanned by a unit cell of constant length with atoms located at the corners and faces of the cube.

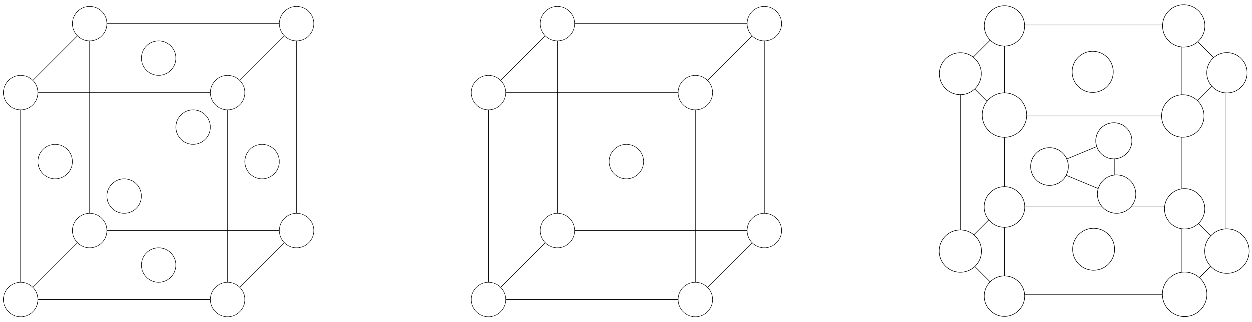

Figure 2.1: Face-centered cubic (fcc) lattice unit cell on the left, body-centered cubic (bcc) lattice unit cell in the center and hexagonal close packed (hcp) unit cell on the right.

2.2.1 Number of atoms per unit cell

FCC lattice. The number of atoms per unit cell in an fcc structure is 4 and it is calculated as follows:

$$\frac{\text{no. of corner atoms}}{\text{no. of unit cells sharing corner atoms}} + \frac{\text{no. of face atoms}}{\text{no. of unit cells sharing face atoms}} = \frac{8}{8} + \frac{6}{2} = 4. \tag{2.1}$$

BCC lattice. Another example of a cubic lattice is the bcc lattice, Figure 2.1 (center). In the bcc lattice, the number of atoms per unit cell is 2 and it is calculated as follows:

$$\text{no. of centre atoms} + \frac{\text{no. of corner atoms}}{\text{no. of unit cells sharing corner atoms}} = 1 + \frac{8}{8} = 2. \tag{2.2}$$

HCP lattice. The hcp lattice, Figure 2.1 (right), is an example of a hexagonal crystal lattice and the hcp unit cell is defined by the h/a ratio where a is the length of a side of a regular hexagon and h is the cell height. The number of atoms per unit cell in the hcp lattice is 6 and is calculated as follows:

$$\begin{aligned} &\frac{\text{no. of corner atoms}}{\text{no. of unit cells sharing corner atoms}} + \frac{\text{no. of face atoms}}{\text{no. of unit cells sharing face atoms}} \\ &\qquad + \text{ no. of atoms per unit cell} = \frac{12}{6} + \frac{2}{2} + 3 \times 1 = 6. \end{aligned} \tag{2.3}$$

2.2.2 Octahedral sites

Octahedral sites are, according to [4], interstitial positions that are surrounded by an octahedron where the lattice atoms make up the six vertices of an octahedron.

FCC lattice. The number of octahedral sites per unit cell in the fcc lattice, the centre of the unit cell and in the edges are calculated as follows:

$$\text{no. of octahedral sites at the centre} + \frac{\text{no. of edge sites}}{\text{no. of unit cells sharing octahedral sites}} = 1 + \frac{12}{4} = 4. \tag{2.4}$$

BCC lattice. For the bcc lattice, the number of octahedral sites per unit cell is calculated as follows:

$$\frac{\text{no. of faces}}{\text{no. of octahedral sites per face}} + \frac{\text{no. edges}}{\text{no. of octahedral sites per edge}} = \frac{6}{2} + \frac{12}{4} = 6. \tag{2.5}$$

HCP lattice. The hpc lattice unit cell has 6 octahedral sites, all wholly contained in the unit cell.

2.2.3 Tetrahedral sites

FCC lattice. The fcc lattice unit cell has 8 tetrahedral interstitial sites (one for each corner atom). They are located inside a tetrahedron formed by lattice atoms.

BCC lattice. A bcc lattice has 12 tetrahedral interstitial sites calculated as follows:

$$\frac{\text{no. of faces } \times \text{no. of locations per face}}{\text{no. of tetrahedral sites per face}} = \frac{6 \times 4}{2} = 12. \tag{2.6}$$

HCP lattice. The hpc lattice unit cell has 6 tetrahedral sites, four of which are wholly contained in the unit cell.

2.3 Interstitials

In true physical configurations extra atoms called self-interstitial atoms can crowd interstitial voids. The result is a stable configuration called a dumbbell or split-interstitial configuration where two atoms are associated with a single lattice site. The atom cores repel each other and arrange themselves in the lowest energy orientation. For the bcc lattice the lowest energy configuration is the split-interstitial configuration axis along the ⟨110⟩ direction, Figure 2.2 (center).

The agglomeration of mobile self-interstitial atoms at elevated temperatures results in the formation of multiple interstitials that have a high binding energy, of order 1 eV [4]. The mobile self-interstitials can be trapped by impurity atoms. The binding energy of self-interstitial-impurity atoms are of order 0.5 eV to 1 eV. The interstitial-impurity complexes dissociate thermally at temperatures where vacancies become mobile.

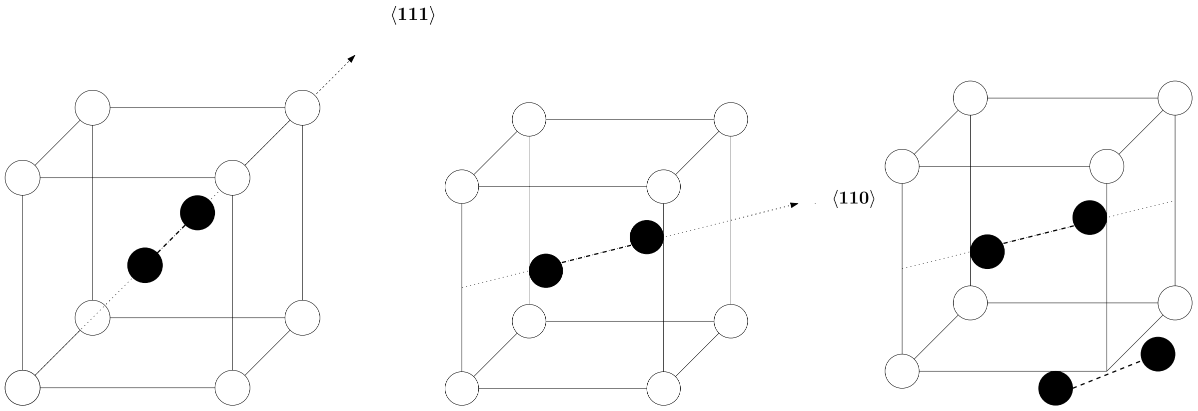

Figure 2.2: Split interstitials in the bcc lattice in the ⟨111⟩ direction (left). Split interstitials in the bcc lattice in the ⟨110⟩ direction (center). Di-interstitials in the bcc lattice in the ⟨110⟩ direction (right).

2.4 Vacancies

Vacancies are missing lattice atoms. Computer simulations and calculations have shown that adjacent or nearest neighbour atoms to a vacancy relax inward toward a vacancy. This indicates a higher migration energy of vacancies ($> 0.5\,\text{eV}$) compared to that of interstitials ($> 0.5\,\text{eV}$). Therefore, the vacancies are less mobile than self-interstitials. Multiple vacancies are often observed in irradiated metals and have a lower binding energy (< 0.1 eV) compared to interstitial clusters [4].

2.5 Line Defects: Dislocations

Dislocations occur as a result of abrupt changes in the regular ordering of atoms in a line [5, 6]. Their density is high and they are characterized by the Burgers vector which is determined by doing a loop around the dislocation line and noticing the extra interatomic spacing needed to close the loop. The line dislocation occur in two types, namely, edge dislocations and screw dislocations. Edge dislocations occur when extra planes are inserted in the lattice, the dislocation line is at the plane end and the Burgers vector is perpendicular to the dislocation line. Screw dislocations occur when lattice planes are displaced through shear and the Burgers vector is parallel to the dislocation line. Moving dislocations are also a mechanism for creep deformation [7, 8].

2.6 Planar Defects

Planar defects are two dimensional and they can be divided into three types:

Free surfaces, which are the external surfaces at terminal parts of the solid at a vapour or liquid. The interaction between the solid and the vapour or liquid phase is governed by the interface between the solid and the two phases and the characteristic behaviour and shape of the solid are affected;

Intercrystalline boundaries, separating grains or distinct phases within the solid. Almost all crystalline solids are polycrystalline. The interfaces that separate grains are called *grain boundaries* and those that separate phases are called *two-phase interfaces*;

Internal defects, that disrupt the crystalline pattern over a surface within a crystal. There are two common types of surface defects that appear in the interior of a crystal and they are *stacking faults* and *antiphase boundaries* [7].

2.7 Volume Defects

Volume defects in crystals are three-dimensional aggregates of atoms or vacancies and are commonly divided into four classes that based on a combination of the size and effect of the particle. According to [7], they include:

Precipitates are small particles that are introduced into the matrix by solid state reactions. They are a fraction of a micron in size.

Dispersants are larger particles that behave as a second phase and influence the behaviour of the primary phase. They may be large precipitates, polygranular particles, or grains distributed through the microstructure;

Inclusions are foreign particles or large precipitate particles and usually undesirable constituents in the microstructure within a crystal;

Voids are holes caused by gases that are trapped during solidification or by vacancy condensation in the solid state. Their principal effect is the decrease of the mechanical strength and the promotion of fracture at small loads.

2.8 Defect Activation and Formation Energy Estimations

Estimation of formation energies of defects can be determined experimentally and theoretically. In both cases, however, a theoretical approach is involved. One example of an experiment designed to determine the energy of formation of vacancies may use the positron annihilation property of vacancies [9, 10]. Computer simulations, which take into account experimentally determined physical properties of defects have also been used to theoretically predict (using statistical approaches) atomic scale processes in radiation damage [11, 12]. In this section, we review a brief background on theoretical estimations of the characteristic energies (i.e. energy of formation, energy of migration, activation energy) associated with point defects and point defect clusters.

2.8.1 Thermodynamics of point defect formation

For solid material, the thermodynamic variables of volume and pressure can be assumed to be constant in the absence of irradiation. With these assumptions, the Helmholtz free energy function applies, according to [13], as follows

$$F \cong G = U + pV - TS = H - TS, \tag{2.7}$$

where U is the internal energy, H is the total enthalpy of the N atoms comprising the system. S represents the disorder (entropy) in the system which is related to the statistical weight w as follows

$$S = k_\mathrm{B} \ln w. \tag{2.8}$$

The statistical weight w is the number of possible different permutations or configurations of atoms and k_B is Boltzmann's constant.

Let N be the number of defects and N_s the number of available sites. Then the increase in free energy is

$$\Delta G_\mathrm{f} = N\Delta H_\mathrm{f} - T\Delta S. \tag{2.9}$$

Here ΔH_f is the increase in enthalpy as a results of the formation of defects and ΔS is the change in total entropy of the system.

The entropy of the system can be expressed as a function of N as follows: If $N = 1$, and there are N_s available sites then there are N_s possible permutations of the defects, if we increase N to, say $N = 2$ then there are $N_\mathrm{s} - 1$ available sites and $N_\mathrm{s} - 1$ permutations. Therefore, for N defects there will be $N_\mathrm{s} - N + 1$ available sites and permutations. The total number of permutations is $N_\mathrm{s}(N_\mathrm{s} - 1)(N_\mathrm{s} - 2)\cdots(N_\mathrm{s} - N + 1)$, another way to write this is $N_\mathrm{s}!\,/(N_\mathrm{s} - N)!$. The N defects are indistinguishable, this means that the number $N_\mathrm{s}!\,/(N_\mathrm{s} - N)!$ includes repeated permutations. To only include different permutations w we divide the number above by $N!$:

$$w = \frac{N_\mathrm{s}(N_\mathrm{s} - 1)(N_\mathrm{s} - 2)\cdots(N_\mathrm{s} - N + 1)}{N!} = \frac{N_\mathrm{s}!}{N!\,(N_\mathrm{s} - N)!}. \tag{2.10}$$

The mixing entropy is then

$$\Delta S_\mathrm{mix} = k_\mathrm{B}\left[\ln N_\mathrm{s}! - \ln N! - \ln(N_\mathrm{s} - N)!\right]. \tag{2.11}$$

Using Stirling's approximation of $\ln x! \approx x \ln x$ for large x gives

$$\Delta S_{\text{mix}} = k_{\text{B}} \ln w \approx \ln[N_{\text{s}} \ln N_{\text{s}} - N \ln N - (N_{\text{s}} - N) \ln(N_{\text{s}} - N)]. \tag{2.12}$$

The vibrational disorder of defects also contributes to the change in the entropy ΔS, in addition to S_{mix}.

In the modelling of the vibrational disorder contribution, the atoms are represented as $3N_{\text{s}}$ independent linear harmonic oscillators, according to the Einstein model of lattice motion, with the associated entropy

$$S_{\text{f}} = 3k_{\text{B}} \ln\left(\frac{k_{\text{B}}T}{\hbar\omega_{\text{E}}}\right), \tag{2.13}$$

where ω_{E} is the natural angular frequency of the oscillator and $\hbar$ is the reduced Planck constant. If ℓ neighbours are changed by each defect to a vibration angular frequency ω_{r}, the entropy is

$$S_{\text{f}}' = 3k_{\text{B}}\ell \ln\left(\frac{k_{\text{B}}T}{\hbar\omega_{\text{r}}}\right) = 3k_{\text{B}}\ell\left[\ln\left(\frac{k_{\text{B}}T}{\hbar\omega_{\text{E}}}\right) - \ln\left(\frac{\omega_{\text{E}}}{\omega_{\text{r}}}\right)\right]. \tag{2.14}$$

For N defects, the total change in entropy due to vibrational disorder is

$$N(S_{\text{f}} - \ell S_{\text{f}}) = \Delta S_{\text{f}} = 3Nk_{\text{B}}\ell \ln\left(\frac{\omega_{\text{E}}}{\omega_{\text{r}}}\right). \tag{2.15}$$

Taking both contributions to the entropy change and inserting them into the free energy equation gives:

$$\Delta G_{\text{f}} = N\Delta H_{\text{f}} - k_{\text{B}}T\left[N_{\text{s}} \ln N_{\text{s}} - N \ln N - (N_{\text{s}} - N)\ln(N - N_{\text{s}}) + N \ln\left(\frac{\omega_{\text{E}}}{\omega_{\text{r}}}\right)^{3\ell}\right]. \tag{2.16}$$

In equilibrium, the free energy does not change with N, i.e. $\mathrm{d}\Delta G/\mathrm{d}N = 0$ which gives,

$$\frac{\Delta H_{\text{f}}}{k_{\text{B}}T} = \ln\left[\frac{N_{\text{s}} - N}{N}\left(\frac{\omega_{\text{E}}}{\omega_{\text{r}}}\right)^{3\ell}\right]. \tag{2.17}$$

Assuming that there are far more available sites than defects, i.e. $N \ll N_{\text{s}}$ and denoting the concentration, C, of N defects in N_{s} sites as $N/N_{\text{s}} = C$ (so that $(N_{\text{s}} - N)/N \approx N_{\text{s}}/N = 1/C$ in (2.17)) then,

$$C = \left(\frac{\omega_{\text{E}}}{\omega_{\text{r}}}\right)^{3\ell} \exp\left(-\frac{\Delta H_{\text{f}}}{k_{\text{B}}T}\right). \tag{2.18}$$

If $(\omega_{\text{E}}/\omega_{\text{r}})^{3\ell}$ is expressed in terms of the entropy we get

$$C = \frac{N}{N_{\text{s}}} = \exp\left(\frac{\Delta S_{\text{f}}}{k_{\text{B}}}\right)\exp\left(-\frac{\Delta H_{\text{f}}}{k_{\text{B}}T}\right) = \exp\left(-\frac{\Delta G_{\text{f}}}{k_{\text{B}}T}\right). \tag{2.19}$$

The energy of formation for the defects E_{f} is equal to the change in enthalpy, so for the k-type defect

$$E_{\text{f}}^{k} = \Delta H_{\text{f}}^{k}. \tag{2.20}$$

Typical values of the energy of formation for interstitials and vacancies in metals are $E_{\text{f}}^{\text{i}} = 4\,\text{eV}$ and $E_{\text{f}}^{\text{v}} = 1\,\text{eV}$, respectively.

2.8.2 Cavity estimation of the vacancy energy of formation

One theoretical approach for determining an estimate for the energy of formation of defects, besides performing an experiment, is by considering the crystal energy increase by an introduction of a cavity into a rigid crystal. Let us denote the volume of the cavity by Ω, then

$$\Omega = \frac{4}{3}\pi r_{\mathrm{a}}^3, \tag{2.21}$$

and Ω is equal to the volume occupied by one atom with a radius of r_{a}. Suppose the crystal is a sphere of radius R. To conserve the volume of the sphere, the volume from the cavity is spread uniformly over the surface of the crystal. Then the new radius R' is

$$R' = R + \Delta R. \tag{2.22}$$

The condition that the volume is conserved leads to the relation

$$4\pi R^2 \Delta R = \frac{4}{3}\pi r_{\mathrm{a}}^3 \tag{2.23}$$

and if the crystal is large compared to the size of the atom, then $R \gg r_{\mathrm{a}}$ and $\Delta R \ll R$ and

$$\Delta R = \frac{r_{\mathrm{a}}^3}{3R^2}. \tag{2.24}$$

Let $E_{\mathrm{f}}^{\mathrm{v}}$ be the difference in surface energy of the crystal with and without a cavity and σ be the surface energy per unit area, then

$$E_{\mathrm{f}}^{\mathrm{v}} = 4\pi r_{\mathrm{a}}^2\sigma + 4\pi\sigma\,(R + \Delta R)^2 - 4\pi R^2\sigma \sim 4\pi\sigma\left(r_{\mathrm{a}}^2 + 2R\Delta R\right). \tag{2.25}$$

Here the first two terms on the right-hand side of the equation are the energies associated with the inner and outer surface after formation of the vacancy and the last term is the energy of the surface of the crystal before the vacancy formation, the ΔR^2 term has been neglected. Substituting (2.24) for ΔR yields

$$E_{\mathrm{f}}^{\mathrm{v}} = 4\pi\sigma\left(r_{\mathrm{a}}^2 + \frac{2}{3}\frac{r_{\mathrm{a}}^3}{R}\right) = 4\pi\sigma r_{\mathrm{a}}^2\left(1 + \frac{2}{3}\frac{r_{\mathrm{a}}}{R}\right), \tag{2.26}$$

and since $r_{\mathrm{a}} \ll R$, we have:

$$E_{\mathrm{f}}^{\mathrm{v}} \sim 4\pi\sigma r_{\mathrm{a}}^2. \tag{2.27}$$

In most metals, $\sigma \sim 10\,\mathrm{eV/nm^2}$, and $r_{\mathrm{a}} \sim 0.15\,\mathrm{nm}$, so $E_{\mathrm{f}}^{\mathrm{v}} \sim 2\,\mathrm{eV}$ [4]. If the crystal is treated as an elastic continuum, then a more definitive expression for $E_{\mathrm{f}}^{\mathrm{v}}$ is

$$E_{\mathrm{f}}^{\mathrm{v}} = 4\pi r_{\mathrm{a}}^2\sigma - 12\pi r_{\mathrm{a}}\frac{\sigma^2}{\mu} + 16\pi r_{\mathrm{a}}\frac{\sigma^2}{\mu}. \tag{2.28}$$

Here the first term on the right-hand side of (2.28) is the surface energy of the cavity while the second term represents the reduction in surface energy due to contraction of the surface by the surface tension, the third term is the elastic energy stored in the solid and μ is the shear modulus of the crystal. The vacancy formation energy, $E_{\mathrm{f}}^{\mathrm{v}} \sim 1\,\mathrm{eV}$ [4].

2.8.3 Defect clusters

In this section we aim to derive expressions for the activation energy of interstitial and vacancies in clusters and their binding energy to the clusters.

The formation and accumulation of interstitial and vacancy clusters depends on the kinetic coefficients. In some interesting cases defects have been observed to self-organise into Stacking-Fault Tetrahedra in fcc metals [14]. The clusters can be created directly in displacement or collision cascades, which can be introduced when the host material is irradiated in a localised region [15]. The kinetic coefficients are functions of the cluster size [3]. An example of this fact is the proportionality of the probability of emission of an interstitial atom by a cluster to the number of atoms which occupy the dislocation loop edge. Kinetic coefficients are difficult to obtain and the difficulty is caused by their dependence on material properties, the physical processes occurring in the material and the irradiation conditions.

Consider a *k-cluster* which is defined as a cluster containing k interstials (or k interstitial atoms), the binding energy E_k^{b} of the cluster is the difference in energy between the crystal containing the k-cluster and the crystal containing k interstitials with a low density such than their interaction energy is negligible. The binding energy of the interstitials of a k-cluster, E_k^{b1}, is the difference in energy between a crystal containing the k-cluster, E_{f}^{k} and the crystal with a $(k-1)$-cluster, and an interstitial that is far from the cluster $E_{\mathrm{f}}^{\mathrm{i}}$, that is

$$E_{\mathrm{f}}^{\mathrm{b1}} = \left(E_{\mathrm{f}}^{k} - E_{\mathrm{f}}^{k-1}\right) - E_{\mathrm{f}}^{\mathrm{i}}. \tag{2.29}$$

Here E_{f}^{k} represents the energy of formation of a k-cluster, which is the energy difference between a crystal with and without a k-cluster. The energies considered satisfy the following relations:

$$\begin{aligned} E_{\mathrm{f}}^{k} &= E_{\mathrm{f}}^{k-1} + E_{\mathrm{f}}^{\mathrm{i}} + E_{\mathrm{f}}^{\mathrm{b1}}, \\ E_{\mathrm{f}}^{k} &= kE_{\mathrm{f}}^{\mathrm{i}} + E_{\mathrm{f}}^{\mathrm{b1}}, \\ E_{k}^{\mathrm{b}} &= \sum_{k'=2}^{k} E_{k'}^{\mathrm{b1}}. \end{aligned} \tag{2.30}$$

The instability of the k-cluster with respect to the decomposition into interstitials or with respect to emission of interstitials is represented by negative values of the binding energies, $E_{\mathrm{f}}^{\mathrm{b1}}$ and $E_{\mathrm{k}}^{\mathrm{b}}$, respectively. At the thermal equilibrium state the probability of the growth of the k-cluster (i.e. growth from k to $k+1$) is equal to the probability of the thermal-stimulated decay of the $(k+1)$-cluster. The growth rate coefficient of the k-cluster is

$$\alpha_k = \frac{n_{k+1}^{\mathrm{e}}}{n_k^{\mathrm{e}} n_{\mathrm{i}}^{\mathrm{e}}} \frac{1}{\tau_{k+1}}, \tag{2.31}$$

where n_{k+1}^{e}, n_k^{e} and $n_{\mathrm{i}}^{\mathrm{e}}$ are the equilibrium defect densities (number of defects per unit volume) of the k-cluster, $(k+1)$-cluster and of the interstitials, respectively. Substitution of the equilibrium densities in (2.31) leads to the relation connecting the growth rate coefficient of the k-cluster with the k-cluster with the lifetime of the $(k+1)$-cluster:

$$\alpha_k = \frac{1}{\tau_{k+1}} \frac{1}{N\,(k+1)} \exp\left(-\frac{E_{\mathrm{f}}^{k+1} - E_{\mathrm{f}}^{k} - E_{\mathrm{f}}^{\mathrm{i}}}{k_{\mathrm{B}}T}\right) = \frac{1}{\tau_{k+1}} \frac{1}{N\,(k+1)} \exp\left(-\frac{E_{k+1}^{\mathrm{b1}}}{k_{\mathrm{B}}T}\right). \tag{2.32}$$

The cluster decay occurs as a result of the emission of one atom from the edge of the dislocation loop and its displacement to a distance that is approximately equal to the radius of the dislocation core. To escape the cluster, the atom has to overcome a potential barrier equal to its binding energy with the cluster. The lifetime of the cluster increases as its binding energy increases and the lifetime of the k-cluster can be represented in the following way,

$$\tau_k = A(k)\exp\left(\frac{E_{\mathrm{k}}^{\mathrm{b1}}}{k_{\mathrm{B}}T}\right), \tag{2.33}$$

where $A(k)$ is the pre-exponential factor and is equal to the lifetime of the cluster with zero binding energy. It is proportional to the displacement time of an atom from the dislocation loop at a distance of the order of the radius, r_0, of the dislocation core, k_L, by means of diffusion; it is also inversely proportional to the fraction of edge atoms,

$$A(k) = \frac{k}{k_L}\frac{r_0^2}{D_{\mathrm{i}}}, \tag{2.34}$$

where $D_{\mathrm{i}} = D_{\mathrm{i}}^0\exp(-E_{\mathrm{m}}^{\mathrm{i}}/k_{\mathrm{B}}T)$ is the diffusion coefficient for interstitials and $E_{\mathrm{m}}^{\mathrm{i}}$ is the interstitial migration energy; and

$$k_L = \frac{2}{a}\sqrt{\frac{k\pi\Omega}{b}}, \tag{2.35}$$

where a is the interatomic distance, Ω is the atomic volume and b is the Burgers vector. The expression for the lifetime of the cluster, thus, takes the form:

$$\tau_k = \frac{ar_0^2}{2D_{\mathrm{i}}}\sqrt{\frac{bk}{\pi\Omega}}\exp\left(\frac{E_{\mathrm{k}}^{\mathrm{b1}}}{k_{\mathrm{B}}T}\right) = \frac{ar_0^2}{2D_{\mathrm{i}}}\sqrt{\frac{bk}{\pi\Omega}}\exp\left(\frac{E_{\mathrm{f}}^{k} - E_{\mathrm{f}}^{k-1} - E_{\mathrm{f}}^{\mathrm{i}}}{k_{\mathrm{B}}T}\right). \tag{2.36}$$

The binding energy E_k^{b1} depends on the energy difference between the energy of formation of the k-cluster and the $(k-1)$-cluster. This energy difference can be written as a function of the changing of energy of the links between atoms of the cluster and changing of the linear tension energy of links between cluster atoms and changing of linear tension E_L energy at the edge of the dislocation loop given by

$$E_L = 2\pi R\mu b^2, \tag{2.37}$$

where μ is the shear modulus. The loop radius, R, is a function of the number of its atoms k

$$R = \sqrt{\frac{k\Omega}{\pi b}}. \tag{2.38}$$

The binding energy of the interstitial and the k-cluster becomes

$$E_k^{\mathrm{b1}} = \mu b\sigma\left(\sqrt{k} - \sqrt{k-1} - E_{\mathrm{i1}} - E_{\mathrm{f}}^{\mathrm{i}}\right), \tag{2.39}$$

where E_{i1} is the energy of the broken links and as a result of the separation of an atom and $\sigma = \sqrt{4\pi\Omega b}$ is introduced to simplify notations. Both E_{i1} and E_{i1} are independent of the cluster size and we can compact them into a temperature dependent variable B as follows:

$$B = B(T) = \exp\left(-\frac{E_{\mathrm{i1}} + E_{\mathrm{f}}^{\mathrm{i}}}{k_{\mathrm{B}}T}\right). \tag{2.40}$$

The cluster life time (2.36) can be re-written as follows:

$$\tau_k = \frac{ar_0^2}{D_{\mathrm{i}}\sigma}\sqrt{k}B(T)\exp\left[\frac{\mu b\sigma\left(\sqrt{k} - \sqrt{k-1}\right)}{k_{\mathrm{B}}T}\right]. \tag{2.41}$$

Substituting (2.41) into (2.32), we get

$$\alpha_k = \frac{D_\mathrm{i}\sigma\sqrt{k}}{N(k+1)abr_0^2}B^{-2}(T)\exp\left(-\eta_k\right), \tag{2.42}$$

where the parameter η_k is

$$\eta_k = \frac{2\mu b\sigma\left(\sqrt{k+1}-\sqrt{k}\right)}{k_\mathrm{B}T}. \tag{2.43}$$

The cluster growth, α_k can be expressed in terms of the diffusion α_k^d and the reaction α_k^r as follows:

$$\frac{1}{\alpha_k} = \frac{1}{\alpha_k^\mathrm{d}} + \frac{1}{\alpha_k^\mathrm{r}}, \qquad \alpha_k = \frac{\alpha_k^\mathrm{d}\alpha_k^\mathrm{r}}{\alpha_k^\mathrm{d}+\alpha_k^\mathrm{r}}. \tag{2.44}$$

The application of Smoluchowski's relation yields

$$\alpha_k^\mathrm{d} = 4\pi R(k)(D_\mathrm{i}+D_k). \tag{2.45}$$

Here D_k is the diffusion coefficient of the k-cluster, which can be set equal to zero for interstitial loops. The Arrhenius relation can be used to determine α_k^r:

$$\alpha_k^\mathrm{r} = \frac{S(k)(D_\mathrm{i}+D_k)}{a}\exp\left(-\frac{E_\mathrm{a}^\mathrm{i}}{k_\mathrm{B}T}\right), \tag{2.46}$$

where $S(k) = 2\pi R(k)b$ is the active surface that absorbs defects and E_a^i is the activation energy of the interstitials that attach to the cluster. Upon substitution, the coefficient of the rate of cluster growth takes the form,

$$\alpha_k = \frac{(D_\mathrm{i}+D_k)\sigma\sqrt{k}}{(D_\mathrm{i}+D_k)\sigma\sqrt{k}+\exp\left(E_\mathrm{a}^\mathrm{i}/k_\mathrm{B}T\right)}. \tag{2.47}$$

The activation energy of the joining of interstitials to the cluster as a function of k (obtained by equating (2.47) and (2.42)) is

$$E_\mathrm{a}^\mathrm{i} = k_\mathrm{B}T\ln\left[(D_\mathrm{i}+D_k)\sigma\sqrt{k}\left(\frac{Nr_0^2B^2b}{D_\mathrm{i}\sigma}\frac{(k+1)^{3/2}}{k}\exp\left(\eta_k\right)-1\right)\right]. \tag{2.48}$$

At large k the activation energy grows like $\ln(k)$ and the activation energy increases with increasing k. The recombination energy is equal to the vacancy activation energy E_a^v and it depends on k in a manner that coincides with the dependence of E_a^i on k up to the ration of dilatational volumes, but has the opposite sign,

$$E_\mathrm{a}^\mathrm{v} = -k_\mathrm{B}T\frac{\Delta V_\mathrm{v}}{\Delta V_\mathrm{i}}\ln\left[(D_\mathrm{i}+D_k)\sigma\sqrt{k}\left(\frac{Nr_0^2B^2b}{D_\mathrm{i}\sigma}\frac{(k+1)^{3/2}}{k}\exp\left(\eta_k\right)-1\right)\right], \tag{2.49}$$

where ΔV_v and ΔV_i are the dilatational volumes of a vacancy and interstitial, respectively.

2.9 Isothermal Annealing

Isothermal annealing of defects occurs when there is no change in temperature of the system. In a physical experiment, where defects release thermal energy when they anneal, isothermal annealing conditions can be achieved by removing the thermal energy, produced by the annealing defects, from the system. In this section we review the theory of the modelling of annealing of defects that does not take account of the thermal energy released by the annealing defects.

2.9.1 Diffusion

Besides thermally initiated annealing, defect diffusion is another mechanism through which defects in a material can anneal and the material properties can be restored. The defects can annihilate when they interact with other defect specie. For example, interstitials and vacancies can annihilate when they cross paths or recombine. The interstitials and vacancies can also annihilate with sinks. In some interesting cases sinks like grain boundaries can be a source of interstitials which annihilate with available vacancies in the material [16].

At a macroscopic level, the time change of the defects can be formulated in two ways, either by (1) only considering the flux of defects from a radius that is larger than the defect separation or (2) by only considering the time evolution of the defect concentration (which depends on temperature). In both these views, the underlying mechanism of diffusion is, in principle, microscopic. At a macroscopic level, *balance equations* (explained in detail later in this section) which take into account microscopic factors are used to formulate the change in defect density.

Macroscopic description of defect diffusion

There are two laws that govern diffusion, which were derived by Fick in 1880 and which apply to any state of matter because of their general character regarding macroscopic diffusion processes. The first law is a relationship between the flux, $\boldsymbol{J}$, and the concentration or density gradient of the diffusing specie:

$$\boldsymbol{J} = -D\nabla C, \tag{2.50}$$

where D is the diffusion coefficient. The second law relates the density gradient and the rate of change of the density caused by diffusion, at a given point, as follows,

$$\frac{\partial C}{\partial t} = \nabla \cdot \boldsymbol{J} = -\nabla \cdot (D\nabla C)\,. \tag{2.51}$$

If D does not change in space and is not a function of the defect density, we write

$$\frac{\partial C}{\partial t} = -D\nabla^2 C. \tag{2.52}$$

In one dimension (2.52) reduces to

$$\frac{\partial C}{\partial t} = -D\frac{\partial^2 C}{\partial x^2}. \tag{2.53}$$

Mechanisms of point defect diffusion

Here we explore several mechanism of diffusion that can be distinguished, according to [17, 4]. They are the following:

Exchange mechanisms: The exchange mechanism, Figure 2.3 (left), does not require the presence of defects and is highly improbable in close packed crystals because it requires considerable deformation and an enormous activation energy. It involves the exchange of lattice positions of two atoms located in adjacent crystal sites.

The ring mechanism: The ring mechanism, Figure 2.3 (right), requires coordinated movement of three to five atoms. The probability of this mechanism is low and the energy is still high, although it requires less energy to start compared to the exchange mechanism.

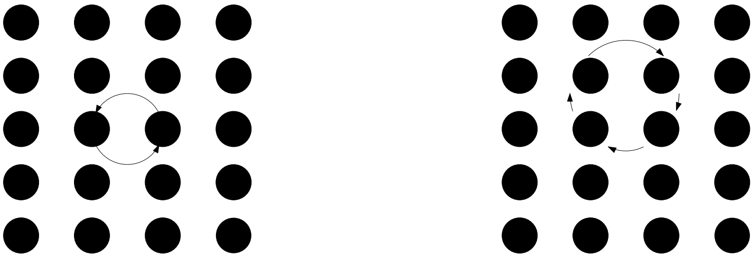

Figure 2.3: Exchange (on the left) and ring (on the right) mechanisms of diffusion.

Vacancy mechanism: The vacancy mechanism, Figure 2.4 (left), is the simplest of diffusion mechanism and occurs in metals and alloys. The diffusion occurs by the jump of an atom from its lattice site to a vacant site, hence it is triggered by the presence of a neighboring vacancy. The vacancy is displaced in the opposite direction of the lattice atom but the coefficient for vacancy diffusion is not equal to that of the lattice atom diffusion.

Interstitial mechanism: This mechanism involves the displacement of an atom from one interstitial site to another, which requires considerable energy to push trough the barrier atoms separating the interstitial sites of the crystal, Figure 2.4 (right). This mechanism occurs when the diffusing specie is of an atom size that is smaller than the host lattice atoms.

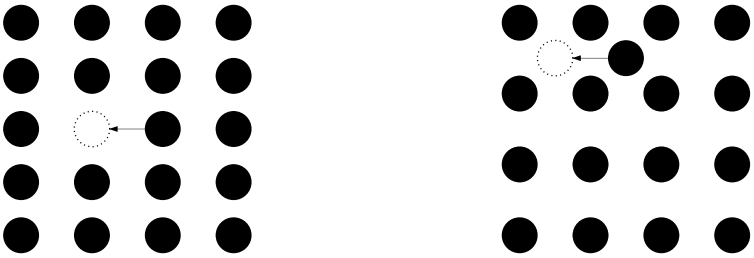

Figure 2.4: Vacancy (on the left) and interstitial (on the right) mechanisms of diffusion.

Interstitialcy mechanism: The interstitialcy mechanism involves the displacement of adjacent lattice atoms to an interstitial site (usually of comparable diameter). There are two variants of the mechanism, namely, collinear variant where atoms move along a straight line Figure 2.5 (left), and non-collinear variant where the displaced atom moves to the interstitial site at an angle Figure 2.5 (right).

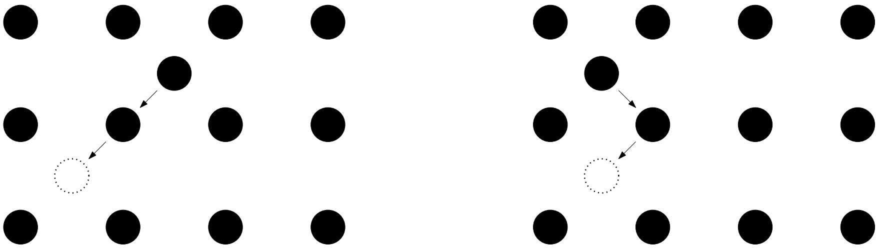

Figure 2.5: Collinear variant interstitialcy mechanism of diffusion (left). Non-collinear variant interstitialcy mechanism of diffusion (right).

Crowding (crowdion) mechanism: The crowding mechanism (Figure 2.6) occurs when an atom is added to a lattice plane but does not reside in the interstitial site. The lattice atoms over the plane are then shifted (perhaps 10 lattice atoms) with respect to their lattice sites. This configuration can be a dumbbell spread over 10 atoms along a row.

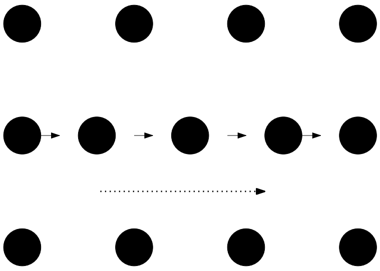

Figure 2.6: Crowdion mechanism of diffusion.

2.9.2 The balance equations for point defects

Collisions between high-energy particles and lattice atoms creates Frenkel defects which are lost through recombination of vacancies and interstitials or by reaction with a defect sink (a defect sink can be a void, grain boundary, dislocation, dislocation loop). The *balance equations of point defects* are used to describe the defect concentration at any point in time as a balance between the production rate and the loss rate of point defects. The local change in the concentration of the different types of defects can be written as the net result of the local defect production rate, the reaction of the different types of defects with each other and with the diffusion in or out of a local volume. In the presence of localised sinks, spatial uniformity is lost and the local distribution of the concentration of defects, C has a spatial dependence, i.e. $C = C(r)$ where r is a localised radius. The *chemical rate equations* are used as follows, to describe the competing processes,

$$\begin{aligned} \frac{\partial C_\mathrm{v}}{\partial t} &= K_0 - K_\mathrm{iv} C_\mathrm{i} C_\mathrm{v} - K_\mathrm{vs} C_\mathrm{v} C_\mathrm{s} + \nabla \cdot D_\mathrm{v} \nabla C_\mathrm{v}, \\ \frac{\partial C_\mathrm{i}}{\partial t} &= K_0 - K_\mathrm{iv} C_\mathrm{i} C_\mathrm{v} - K_\mathrm{is} C_\mathrm{i} C_\mathrm{s} + \nabla \cdot D_\mathrm{i} \nabla C_\mathrm{i}. \end{aligned} \tag{2.54}$$

Here C_v and C_i are the vacancy and interstitial concentrations, respectively and K_0 is the defect production rate; K_iv, K_is and K_vs represent the vacancy-interstitial recombination rate coefficient, the interstitial-sink reaction rate coefficient and vacancy-sink reaction rate coefficient, respectively. The concentration of sinks is denoted by C_s. The last terms on the right,$\nabla \cdot D_\mathrm{v} \nabla C_\mathrm{v}$ and $\nabla \cdot D_\mathrm{i} \nabla C_\mathrm{i}$ represent the diffusion of defects from a local volume, and D_v and D_i are the diffusion coefficient for the vacancies and interstitials respectively.

If we assume that the mean separation of the defects is greater than the mean distance between sinks then the spatial dependence of the defect concentrations can be neglected and $\nabla C \approx 0$. In this case the sink density becomes higher than the defects density and the sink density can be treated as being uniformly distributed, and (2.54) can be re-written as follows

$$\begin{aligned} \frac{\mathrm{d}C_\mathrm{v}}{\mathrm{d}t} &= K_0 - K_\mathrm{iv} C_\mathrm{i} C_\mathrm{v} - K_\mathrm{vs} C_\mathrm{v} C_\mathrm{s}, \\ \frac{\mathrm{d}C_\mathrm{i}}{\mathrm{d}t} &= K_0 - K_\mathrm{iv} C_\mathrm{i} C_\mathrm{v} - K_\mathrm{is} C_\mathrm{i} C_\mathrm{s}. \end{aligned} \tag{2.55}$$

Equation (2.55) can be used to explore various limiting cases for the concentrations of defects. For example, one might be interested in the steady-state solutions, or the solutions in the case where one type of defects dominates.

Defect Density during and after Irradiation

In the absence of sinks and thermal vacancies (2.55) becomes

$$\begin{aligned} \frac{\mathrm{d}C_\mathrm{v}}{\mathrm{d}t} &= K_0 - K_\mathrm{iv}C_\mathrm{i}C_\mathrm{v}, \\ \frac{\mathrm{d}C_\mathrm{i}}{\mathrm{d}t} &= K_0 - K_\mathrm{iv}C_\mathrm{i}C_\mathrm{v}. \end{aligned} \tag{2.56}$$

The diffusion coefficient under radiation D_rad in a pure metal is given by

$$D_\mathrm{rad} = D_\mathrm{i}C_\mathrm{i} + D_\mathrm{v}C_\mathrm{v}, \tag{2.57}$$

where $C_\mathrm{i} = C_\mathrm{v}$, but $D_\mathrm{i} \gg D_\mathrm{v}$ and so interstitials contribute much more to atom mobility than do vacancies. Initially the defect densities build up linearly according to $\mathrm{d}C/\mathrm{d}t = K_0$ with $C_\mathrm{i} \sim C_\mathrm{v}$. The production term, K_0, is the *effective* point defect production rate, it refers to the production of only freely migrating defects that can give rise to long-range diffusion [4]. For the case $C_\mathrm{v} = C_\mathrm{i} = C$, hence

$$\frac{\mathrm{d}C}{\mathrm{d}t} = K_0 - K_\mathrm{iv}C^2. \tag{2.58}$$

If the initial sink density is zero then the exact solution to (2.58) is

$$C(t) = \sqrt{\frac{K_0}{K_\mathrm{iv}}}\tanh(\sqrt{K_\mathrm{iv}K_0}t). \tag{2.59}$$

Analysis of the plot of (2.59), shown in Figure 2.7, shows that after some time $t = t_1$, the production rate of defects is approximately zero, i.e.

$$\frac{\mathrm{d}C}{\mathrm{d}t} = K_0 - K_\mathrm{iv}C^2 \approx 0. \tag{2.60}$$

Therefore t_1 is the characteristic time for the onset of mutual recombination. For $t \geq t_1$ the solution is

$$C \approx \sqrt{\frac{K_0}{K_\mathrm{iv}}}. \tag{2.61}$$

At time $t \leq t_1$ the defect density can be approximated as a linear build up as

$$C \approx K_0 t. \tag{2.62}$$

Equating (2.61) and (2.62) gives

$$K_0 t = \sqrt{\frac{K_0}{K_\mathrm{iv}}}. \tag{2.63}$$

Therefore,

$$t = t_1 = (K_0 K_\mathrm{iv})^{-1/2}. \tag{2.64}$$

If, after irradiation at time $t = t_1$ and $K_0 = 0$, the thermal equilibrium defect concentration is $C_0' = C(t_1)$ then the concentration of defects after irradiation changes as follows,

$$\frac{\mathrm{d}C'}{\mathrm{d}t} = -K_\mathrm{iv}C'^2. \tag{2.65}$$

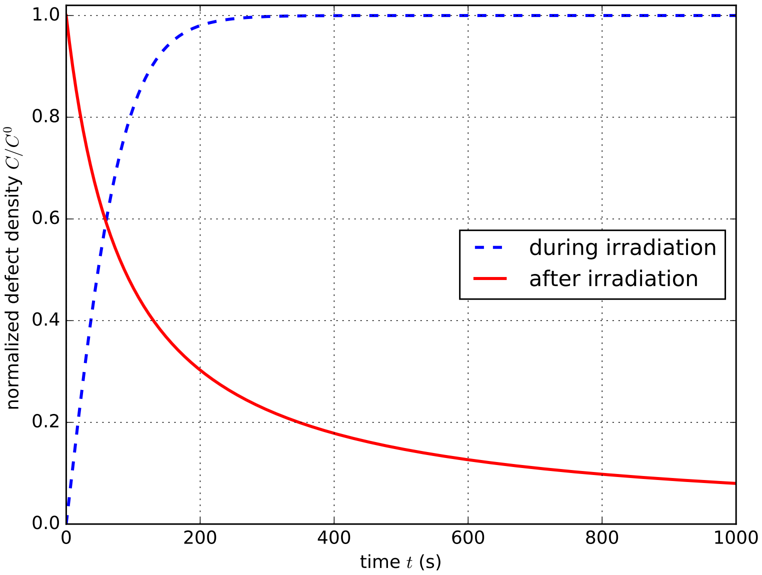

Figure 2.7: Schematic of time evolution of the normalized density of defects in an irradiated material, before and after irradiation at a low temperature.

The solution to (2.65) is

$$C'(t) = \frac{1}{K_{iv}t + \gamma}, \tag{2.66}$$

where γ is the constant of integration such that

$$C'(t = 0) = \frac{1}{\gamma} = \sqrt{\frac{K_0}{K_{iv}}} \tanh(\sqrt{K_{iv}K_0}t_1). \tag{2.67}$$

The vacancy-interstitial recombination constant, K_{iv}, is proportional to the interaction radius of the reaction between interstitials and vacancies, r_{iv},

$$K_{iv} = 4\pi r_{iv}(D_i + D_v) \approx 4\pi r_{iv} D_i. \tag{2.68}$$

In Figure 2.8 we present the schematic of the normalized concentrations for the solution (2.66) for different interaction radii.

The Steady State Solution in the Presence of Sinks

If there is only one type of sink, then at steady state

$$\begin{aligned} K_0 &= K_{iv}C_iC_v + K_{vs}C_vC_s, \\ K_0 &= K_{iv}C_iC_v + K_{is}C_iC_s, \end{aligned} \tag{2.69}$$

or

$$K_{vs}C_v = K_{is}C_i, \tag{2.70}$$

and the absorption rate of interstitials and vacancies at sinks is equal, or the net absorption rate at the sink is zero. Even for the case of multiple sink types, if the sinks have the same "strength" for vacancies and interstitials, then the net flow to any sink is zero.

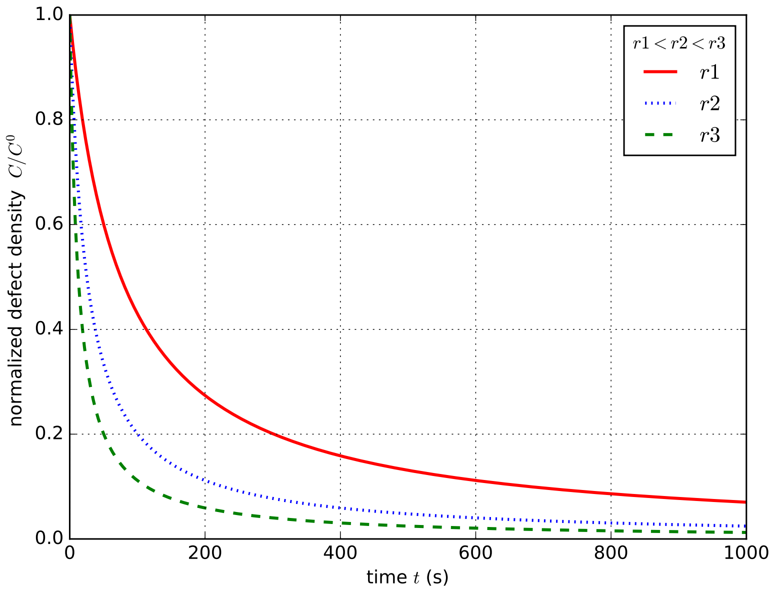

Figure 2.8: Schematic of the time evolution of normalized defect concentration for different interaction radii, $r_{\mathrm{iv},j}$, where $j = 1, 2, 3$. As expected, when the interaction radius is increased the probability for annihilation of interstitials and vacancies increases and the defect concentration decreases faster.

Inclusion of sink terms violates the symmetry with respect to C_i and C_v because the reaction-rate coefficients for the vacancy-sink and interstitial-sink are different (i.e. $K_\mathrm{vs} \neq K_\mathrm{is}$). Symmetry is present in the steady state with regard to $D_\mathrm{i}C_\mathrm{i}$ and $D_\mathrm{v}C_\mathrm{v}$ (since $K_\mathrm{is} \propto D_\mathrm{i}$ and $K_\mathrm{vs} \propto D_\mathrm{v}$). The physical consequence is that vacancies and interstitials contribute to atom mobility to the same extent and their actions cannot be differentiated. At steady state

$$\begin{aligned} 0 &= K_0 - K_\mathrm{iv}C_\mathrm{i}C_\mathrm{v} - K'_\mathrm{vs}D_\mathrm{v}D_\mathrm{v}C_\mathrm{s}, \\ 0 &= K_0 - K_\mathrm{iv}C_\mathrm{i}C_\mathrm{v} + K'_\mathrm{is}D_\mathrm{i}D_\mathrm{i}C_\mathrm{s}, \end{aligned} \tag{2.71}$$

where the K terms have been written as $K = K'D$ giving:

$$D_\mathrm{v}C_\mathrm{v}K'_\mathrm{vs}C_\mathrm{s} = D_\mathrm{is}C_\mathrm{i}K'_\mathrm{is}C_\mathrm{s}. \tag{2.72}$$

If $K'_\mathrm{vs} \sim K'_\mathrm{is}$, then $D_\mathrm{i}C_\mathrm{i} = D_\mathrm{v}C_\mathrm{v}$ which means that vacancies and interstitials contribute equally to atom mobility. The faster rate of diffusion of interstitials (compared to vacancies) compensates the much lower steady state concentration of the interstitials (compared vacancies) such that the vacancies and interstitials contribute *equally* to atom mobility. In real metals, K_vs and K_is are not equal because specific sinks have a bias for certain point defects.

2.9.3 Defect density: number of defects per unit volume

With the exclusion of Section 2.8.3, we have thus far referred to the defect density as the number of defects per available defect site ($C = N/N_\mathrm{s}$). We will now proceed by denoting the density of defects, with the symbol n, defined as the number of defects, denoted by N, per unit volume.

Consider a sample at a temperature T without any change in temperature, the evolution in time of defects of k-type can be formulated as follows [3]:

$$\frac{\mathrm{d}n_k}{\mathrm{d}t} = -\frac{n_k}{\tau_k}. \tag{2.73}$$

If the initial defects density is $n_{k,0}$, then the defect density decreases monotonically according to the exponential law:

$$n_k(t) = n_{k,0} \exp\left(-\frac{t}{\tau_k}\right). \tag{2.74}$$

Here, τ_k, is a temperature dependent characteristic time and it is given by the Arrhenius law

$$\tau_k^{-1} = \tau_{0,k}^{-1} \exp\left(-\frac{E_{\mathrm{a},k}}{k_\mathrm{B} T}\right), \tag{2.75}$$

where $\tau_{0,k}$ is a material property dependent parameter.

2.10 Adiabatic Annealing

When the initial temperature of the sample is set above absolute temperature the defects anneal and the annealing rate depends on temperature according to the Arrhenius law (2.75). The defects release their stored energy (that is equal to their formation energy) thermally. The entire process, from the increase in the annealing rate when the sample temperature is increased to the release of thermal energy from the annealing defets, is referred to as the *thermal concentration feedback*. If the system is isolated from the environment and the defect density and the temperature is uniform at the initial moment of time then the time change of the temperature as a result of the thermal energy released is as given by the following equation [3]:

$$c\frac{\mathrm{d}T}{\mathrm{d}t} = \theta_k \frac{n_k}{\tau_k}, \tag{2.76}$$

where c is the volumetric heat capacity of the material and θ_k is the thermal energy released as a result of the annealing of a single defect of type k.

2.10.1 Homogeneous annealing

In this section we consider the case where homogeneous annealing can be achieved and the distribution of the temperature and of the defect density remain uniform in the sample. We will derive an analytic formula for the dependence of the defect density and temperature on time.

We denote by Θ_k the *thermal contribution* from the annealing defects, defined as the sample temperature increase at any time as a result of the energy density of amount $\theta_k n_k$ that is released into the sample of volumetric heat capacity c in the process annealing and thereby raising the temperature of the sample by an amount $\theta n_k/c$:

$$\Theta_k = \frac{\theta_k}{c} n_k. \tag{2.77}$$

If we substitute (2.73) into (2.76) and rearrange terms, we get

$$\frac{\mathrm{d}}{\mathrm{d}t}\left(T + \Theta_k\right) = 0, \tag{2.78}$$

which leads to the energy conservation relationship

$$T(t) + \Theta_k(t) = \text{const.} \tag{2.79}$$

The final temperature of the sample T_f, after all defects are annealed, is equal to the initial temperature of the sample and the thermal contribution from the annealed defects:

$$T_\mathrm{f} = T_0 + \Theta_{k,0}, \tag{2.80}$$

where $\Theta_{k,0} = \theta n_{0,k}/c$ and $n_{k,0}$, as before, is the initial density of defects. By taking energy conservation into account we can equate (2.79) to the final temperature of the sample

$$T + \Theta_k = T_\mathrm{f} \quad \text{or} \quad \Theta_k = T_\mathrm{f} - T. \tag{2.81}$$

If we substitute n_k by Θ_k and T by $T_\mathrm{f} - \Theta_k$ into (2.73), we get

$$\frac{\mathrm{d}t}{\tau_{0,k}} = -\frac{1}{\Theta_k}\exp\left(\frac{T_\mathrm{a}}{T_\mathrm{f} - \Theta_k}\right)\mathrm{d}\Theta_k, \tag{2.82}$$

where we express the activation energy in temperature units in order to simplify notations, i.e.

$$T_\mathrm{a} = \frac{E_\mathrm{a}}{k_\mathrm{B}} \tag{2.83}$$

and we make the following substitution in (2.82):

$$\zeta = \frac{T_\mathrm{a}}{T_\mathrm{f} - \Theta^k}. \tag{2.84}$$

Then the differential in (2.82) transforms as follows:

$$\frac{\mathrm{d}\zeta}{\mathrm{d}\Theta_k} = \frac{T_\mathrm{a}}{\left(T_\mathrm{f} - \Theta^k\right)^2} = \frac{\zeta^2}{T_\mathrm{a}} \quad \text{and} \quad \mathrm{d}\Theta_k = \frac{T_\mathrm{a}}{\zeta^2}\mathrm{d}\zeta. \tag{2.85}$$

Finally,

$$-\frac{1}{\Theta_k}\exp\left(\frac{T_\mathrm{a}}{T_\mathrm{f} - \Theta_k}\right)\mathrm{d}\Theta_k = -\mathrm{e}^{\zeta}\frac{\chi\mathrm{d}\zeta}{\zeta\left(\zeta - \chi\right)} = \mathrm{e}^{\zeta}\frac{\mathrm{d}\zeta}{\zeta} - \mathrm{e}^{\zeta}\frac{\mathrm{d}\zeta}{\left(\zeta - \chi\right)}, \tag{2.86}$$

where $\chi = T_\mathrm{a}/T_\mathrm{f}$. The simplification of the right-hand side of (2.86) was done using a trick for decomposition of fractions [18]. We may simplify the second term on the right-hand side of (2.86) further by substituting $\varepsilon = \zeta - \chi$, so that

$$\mathrm{e}^{\zeta}\frac{\mathrm{d}\zeta}{\left(\zeta - \chi\right)} = \mathrm{e}^{(\varepsilon+\chi)}\frac{\mathrm{d}\varepsilon}{\varepsilon} = \mathrm{e}^{\chi}\mathrm{e}^{\varepsilon}\frac{\mathrm{d}\varepsilon}{\varepsilon}. \tag{2.87}$$

The integral of the right-hand side of (2.86) can be determined with the exponential integral function, defined as [19]:

$$\mathrm{Ei}(x) = \int_{-\infty}^{x}\frac{\mathrm{e}^{x'}}{x'}\mathrm{d}x', \quad x > 0. \tag{2.88}$$

For our problem, the integral domain is in the range $\zeta_0 = T_\mathrm{a}/T_0$ to $\zeta = T_\mathrm{a}/(T_\mathrm{f} - \Theta_k)$ or $\varepsilon_0 = T_\mathrm{a}/T_0 - T_\mathrm{a}/T_\mathrm{f}$ to $\varepsilon = T_\mathrm{a}/(T_\mathrm{f} - \Theta_k) - T_\mathrm{a}/T_\mathrm{f}$. Therefore,

$$\int_{\zeta_0}^{\zeta}\mathrm{e}^{\zeta'}\frac{\mathrm{d}\zeta'}{\zeta'} - \mathrm{e}^{\chi}\int_{\varepsilon_0}^{\varepsilon}\mathrm{e}^{\varepsilon'}\frac{\mathrm{d}\varepsilon'}{\varepsilon'} = \mathrm{Ei}(\zeta) - \mathrm{Ei}(\zeta_0) - \mathrm{e}^{\chi}\left[\mathrm{Ei}(\varepsilon) - \mathrm{Ei}(\varepsilon_0)\right]. \tag{2.89}$$

The implicit dependence of the density of defects can now be determined by substituting back the physical parameters into (2.89) to obtain the following analytic formula:

$$\frac{t}{\tau_{0,k}} = \mathrm{Ei}\left(\frac{T_\mathrm{a}}{T_\mathrm{f} - \Theta_k}\right) - \mathrm{Ei}\left(\frac{T_\mathrm{a}}{T_0}\right) + \exp\left(\frac{T_\mathrm{a}}{T_\mathrm{f}}\right)\left[\mathrm{Ei}\left(\frac{T_\mathrm{a}}{T_0} - \frac{T_\mathrm{a}}{T_\mathrm{f}}\right) - \mathrm{Ei}\left(\frac{T_\mathrm{a}}{T_\mathrm{f} - \Theta_k} - \frac{T_\mathrm{a}}{T_\mathrm{f}}\right)\right]. \tag{2.90}$$

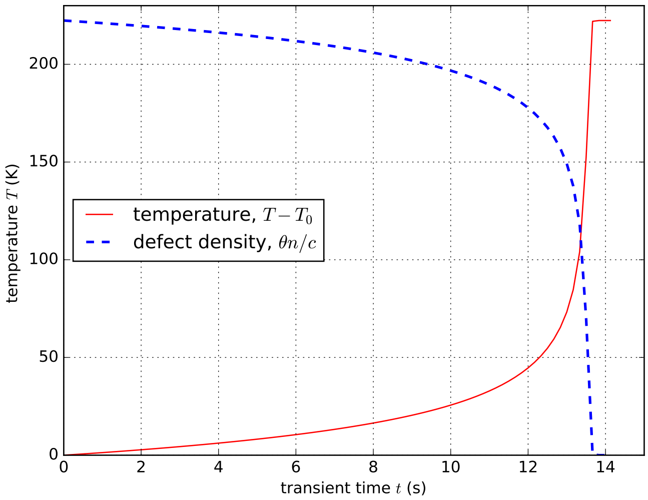

Figure 2.9: The decrease in defect density and increase in temperature in time in the process of spontaneous and homogeneous annealing.

The problem (2.82) has been previously solved in [3] and an implicit dependence of the sample temperature on time t in the case of homogeneous annealing was determined:

$$\frac{t}{\tau_{0,k}} = \mathrm{Ei}\left(\frac{T_\mathrm{a}}{T}\right) - \mathrm{Ei}\left(\frac{T_\mathrm{a}}{T_0}\right) + \exp\left(\frac{T_\mathrm{a}}{T_\mathrm{f}}\right)\left[\mathrm{Ei}\left(\frac{T_\mathrm{a}}{T_0} - \frac{T_\mathrm{a}}{T_\mathrm{f}}\right) - \mathrm{Ei}\left(\frac{T_\mathrm{a}}{T} - \frac{T_\mathrm{a}}{T_\mathrm{f}}\right)\right]. \tag{2.91}$$

Note that, alternatively, relationship (2.91) could be obtained from (2.90) by substitution $T_\mathrm{f} - \Theta_k = T$.

Figure 2.9 shows the dependence of temperature and defect density, expressed in temperature units by applying formula (2.77), on time calculated for homogeneous initial distributions of temperature and defect density $T_0 = 300\,\mathrm{K}$ and $n_0 = 6.63 \times 10^{26}/\mathrm{m}^3$, respectively, and for the energy released per one annealed defect $\theta_k = 5.4\,\mathrm{eV}$.

2.10.2 Heterogeneous annealing

Keeping in mind our formal definition of annealing as thermally activated relaxation processes in which the relaxation rate is temperature dependent, we investigate possible physical processes that may lead to in-homogeneous distributions of temperature in the irradiated material. This in-homogeneous distribution of temperature may result in the heterogeneous annealing of defects.

Heterogeneous annealing can be a result of one or all of the following factors:

1. Localised heat addition;
2. Localised fluctuations or instabilities;
3. In-homogeneous distribution of defects (i.e. defect clusters).

In the last part of this section we present a temperature model that incorporates the thermal contribution of in-homogeneously distributed defects.

Localised heat addition

If heat is added locally at the sample boundaries and the sample temperature is increased, then the defects will anneal faster in the localised region and this will result in an in-homogeneous distribution of defects. If we neglect the diffusion of the in-homogeneously distributed defects then the change of the defect density in time will be given by:

$$\frac{\partial n_k}{\partial t} = -\frac{n_k}{\tau_k}. \tag{2.92}$$

The local change in temperature will result in a transfer of heat in the sample as a result of a localised heat addition and the thermal energy released by annealing defects. If we consider a one dimensional geometry, for simplicity, then the temperature changes in time and space as follows:

$$c\frac{\partial T}{\partial t} = \kappa\frac{\partial^2 T}{\partial x^2} + \theta_k\frac{n_k}{\tau_k}, \tag{2.93}$$

where κ is the thermal conductivity of the material.

Equations (2.92) and (2.93) are similar to the governing equations for combustion waves in a premixed solid fuel in a one-dimensional configuration [20] and in [21].

Local instabilities

Even in an isolated system with a homogeneous distribution of defects and of temperature the defects may not anneal homogeneously. The homogeneous annealing may cease as a result of in-homogeneous perturbations of the defect density, $\delta n(x,t)$, and of the temperature, $\delta T(x,t)$ which can be described, according to [3], as follows:

$$\begin{aligned} \delta n_k(x,t) &= \delta n_k(t)\mathrm{e}^{\mathrm{i}kx}, \\ \delta T(x,t) &= \delta T(t)\mathrm{e}^{\mathrm{i}kx}, \end{aligned} \tag{2.94}$$

where $\mathrm{i} = \sqrt{-1}$ is the imaginary unit and k is the wavenumber and $n(t)$ and $T(t)$ are the solutions of the homogeneous coupled system (2.73) and (2.76).

Other studied effects that can lead to instabilities of a metastable state are the large amplitude oscillations of atoms about their equilibrium positions in the lattice. These oscillations cause local potentials of alternating sign, which are described in terms of time-periodic modulations of the potential barriers for chemical reactions taking place in the vicinity of the spatially localised vibrations, [22, 23, 24, 25, 26, 27]. The interplay of nonlinearity and the anharmonicity of these vibration (as a result of the discreteness of the lattice) can lead to the violation of the Arrhenius law; this violation is observed when chemical reactions occur at much lower temperatures than expected [26].

Thus far, we have only considered the irradiation of material in the nuclear regime which involves the displacement of lattice atoms and the formation of interstitials and vacancies. We have considered the thermal energy contribution of the interstitials and the vacancies to the irradiated material when they anneal or when they decay from clusters. However, there is another non-nuclear irradiation regime that can lead to a transfer of thermal energy in the irradiated material, and it is high energy heavy-ion irradiation. The collision energy of the heavy-ion projectile is transferred mainly to the target electrons and any structural changes are a result of energy and momentum transfer from the excited electrons to the lattice in the track, the so called *thermal spikes* [23, 28, 29, 30]. This may results in the enhancement of thermally activated processes (such as annealing) and therefore the contribution of the thermal spikes should also be taken into account in the modeling of the temperature changes in the irradiated material.

Defect Clusters

The thermal energy contribution from defect cluster decays (as a result of absorption of vacancies and interstitials by sinks or by vacancy-interstitial recombination) is another way in which heterogeneous annealing can occur. Equation (2.78) can be extended to include the thermal contribution from the cluster decays. A model that incorporates defect cluster thermal energy density contributions, with all physical parameters taken from the work of [3], is formulated as follows:

$$c\frac{\partial T}{\partial t} = \kappa\frac{\partial^2 T}{\partial x^2} + \frac{\theta_{\mathrm{i}} n_{\mathrm{i}}}{\tau_{\mathrm{i}}} + \frac{\theta_{\mathrm{v}} n_{\mathrm{v}}}{\tau_{\mathrm{v}}} - \sum_{k=2}^{m}\frac{\theta_k n_k}{\tau_k} + (\theta_{\mathrm{i}} + \theta_{\mathrm{v}})\,\gamma_1 n_{\mathrm{i}} n_{\mathrm{v}} + \sum_{k=2}^{m}(\theta_{\mathrm{i}} + \theta_{\mathrm{v}} - \theta_k)\,\gamma_k n_k n_{\mathrm{v}}. \tag{2.95}$$

Here $\tau_{\mathrm{i}}^{-1} = z_{\mathrm{i}}\rho_{\mathrm{d}} D_{\mathrm{i}}$ and $\tau_{\mathrm{v}}^{-1} = z_{\mathrm{v}}\rho_{\mathrm{d}} D_{\mathrm{v}}$ are the inverse lifetimes of interstitials and vacancies as they interact with sinks; $D_{\mathrm{i}} = D_{\mathrm{i}}^0 \exp(-E_{\mathrm{m}}^{\mathrm{i}}/k_{\mathrm{B}}T)$ (introduced in Section 2.8.3) and $D_{\mathrm{v}} = D_{\mathrm{v}}^0 \exp(-E_{\mathrm{m}}^{\mathrm{v}}/k_{\mathrm{B}}T)$ are the diffusion coefficients and $E_{\mathrm{m}}^{\mathrm{i}}$ and $E_{\mathrm{m}}^{\mathrm{v}}$ are migration energies for the interstitials and vacancies, respectively. The temperature dependent coefficient of vacancy recombination with a k-cluster is represented by γ_k. The energies released in absorption by a sink of an interstitial and a vacancy are represented by θ_{i} and θ_{v} respectively. θ_k is the thermal energy required to activate the emission of an interstitial by a k-cluster and its magnitude is approximately equal to the binding energy of an interstitial in a k-cluster.

2.11 Self-Sustained Annealing Wave

In this section we review previous studies of the self-sustained travelling wave of annealing in an infinite isolated system which is described by the following coupled system [3]:

$$\begin{aligned} \frac{\partial n}{\partial t} &= -\frac{n}{\tau}, \\ c\frac{\partial T}{\partial t} &= \kappa\frac{\partial^2 T}{\partial x^2} + \theta\frac{n}{\tau}. \end{aligned} \tag{2.96}$$

The coupled system (2.96) has been already introduced in Section 2.10 (equations 2.92 and 2.93); here we omit the k index which indicates the defect type, for simplicity.

We also review the derivation of the wave speed initiated at infinity and at the absolute zero temperature. The absolute zero initial temperature means that the relaxation time approaches infinity and the defects are in a stationary state. A condition that is crucial for the mathematical description of the travelling wave, since, as a result of annealing, the system transits from one stationary state to another [3]. This model is also commonly used to describe combustion waves [20, 31, 32].

To estimate the speed of the self-sustained annealing wave initiated at infinity we have to consider the propagation of the wave in a narrow region in the vicinity of the wave front, referred to as the *annealing front* in [3]. The speed of the annealing front, v, is defined as the volume of damaged material in which the defects are annealed per unit time per unit surface. To determine v we consider the coordinate system s in which the annealing front is at rest, defined as follows:

$$s = x - vt. \tag{2.97}$$

Then the coupled system (2.96) transforms into the following ordinary differential equation system:

$$\begin{aligned} -v\frac{\mathrm{d}n}{\mathrm{d}s} &= -\frac{n}{\tau}, \\ -vc\frac{\mathrm{d}T}{\mathrm{d}s} &= \kappa\frac{\mathrm{d}^2 T}{\mathrm{d}s^2} + \frac{\theta n}{\tau}. \end{aligned} \tag{2.98}$$

The boundary conditions are

$$\begin{aligned} s \to -\infty: &\qquad n = 0, &\qquad T = T_\infty, \\ s \to +\infty: &\qquad n = n_0, &\qquad T = 0. \end{aligned} \tag{2.99}$$

A rapid change of the temperature from T_∞ to 0 in the narrow region of the annealing zone is attributed more to the contribution from thermal conduction than advective heat flow. This means that the left-hand side of the second equation in (2.98) is negligible and so the equation can be simplified as follows:

$$\kappa \frac{\mathrm{d}^2 T}{\mathrm{d}s^2} + \frac{\theta n}{\tau} = 0. \tag{2.100}$$

Next, we make T the independent variable and make the substitution $\kappa \mathrm{d}T/\mathrm{d}s = \xi$ in (2.100), which yields:

$$\xi \frac{\mathrm{d}\xi}{\mathrm{d}T} + \kappa \frac{\theta n}{\tau} = 0. \tag{2.101}$$

Integrating (2.101) from 0 to T_∞ yields the heat flux from the annealing front,

$$\kappa \frac{\mathrm{d}T}{\mathrm{d}s} = \sqrt{2\kappa\theta \int_0^{T_\infty} \frac{n}{\tau} \mathrm{d}T}. \tag{2.102}$$

The total amount of heat released as a result of annealing per unit time and removed by the heat conduction, is equal to the energy stored in defects [3]. This heat is carried by the flow of un-annealed substance, and therefore we can write,

$$\sqrt{2\kappa\theta \int_0^{T_\infty} \frac{n}{\tau} \mathrm{d}T} = \theta n_0 v. \tag{2.103}$$

Therefore, the annealing front speed becomes

$$v = \frac{1}{n_0} \sqrt{\frac{2\kappa}{\theta} \int_0^{T_\infty} \frac{n}{\tau} \mathrm{d}T}. \tag{2.104}$$

From (2.104) we see that the speed of the annealing wave depends on the integral of the rate of heat production and is, therefore, associated with the activation energy and other kinetic characteristics of the damaged material.

Chapter 3

Mathematical Model of Self-Sustained Annealing

In this chapter we present a mathematical model for initiated annealing that results in a self-sustained annealing system as a result of the thermal concentration feedback and the heat conductivity in the sample with defects.

The finite one-dimensional model

To model the annealing process, we consider a sample having the form of a slab of thickness L, which is located in the region $0 < x < L$ and assumed to be infinite in lateral directions. Physical properties of material are assumed to be uniform all over the sample. The initial distribution of defects over the volume of the sample is assumed to be homogeneous with a density n_0. The initial temperature of the sample is T_0 everywhere except for a subsurface layer at $x = 0$ with a depth $\Delta x < L$, where the temperature is higher by an amount of ΔT due to initial heating. The initiating energy per unit surface area depends on the heating depth and the temperature increase as follows:

$$Q = c\Delta x\Delta T, \tag{3.1}$$

where c is the volumetric heat capacity of the material. In Figure 3.1, different initiation temperature distributions for different ΔT, for a constant initiating energy Q_0 are presented.

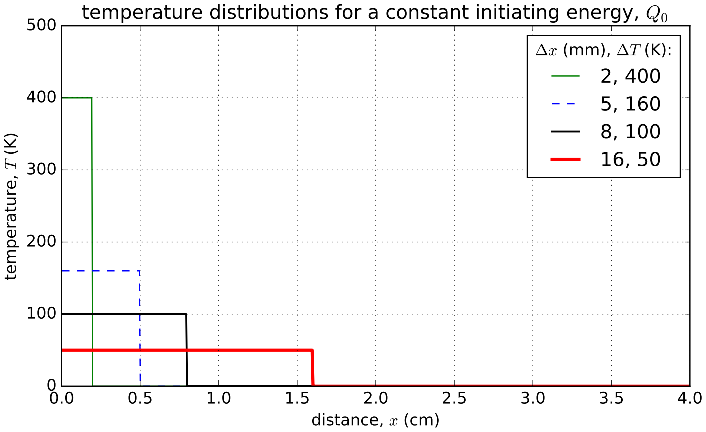

Figure 3.1: Different distributions of the annealing initiating temperature.

For the sake of simplicity we assume only one type of defects characterized by a single activation energy value E_a and material dependent parameter τ_0. In the process of annealing each defect releases an amount of energy, θ, which is approximately equal to the typical energies of formation of irradiation induced defects [33]. If there is only one defect present in the sample then we assume the thermally released energy into the sample is θ and if the number of defects in the sample is more than one, we neglect the energy of interaction of the defects and assume that the total energy released in the sample is θN (where $N > 1$ is the number of defects). This energy is released as heat and contributes to the increase of temperature in the sample, whose amplitude depends on the volumetric heat capacity of the material, c. As a result, the annealing rate of defects is increased according to the Arrhenius dependence introduced earlier in Section 2.9.3. Based on our modelling assumptions this dependence simplifies to

$$\tau^{-1} = \tau_0^{-1} \exp\left(-\frac{E_\mathrm{a}}{k_\mathrm{B}T}\right). \tag{3.2}$$

With this simplification the model for the heterogeneous self sustained annealing system, introduced before in Section 2.10, can be re-written as follows:

$$\begin{aligned} \frac{\partial n}{\partial t} &= -\frac{n}{\tau}, \\ c\frac{\partial T}{\partial t} &= \kappa\frac{\partial^2 T}{\partial x^2} + \theta\frac{n}{\tau}. \end{aligned} \tag{3.3}$$

We consider the sample to be thermally isolated, hence the coupled system (3.3) is solved subject to the zero-flux boundary conditions (note that boundary for defect flux is satisfied naturally, since the diffusion of defects is neglected in our model by applying the defect diffusion coefficient equal to zero, i.e. $D = 0$):

$$D\left.\frac{\partial n}{\partial x}\right|_{x=0} = D\left.\frac{\partial n}{\partial x}\right|_{x=L} = 0, \qquad \kappa\left.\frac{\partial T}{\partial x}\right|_{x=0} = \kappa\left.\frac{\partial T}{\partial x}\right|_{x=L} = 0, \tag{3.4}$$

and initial distributions of defect density and temperature (initial conditions):

$$\begin{aligned} n(t = 0, x) &= n_0, && 0 < x < L; \\ T(t = 0, x) &= \begin{cases} T_0 + \Delta T, & 0 < x < \Delta x; \\ T_0, & \Delta x < x < L. \end{cases} \end{aligned} \tag{3.5}$$

The initial temperature distribution in (3.5) is a mathematical implementation of the initiation temperature distribution indicated in Figure 3.1.

In previous studies of heterogeneous annealing [1], sample lengths greater than 10 cm and initial defect densities of order 10^{26} defects/m^3 have been considered and have been shown to be sufficient for modelling of self-sustained annealing in the sample. In our study we consider a sample of length $L = 13$ cm which is large enough for modelling of self-sustained annealing and sufficiently small to reduce the numeric computation time of results. The parameter values used in our study are summarised in Table 3.1.

Table 3.1: Values of parameters used in our study.

name	symbol	value
Defect activation energy	E_a	0.55 eV
Thermal energy released per annealing of one defect	θ	5.4 eV
Base case initial defect density	n_0	6.63×10^{26} defects/m^3
Material-dependent constant	τ_0	1×10^{-7} s
Thermal conductivity of aluminium	κ	220 W/(m K)
Volumetric heat capacity of aluminium	c	2.579×10^6 J/(K m^3)
Initial temperature of sample	T_0	300 K
Length of sample	L	13 cm
Melting temperature	T_melt	933 K

Chapter 4

Methods for the Numerical Solution of the Problem

In this chapter we discuss different methods that can be used to solve problem (3.2)–(3.3) subject to boundary conditions (3.4) and initial conditions (3.5). We apply a finite difference discretisation in space to turn our two coupled partial differential equations to a system of ordinary differential equations with respect to the temporal variable. This system is then integrated numerically by applying different algorithms, which include the Explicit Euler method, the fourth order Runge-Kutta method, and the first order Backward Differentiation method implemented in the Python `odeint` Package. The accuracy of the obtained numerical solution is verified by comparing it to an analytical solution for the homogeneous annealing of defects and by comparing solutions obtained with different algorithms.

4.1 Discretisation of the Model in Space

In this section we describe the finite difference scheme used to discretise the coupled system of partial differential equations (3.2)–(3.3) in space. To this end, we divide the problem domain of size L into N_p equal intervals as indicated in Figure 4.1. We attribute all the scalar material-related physical quantities (such as T, n, κ, c, etc.) to the middle of each interval with a coordinate x_j with indices $j = 1, \ldots, N_p$ [34]. Therefore quantities $n_j = n(x_j)$ and $T_j = T(x_j)$ describe the solutions at time t at a corresponding space point x_j. In these notations boundaries of each interval j are given by coordinates $x_{i-1/2}$ and $x_{i+1/2}$ in such a way that $x_{1/2} = 0$ and $x_{N_p+1/2} = L$. For the model parameter values of our study, a minimum interval number of $N_p = 1200$ was sufficient to produce converging solutions and the results were consistent for larger values, i.e. for $N_p > 1200$, hence $N_p = 1200$ was used throughout this study.

We use the central difference (CD) scheme in space to approximate the Laplace operator in the

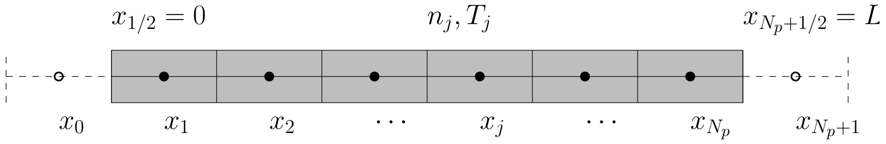

Figure 4.1: For N_p intervals, we implement a discretisation that maps the defect density and temperature values, n_j and T_j, in the middle of the j-th interval.

heat transfer equation (3.3):

$$\frac{\partial^2 T}{\partial x^2} \approx \frac{T_{j+1} - 2T_j + T_{j-1}}{h_x^2}, \tag{4.1}$$

where h_x is the mesh size and is given (for our equidistant mesh) by:

$$h_x = x_{j+1} - x_j = x_{j+1/2} - x_{j-1/2}. \tag{4.2}$$

The discretisation of the Laplacian term (4.1) involves non-existent points for indices $j = 1$ and $j = N_p$. In order to overcome this difficulty we introduce fictitious temperature points at the boundaries, namely T_0 at x_0 and T_{N_p+1} at x_{N_p+1} (see Figure 4.1) and apply the boundary conditions (3.4). We again use the central difference to approximate the derivative in (3.4) with respect to x:

$$\kappa \frac{T_j - T_{j-1}}{h_x} = 0 \quad \text{at } j = 1, \tag{4.3}$$

$$\kappa \frac{T_{j+1} - T_j}{h_x} = 0 \quad \text{at } j = N_p. \tag{4.4}$$

Discretised boundary conditions (4.3) and (4.4) mean that there is no spatial variation of temperature at these points, i.e. $T_0 = T_1$ and $T_{N_p} = T_{N_p+1}$. Substituting (4.3) and (4.4) to (4.1) yields the following spatial discretisation of our coupled system:

$$\begin{aligned}
\frac{\partial n_j}{\partial t} &= -\frac{n_j}{\tau_0} \exp\left(-\frac{T_\mathrm{a}}{T_j}\right), \qquad j = 1, \dots, N_p \\
\frac{\partial T_1}{\partial t} &= \frac{\kappa}{c h_x^2}(T_2 - T_1) + \frac{\theta}{c}\frac{n_j}{\tau_0} \exp\left(-\frac{T_\mathrm{a}}{T_j}\right), \\
\frac{\partial T_j}{\partial t} &= \frac{\kappa}{c h_x^2}(T_{j+1} - 2T_j + T_{j-1}) + \frac{\theta}{c}\frac{n_j}{\tau_0} \exp\left(-\frac{T_\mathrm{a}}{T_j}\right), \qquad j = 2, \dots, N_p - 1, \\
\frac{\partial T_{N_p}}{\partial t} &= \frac{\kappa}{c h_x^2}(T_{N_p-1} - T_{N_p}) + \frac{\theta}{c}\frac{n_j}{\tau_0} \exp\left(-\frac{T_\mathrm{a}}{T_j}\right).
\end{aligned} \tag{4.5}$$

For a time change from t to $t + \mathrm{d}t$ the defect density changes by an amount indicated by the right hand side of the first equation in (4.5) in each sub-volume at position x_j. For the interior points (shaded region in Figure 4.1), the change in the defect density n_j in each sub-volume at position x_j depends on both the defect density, n_j and on the temperature T_j in that sub-volume.

For the sub-volume temperatures, when the time changes from t to $t + \mathrm{d}t$ the temperature T_j at position x_j changes as a result of the heat transfer and therefore involves temperature values at neighbouring sub-volumes (T_{j-1} and T_{j+1}) and thermal energy contribution from annealing defects or defect density, as described by the second to the fourth equation in the coupled system (4.5).

The space discretisation as discussed in this section has allowed us to reduce a coupled system of two partial differential equations (PDEs) to a coupled system of $2N_p$ ordinary differential equations (ODEs). Solutions of the ODE system would allow one to obtain the evolution of the defect density and temperature distributions (profiles) in time. The system (4.5) does not have analytical solutions and we discuss ways to solve it numerically in Section 4.2.

4.2 Time Integration Methods

In this section we present a numeric integration in time used to produce solutions in space and time for the system (4.5) using forward difference (FD) and backward difference (BD) schemes, their combination called the theta method and the fourth order Runge-Kutta method.

We use indices $k = 0, \dots, N_t$ to represent the temporal mesh with a step size Δt defined as follows:

$$\Delta t = t_{k+1} - t_k. \tag{4.6}$$

We can organise the defect density and temperature values in each sub-volume into a $2N_p$-element vector $\boldsymbol{y}$ with $y_j = n_j$ and $y_{j+N_p} = T_j$ for $j = 1, \dots, N_p$, i.e.

$$\boldsymbol{y} = \begin{pmatrix} n_1 \\ \vdots \\ n_{N_p} \\ T_1 \\ \vdots \\ T_{N_p} \end{pmatrix}. \tag{4.7}$$

To represent the right-hand side of our coupled system, we use a vector function $\boldsymbol{f}(\boldsymbol{y})$ with components f_j ($j = 1, \dots, 2N_p$) defined as follows:

$$\begin{aligned}
f_j(\boldsymbol{y}) &= -\frac{y_j}{\tau_0} \exp\left(-\frac{T_\text{a}}{y_{j+N_p}}\right), && j = 1, \dots, N_p \\
f_j(\boldsymbol{y}) &= \frac{\kappa}{ch_x^2}(y_{j+1} - y_j) + \frac{\theta}{c}\frac{y_{j-N_p}}{\tau_0} \exp\left(-\frac{T_\text{a}}{y_j}\right), && j = N_p + 1 \\
f_j(\boldsymbol{y}) &= \frac{\kappa}{ch_x^2}(y_{j+1} - 2y_j + y_{j-1}) + \frac{\theta}{c}\frac{y_{j-N_p}}{\tau_0} \exp\left(-\frac{T_\text{a}}{y_j}\right), && j = N_p + 2, \dots, 2N_p - 1 \\
f_j(\boldsymbol{y}) &= \frac{\kappa}{ch_x^2}(y_{j-1} - y_j) + \frac{\theta}{c}\frac{y_{j-N_p}}{\tau_0} \exp\left(-\frac{T_\text{a}}{y_j}\right), && j = 2N_p
\end{aligned} \tag{4.8}$$

It is worth reminding that in (4.8) components corresponding to indices $j = N_p + 1$ and $j = 2N_p$ (the second and the fourth lines, respectively) incorporates the boundary conditions (4.3) and (4.4).

Specific solutions for the unknowns $n_j(t)$ and $T_j(t)$ depend on their initial values at $t = 0$ (that corresponds to index $k = 0$ of our time discretisation), i.e. on initial conditions (3.5) of the original PDE problem. For our spatial discretisation this gives $n_j^0 = n(t = 0, x_j)$ and $T_j^0 = T(t = 0, x_j)$. As before we organise them into a vector, $\boldsymbol{y}^0$, that contains initial values of the defect density and temperature:

$$\boldsymbol{y}^0 = \begin{pmatrix} n(t = 0, x_1) \\ \vdots \\ n(t = 0, x_{N_p}) \\ T(t = 0, x_1) \\ \vdots \\ T(t = 0, x_{N_p}) \end{pmatrix}. \tag{4.9}$$

Now we re-write the system of ODE in a general form which is more convenient for solving (integrating in time) the problem numerically with existing methods or solvers:

$$\frac{\mathrm{d}\boldsymbol{y}}{\mathrm{d}t} = \boldsymbol{f}(t, \boldsymbol{y}), \tag{4.10}$$

subject to the initial condition $\boldsymbol{y}(t = 0) = \boldsymbol{y}^0$.

In the next section we present three integration methods that can be used to solve our coupled system (4.10), namely, the Euler method, the theta method and the 4th-order Runge-Kutta method.

4.2.1 Euler method

The Euler method is an integration method that uses the first-order Taylor series expansion to approximate solutions of a differential equation in the neighbourhood of its variable t such that

$$\boldsymbol{y}(t+\Delta t)=\boldsymbol{y}(t)+\Delta t \boldsymbol{f}(t, \boldsymbol{y}). \tag{4.11}$$

Formula (4.11) is the general form of the forward difference (FD) approximation of the Euler method and is called the *explicit Euler method* (EEM) [35].

The accuracy of the EEM solutions depends heavily on the time step size Δt. For the parameters used in our problem, the EEM fails to produce accurate results for time step sizes that are greater than 10^{-4} s.

The advantage of the EEM (4.11) is that it is simple, easy to understand, easy to implement and less computationally costly than other methods when it is applicable [35]. Unfortunately, it suffers from low accuracy and instability when the time step, Δt, is not sufficiently small. However, reducing time step will increase the calculation time for solutions because it will increase the loop range in our algorithm (i.e. the range of the k indices, N_t).

An implicit form of the Euler method is less computationally expensive and can produce more accurate results. It is based on a backward finite difference (BD) approximation [34, 35, 19] and is expressed as follows:

$$\boldsymbol{y}(t+\Delta t)=\boldsymbol{y}(t)+\Delta t \boldsymbol{f}(t+\Delta t, \boldsymbol{y}(t+\Delta t)), \tag{4.12}$$

and is called the *implicit Euler method* (IEM). In the IEM the right-hand side of the ODE is evaluated at a later state at time $t+\Delta t$. Despite its advantages this method introduces additional difficulties. Since the method is implicit, a system of nonlinear equations must be solved at each time step.

4.2.2 Theta method

Another implicit method called θ_{m}-method, described in [34], evaluates the right-hand side of the ODE system at the current state at time t and later state at time $t+\Delta t$ as follows:

$$\boldsymbol{y}(t+\Delta t)=\boldsymbol{y}(t)+\Delta t\left[\theta_{\mathrm{m}} \boldsymbol{f}(t+\Delta t, \boldsymbol{y}(t+\Delta t))+(1-\theta_{\mathrm{m}}) \boldsymbol{f}(t, \boldsymbol{y}(t))\right], \tag{4.13}$$

where $\theta_{\mathrm{m}}=[0,1]$. If $\theta_{\mathrm{m}} \neq 0$ the method also requires solving a system of nonlinear equations at each time step. The method is first order accurate, except for the choice of $\theta_{\mathrm{m}}=1/2$, for which it is second order accurate.

4.2.3 Fourth-order Runge-Kutta method

The fourth-order Runge-Kutta method (RK4) is an approximation of the fourth order Taylor series expansion and is an extension of the Euler method. In the RK4, the time derivative function of the ODE is evaluated once at the initial point, twice at the trial midpoint and once at a final trial point as it is illustrated in Figure 4.2. For our system, these function evaluations are $2N_p$ dimension vectors described as follows:

$$\begin{aligned}
\boldsymbol{u}_1 &= \Delta t \boldsymbol{f}(t, \boldsymbol{y}(t)), \\
\boldsymbol{u}_2 &= \Delta t \boldsymbol{f}\left(t+\frac{\Delta t}{2}, \boldsymbol{y}(t)+\frac{\boldsymbol{u}_1}{2}\right), \\
\boldsymbol{u}_3 &= \Delta t \boldsymbol{f}\left(t+\frac{\Delta t}{2}, \boldsymbol{y}(t)+\frac{\boldsymbol{u}_2}{2}\right), \\
\boldsymbol{u}_4 &= \Delta t \boldsymbol{f}(t+\Delta t, \boldsymbol{y}(t)+\boldsymbol{u}_3).
\end{aligned} \tag{4.14}$$

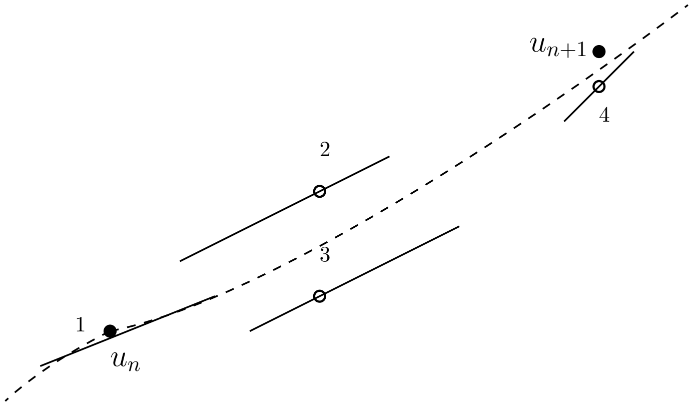

Figure 4.2: The fourth-order Runge-Kutta method extends the number of function evaluation in the Euler method. The function is evaluated once at the initial point, twice at trial midpoints and once at a trial end points. These functions are then summed to produce the final point u_{i+1} (filled dot).

The final function value is produced by a weighted sum of the four functions $\boldsymbol{u}_1$, $\boldsymbol{u}_2$, $\boldsymbol{u}_3$ and $\boldsymbol{u}_4$:

$$\boldsymbol{y}(t+\Delta t) = \boldsymbol{y}(t) + \frac{1}{6}\left[\boldsymbol{u}_1 + 2\boldsymbol{u}_2 + 2\boldsymbol{u}_3 + \boldsymbol{u}_4\right]. \tag{4.15}$$

The RK4 fails for time steps that are of order that is greater than 10^{-4} s for the parameters values used in our problem. Just like the EEM, the RK4 is computationally expensive for small mesh sizes. An implicit form of the RK4 method (i.e. IRK4) is based on a backward finite difference (BD) approximation [35]. The IRK4 can be used with larger mesh sizes than the explicit form of RK4 while producing equally accurate solutions.

4.3 Stiffness

Our coupled system involves two independent variables (time and space) in which one of the dependent variables (temperature) is second order in one of the variables, namely the space variable. This results in different scaling of the the two independent variables, problems of this nature are called *stiff* problems. Therefore, when solving the problem, implicitly or explicitly, the appropriate scaling of independent variables is necessary to avoid non-converging or oscillating solutions. For our problem the following scale range was sufficient to obtain non-oscillating solutions

$$\Delta t = \epsilon \frac{c {h_x}^2}{2\kappa}. \tag{4.16}$$

where $\epsilon = (0, 1]$. In cases where the smooth (accurate) solution also oscillates, the best way to improve the results is to reduce the mesh size to see if the solution converges further. Another, common and efficient way to reach convergence without reducing the mesh size is to use implicit integration methods.

4.4 Other Tools Used for Solving the Problem

In this section we discuss the solving tools used to integrate our differential equations. We discuss the advantage and disadvantage of each one and the justification for the solver that we used to produce our results in the summary, Section 4.4.3.

4.4.1 The Maple PDE Solver, pdsolve

The Maple solver for the Partial Differential Equations (PDE), `pdsolve`, has various built in algorithms for solving PDEs, see **Maple help** [36]. The solver needs one to specify the initial and boundary conditions, the solver recognises a certain number of PDE families that can be solved by using standard methods [37, 38, 39]. For PDEs that belong to unrecognised families, the `pdsolve` uses a heuristic algorithm that attempts separation of variables based on the specific PDE structure [40, 41, 42]. Optional arguments where one can give hints to the solver are also available. If the problem does not have an analytic solution, as in our case, one needs to include the option `numeric`. The default method used by the numeric `pdsolve` is a second order (in space and time) centred, implicit finite difference scheme in which the number of points in the stencil is one greater than the order of the equation, or each equation in the case of coupled PDE systems. There are also other optional finite difference schemes available, one available option suitable for our problem is the Crank-Nicolson scheme [43]. However, the optional or non-default schemes only handle single PDE (if they are not default) therefore to implement the optional schemes one would have to be more interactive with the Maple solver and supply the coupled system as a single PDE transformation. There is also the option, `stiff`, to handle stiff problem variables, however, one still needs to specify the independent variable step sizes in the space for optional arguments.

If one does not wish to complicate matters but simply wants to obtain accurate solutions by only supplying the solver with the differential equations to be solved and the required initial and boundary conditions, then the Maple solver is a reliable source. The main disadvantage is that the solutions take long times to be calculated; in that case one may need to implement their own efficient finite difference algorithm for the specific PDE, or ODE. This is possible to implement on the Maple command window. Another disadvantage of implementing your own solver on Maple is that the software contains many protected symbols and this restricts the freedom for naming parameters related to your problem.

In our research we compared the results that we implemented with our more time efficient algorithm with the results we obtained using Maple to verify our results.

4.4.2 The Python ODE Solver, odeint

The module `odeint`, written in Python, solves the initial value problem for stiff or non-stiff systems of first order ODEs [44]. The `odeint` solver takes in, as main parameters, the right-hand side of the coupled system which, in our case, is the vector function $\boldsymbol{f}(t, \boldsymbol{y})$ as described in (4.8) and the initial conditions contained in vector $\boldsymbol{y}^0$ as described in (4.9), and lastly a series of time points where the functions are to be evaluated [44]. Extra parameters have to be specified to produce accurate solutions. The most important extra parameters in our problem are the number of function evaluations and the order of the Taylor series expansion for approximating the solutions. The first order approximation for the Taylor series approximation was sufficient for our problem and produced relatively negligible errors.

The `odeint` solver can also be implemented in a loop, say in the case where one wants to investigate solutions for different initial conditions. However, the version up to Python 2.7 of the `odeint` solver, to our knowledge, does not take iterable array parameter inputs. To overcome this difficulty one can give the `odeint` function a string name in a conditional loop which updates the parameters that one wishes to vary.

4.4.3 Summary of the Maple and Python tools

As discussed in Section 4.4.1, although the Maple software allows one to solve a PDE system without implementing one's algorithm, the default methods are robust leading to long computation times. An interactive approach in Maple that allows one to optimise the computation times is necessary. Overall, our decision to proceed with our algorithm that was developed in Python was motivated by three reasons, the first being that the computation time for solutions was relatively faster with our own algorithm compared to the Maple solver; the second is that it was easier to implement additional algorithms for storage and analysis of previously calculated data in Python than in Maple; lastly the third reason was the verification of a small set of results that were calculated in both Maple and Python which showed agreement. In addition to the three main reasons is that the Python software is available on the web without financial cost to the user and is therefore easily accessible on more than one PC, where as the use of the Maple software requires purchase of the software and the license which, in addition to the cost, may also restrict the user to limited number of PCs to produce calculations.

4.5 Verification of Numerical Solutions

In Section 2.10.1 we determined the analytic solution for the implicit time dependence of the defect density and the temperature for homogeneous annealing (equations (2.90) and (2.91), respectively). We use, in this section, the analytic solution for homogeneous annealing as a standard reference to verify our numeric integrations, at least for the homogeneous annealing case. In Figure 4.3 we compare the solutions determined with the analytic formula and numerically with the RK4 method for the defect density dependence on time. We determined the RK4 numeric solutions to be close to the solution obtained with analytic formula (2.90), as shown in Figure 4.3

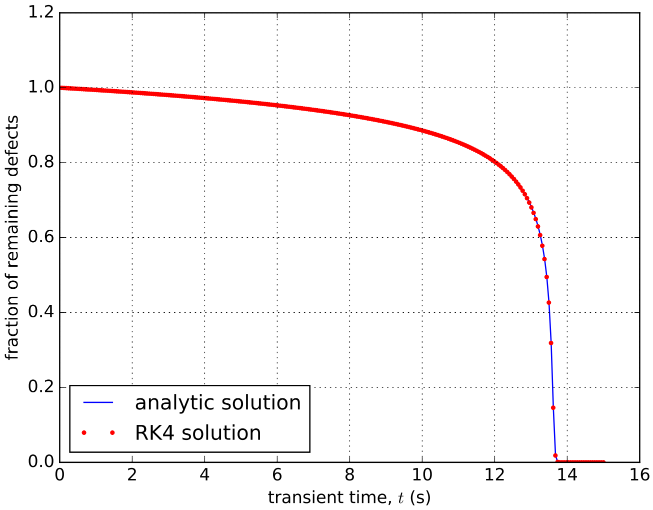

Figure 4.3: Comparison of solutions determined with analytic formula and numerically with the RK4 method for the normalised defect density (or fraction of remaining defects) dependence on time.

For heterogeneous annealing we compare the results determined with EEM, RK4 and the `odeint` solver. Our reasoning in verifying our numeric integrators is that since our ODE problem (4.10) is an initial value problem with unique solutions and the different methods mentioned are less likely to have the same truncation errors, if the solutions determined with the different methods are closely similar then the integration methods are accurate.

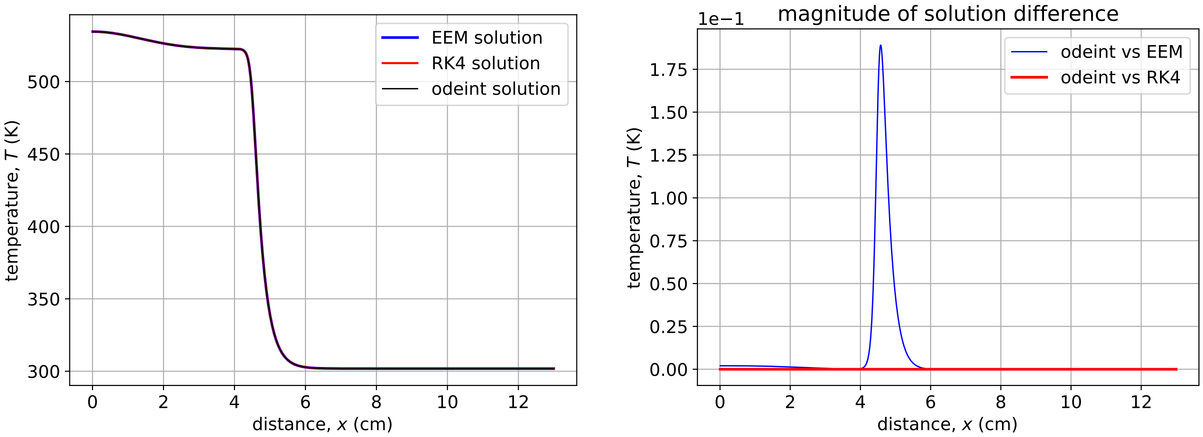

Figure 4.4: Comparison of solutions for the temperature profile determined numerically with the Explicit Euler, Runge-Kutta (4th order) methods and the `odeint` solver. The solutions show close similarity (left) with a negligible difference (right).

In Figure 4.4 (left) the similarity in the solutions determined with RK4, EEM and `odeint` solver is shown when the temporal and spatial meshes are less than order of magnitude of 10^{-5} s and 10^{-4} m, respectively. The solution difference of solutions determined with the `odeint` and the RK4 is negligible compared to the solution difference from the `odeint` and the EEM which is of order 2×10^{-1} K (that corresponds to relative error of approximately 4×10^{-2} %) for the temperature solutions as shown in In Figure 4.4 (right).

Since, therefore, the difference in the solutions determined with the `odeint` and RK4 (which is more accurate than the EEM) method is negligible, we opted to use the `odeint` solver to produce results in our study, for consistency.

Chapter 5

Results and Discussion

In this chapter we present the results of our study and their analysis. We start by discussing the development of self-sustained annealing in a sample of finite length. Next, we address different ways of initiation of the heterogeneous annealing of defects. In our study the self-sustained annealing can be initiated either heterogeneously when the temperature of the sample is increased uniformly over a given interval and locally near the sample boundary or homogeneously when the temperature of the sample is increased uniformly over the entire sample. The time required for the number of defects in the sample to reduce to a negligible value is referred to in our work as *annealing time*. The numerically calculated time for the defect to anneal homogeneously to negligible concentrations (annealing time) will be compared to the value determined with the analytic formula for the implicit dependence of the defect density on time for spontaneous annealing. After that we study the dependence of the annealing time on values of initiating parameters and initial conditions (i.e. initial temperature and initial defect density) for both the heterogeneous and homogeneous annealing. For some values of initiation parameters the annealing process can be realised in the form of a *travelling wave*. The travelling wave is a quasi-autowave, it is different from the autowave which is initiated in an infinite sample with initial temperature $T_0 = 0\,\mathrm{K}$. The travelling wave is initiated in a finite sample in the process of heterogeneous annealing and the initial temperature of the sample is greater than absolute zero, i.e. $T_0 > 0\,\mathrm{K}$. The speed of the travelling wave will be estimated from the annealing rate of defects in the sample and from the time the travelling wave traverses the entire length of the sample. The travelling wave can experience damping as a result of spontaneous annealing of defects, we conclude by studying this effect at high initial and uniform temperatures of the sample.

5.1 Self-Sustained Annealing in a Finite Sample

We discussed in Section 2.11, that in the self-sustained annealing wave regime the defects anneal in a narrow region near the annealing front called the *annealing zone*. This front separates the annealed region with an increased temperature from the damaged region of the material with a lower temperature, as it is illustrated in Figure 5.1. The width of the annealing zone and the speed of its propagation depend on the physical characteristics of the sample and on the density of defects. As one can observe in Figure 5.1 the density of defects in the annealing zone falls from its initial value to practically zero. It is interesting to note that the defect density curve in Figure 5.1 resembles and can be approximated by smooth sigmoidal functions which are discussed in detail in [45, 46].

The analytic model in Section 2.11 considers a frame of reference that is moving with the wave, i.e. the reference frame that is at rest and the self-sustained annealing wave (also referred to as

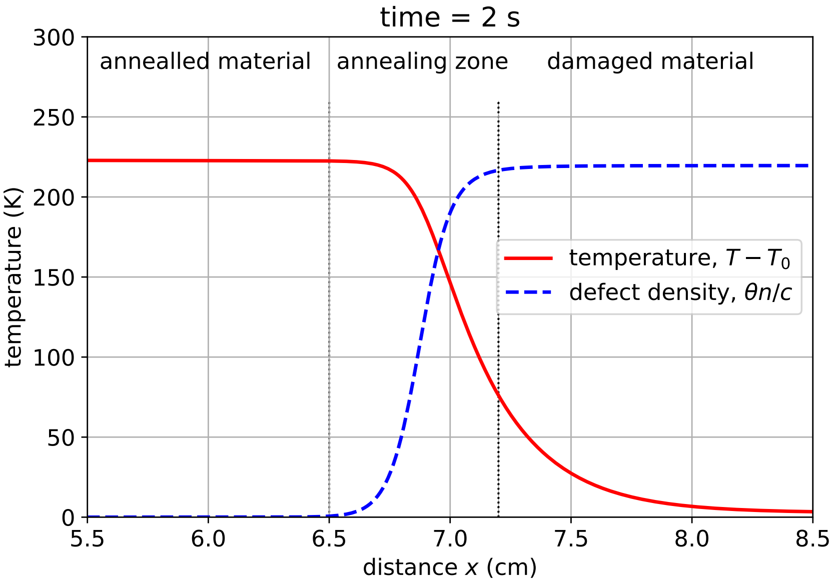

Figure 5.1: Schematic of the annealing wave front, propagating from the annealed material with an increased temperature to the damaged material with a lower temperature. Annealing happens predominantly in the area indicated as "annealing zone" [1].

autowave in that context) is assumed to be initiated at infinity far from observation. In a finite geometry[1], a quasi-wave regime of self-sustained annealing can be achieved in the interior region (i.e. in the region $0 < x < L$) of the sample under certain conditions that will be discussed later in this chapter.

The self-sustained annealing process in this finite geometry can be initiated at one boundary by increasing the temperature of the sample with defects in a localised region near the material surface. In the process of annealing, and for some initial distributions of temperature and defect density, the combined effect of the thermal concentration feedback (as a result of the energy released in the process of annealing) and the thermal conductivity, characterised by heat transfer coefficient, κ, may lead to the development of the self-sustained and self-propagating annealing process [47, 48], in which the annealing occurs in the form of a travelling wave, shown in Figure 5.2.

The example, presented in Figure 5.2, corresponds to the initiation temperature increase of $\Delta T = 200\,\mathrm{K}$ in a localised region of depth $\Delta x = 2\,\mathrm{mm}$ near the left boundary of the sample (represented by thick solid line in the figure). The defect density in this example and in the rest of the documents is expressed in units of temperature as $\Theta = \theta n/c$ – a quantity, which was defined earlier in (2.77), i.e. with amplitude proportional to the thermal energy released per annealing of one defect θ and inversely proportional to the volumetric heat capacity of the sample c, whose values are specified in Table 3.1 in Section 3.

In the interior region of the sample the travelling wave propagates at a constant speed, as one can see in Figure 5.2, where temperature and defect density profiles at equal time intervals appear to be equidistant in space. In addition, one can observe that in the inner region the shape of the temperature and defect density profiles does not significantly change. Furthermore, in the same figure it may be seen that at the boundaries the profile shapes and the uniformity of the travelling wave speed are disturbed. Since the heating depth of $\Delta x = 2\,\mathrm{mm}$ is much less than the length of

---

[1] As, for example, in a sample considered in this study, and which has the form of a slab of thickness L and is located in the region $0 < x < L$ and assumed to be infinite in lateral directions (see the model description in Chapter 3).

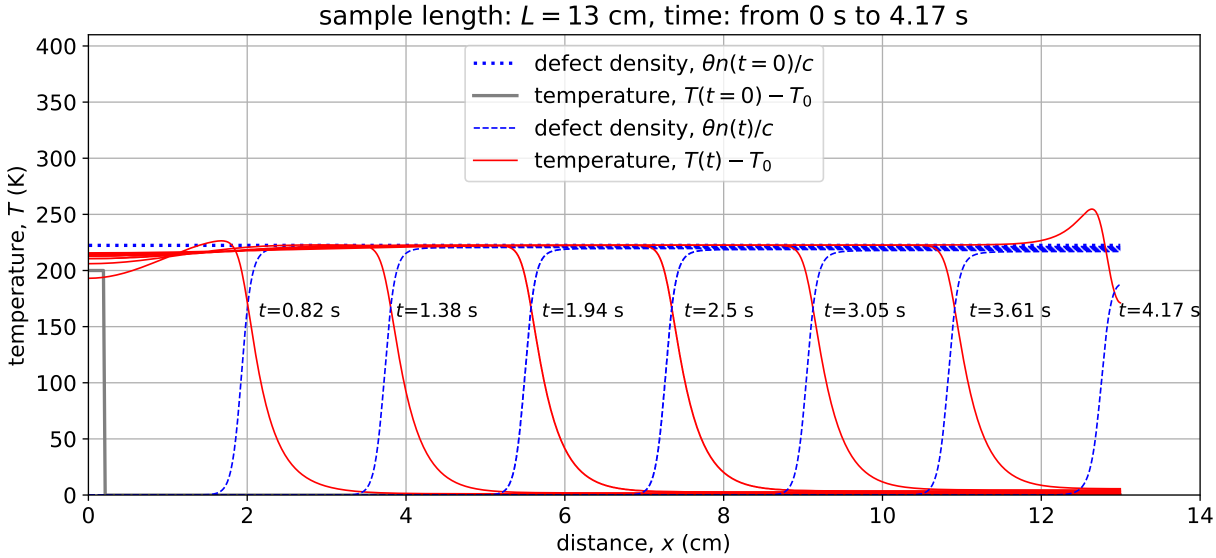

Figure 5.2: The temperature (solid line) and defect density (dashed line) profiles for an initiating temperature increase of $\Delta T = 200\,\mathrm{K}$ over a heating depth of $\Delta x = 2\,\mathrm{mm}$ calculated for different transient times from $t = 0.0\,\mathrm{s}$ to $t = 4.17\,\mathrm{s}$.

the sample $L = 13\,\mathrm{cm}$ in the considered example, the initiation boundary has a negligible effect on the travelling wave. At the right boundary the propagation of the travelling wave reaches a halt and the temperature increases near the boundary where the defects anneal faster as a result of the temperature increase because the generated heat cannot go further right beyond the thermally isolated boundary. Although it is not clearly visible in Figure 5.2 another pertubation effect on the travelling wave besides the boundaries is the damping effect from the spontaneous annealing of defects which will be discussed in Sections 5.3 and 5.4 and in more detail in the last section of this chapter, Section 5.9.

In this section we discussed the initiation of the travelling wave in a finite length sample as well some particularities of its propagation. The initiation temperature distribution presented in Figure 5.2 and discussed in this section is, however, only one of many possible distributions. In the next section (Section 5.2) we will discuss results for a small set of other possible initiation parameter combination that trigger a heterogeneous annealing of defects when the initiation energy is fixed.

5.2 Heterogeneous Annealing for a Fixed Initiating Energy

In this section we present results for different spatial distributions of the annealing initiating energy (per unit area), Q, introduced previously in Section 3 as follows:

$$Q = c\Delta x\Delta T. \tag{5.1}$$

Let us assume that the initiation energy is fixed to some given value Q_0. One can see from (5.1), that for a given material and a given initiating heat, Q_0, one can initiate annealing for different values of the parameters ΔT and Δx:

$$Q_0 = c\Delta x_m\Delta T_m, \quad m = 1, 2, \ldots,$$

where index m corresponds to different cases of annealing initiation. In this case the annealing initiation parameters Δx and ΔT should be such that the following condition is met:

$$\Delta x_m \Delta T_m = \Delta x_{m'} \Delta T_{m'} \quad \text{for any } m, m'. \tag{5.2}$$

As it was previously discussed in Chapters 2 and 3, the annealing rate of defects has the Arrhenius dependence on temperature (3.2), namely:

$$\frac{n}{\tau} = \frac{n}{\tau_0} \exp\left(-\frac{E_\mathrm{a}}{k_\mathrm{B} T}\right), \tag{5.3}$$

From an analysis of (5.3) one can expect, and this will be confirmed by results we report below, a larger temperature initiation value, say, ΔT_1 such that $\Delta T_1 > \Delta T_2$ will result in a higher annealing rate of defects at the corresponding heating depth Δx_1, and therefore a stronger positive feedback, compared to the temperature initiation value of ΔT_2 with a heating depth of Δx_2. Furthermore, since the temperature of the sample is time-dependent, the rate of defect annealing in the localised region of the sample where the temperature is increased by amount ΔT, is also time-dependent. Therefore, the rate of defect annealing depends on the temperature increase in a localised region of the sample, ΔT, and the time of the transient.

To investigate this dependence we consider, as example, a case in which $Q_0 = 2063.20\,\mathrm{kJ/m^2}$ and four variants of temperature increase: 100 K, 160 K, 320 K and 400 K, at the respective heating depths such that the condition (5.2) is met and Q_0 remains unchanged (8.0 mm, 5.0 mm, 2.5 mm and 2.0 mm, respectively). For these combinations of ΔT and Δx, we have calculated temperature and defect density profiles at time $t = 0.5$ ms. The results of the calculation, along with the corresponding temperature and defect density profiles at $t = 0.0$ ms (initial distributions), are presented in Figure 5.3.

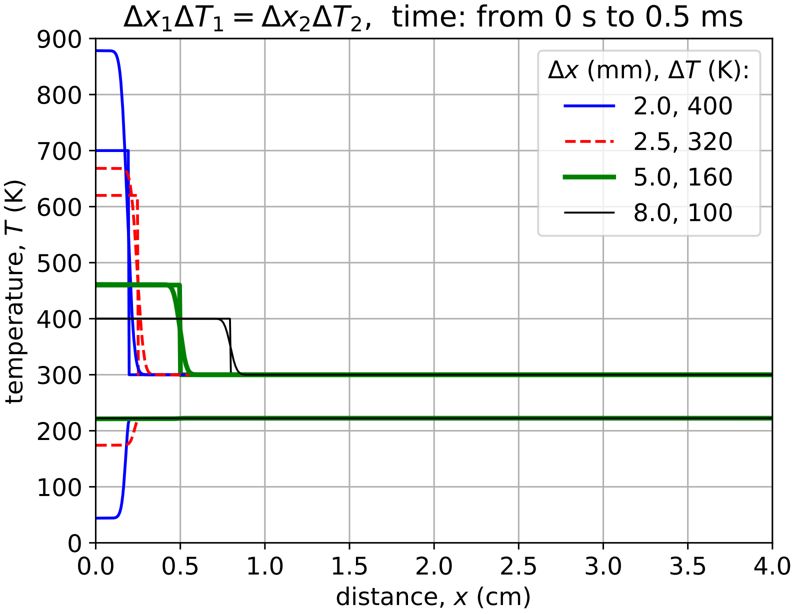

Figure 5.3: The annealing of defects (bottom) near the initiation boundary and the temperature increase (top), as a result of the positive feedback, for different initiation temperature ΔT_m and heating depth Δx_m values under the condition $\Delta x_m \Delta T_m = \Delta x_{m'} \Delta T_{m'}$. The temperature and defect density profiles are given for $t = 0.0$ ms and $t = 0.5$ ms.

As one can see in Figure 5.3, the temperature increase of $\Delta T = 100\,\mathrm{K}$ and $\Delta T = 160\,\mathrm{K}$ (at a heating depth of $\Delta x = 8\,\mathrm{mm}$ and $\Delta x = 5\,\mathrm{mm}$, respectively) is insufficient to trigger a notable annealing of defects near the boundary in the very early moments of the transient. However, for higher initiation temperature increases (for the same initiation energy Q_0) of, say, $\Delta T = 320\,\mathrm{K}$ and above (respectively for $\Delta x = 2.5\,\mathrm{mm}$ and below) the annealing of defects can be detected by observing a significant increase of temperature and decrease of defect density at 0.5 ms. One can also observe in Figure 5.3 that defect anneal fastest for the highest initiating temperature of $\Delta T = 400\,\mathrm{K}$, with a heating depth of $\Delta x = 2\,\mathrm{mm}$.

The same set of calculations was also performed for a longer transient time of 0.1 s and results are presented in Figure 5.4. In this figure the amount of annealed defects has significantly increased, predominantly near the initiation boundary. This holds for all considered initiating combinations with the given Q_0, including the initiation temperature increases of $\Delta T = 100\,\mathrm{K}$ and $\Delta T = 160\,\mathrm{K}$. One can also observe in Figure 5.4, that for ΔT above 100 K the temperature and defect density profiles almost overlap and the defects have annealed to a negligible concentration up to approximately 5 mm in depth.

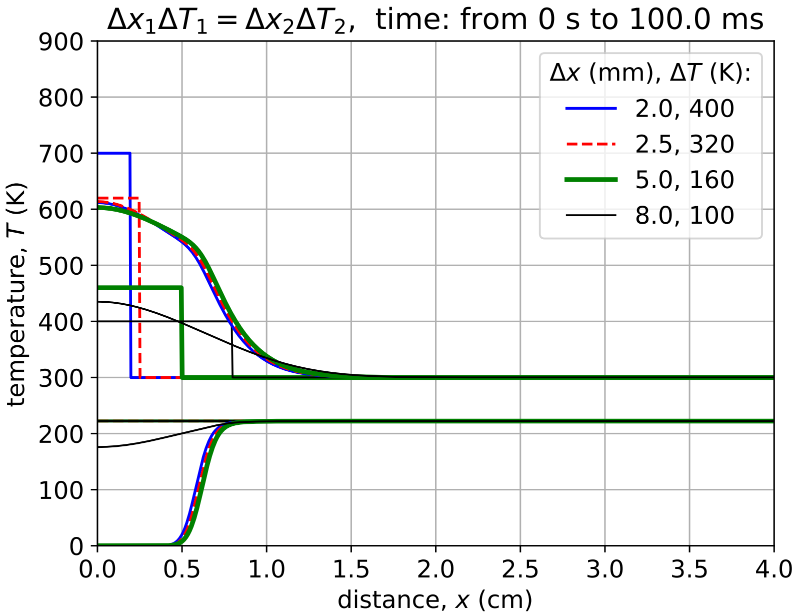

Figure 5.4: The temperature (top) and defect density profiles (bottom) with the similar annealing initiation temperature distributions of Figure 5.3. The temperature and defect density profiles are given for $t = 0.0\,\mathrm{ms}$ and $t = 100.0\,\mathrm{ms}$.

Subsequently at transient times close to or much longer than the relaxation time of the annealing process, the defects will start to anneal heterogeneously to negligible concentrations for all considered: initiation temperatures 100 K, 160 K, 320 K and 400 K at their respective heating depths and a self-sustained and self-propagating heterogeneous annealing process will develop as shown in Figure 5.5, in which results of calculations for further time of 0.5 s are given. Although the self-propagating annealing regime is achieved with all the initiation distributions for the temperatures, the time for all the defects to anneal heterogeneously in the sample still depends on the initiation temperature distribution. For a localised temperature increase of $\Delta T = 100\,\mathrm{K}$ the defects will take a longer time to anneal to negligible concentrations compared to other considered localised initiation temperatures, as can be seen in Figure 5.5 where the annealing propagation front corresponding to the initiation temperature of $\Delta T = 100\,\mathrm{K}$ is lagging behind the propagation fronts for other initiation temperature increases at their respective heating depths.

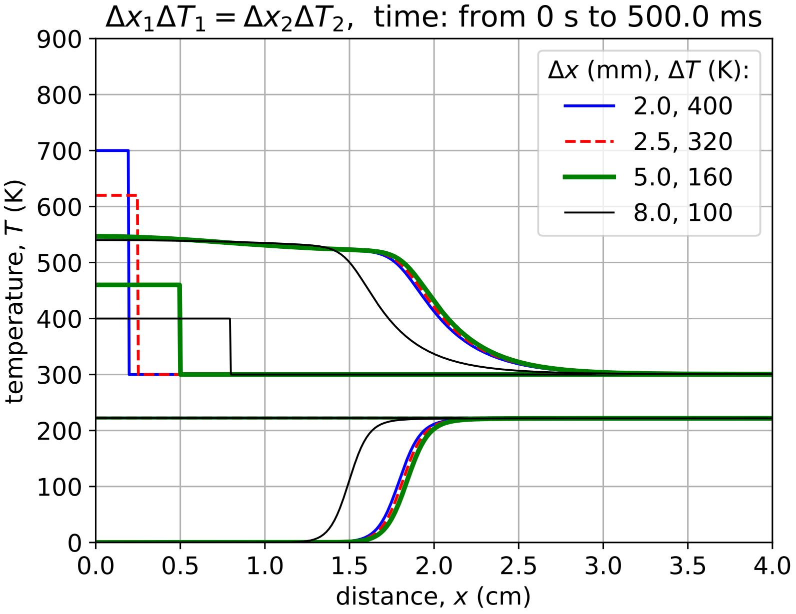

Figure 5.5: The temperature (top) and defect density profiles (bottom) with the similar annealing initiation temperature distributions of Figure 5.3. The temperature and defect density profiles are given for $t = 0.0\,\text{ms}$ and $t = 500.0\,\text{ms}$.

It is worth mentioning that, for given values of the initiation energy, Q_0, and heating depth, Δx, the temperature increase ΔT also depends on the specific (or volumetric) heat capacity of the material. A lower heat capacity of the material means that the temperature increase of the sample as a result of the energy released from annealed defects, and which has a magnitude $\theta n_0/c$, is higher for material with lower heat capacities. Our model becomes invalid if this temperature increase exceeds the melting temperature of the material because it does not account for phase changes. However, the reference initial density of defects and the volumetric heat capacity are chosen in this section in such a way that the temperature increase from the energy released from annealed defects is 222.58 K as one can clearly see from the concentration swing in Figures 5.3 and 5.4 (bottom curves). This value is way below the melting temperature of our sample model which is assumed to have material parameters of aluminium (see Table 3.1 for details). We also make sure that we do not reach melting temperatures in the rest of this study.

The main observation of this section is the dependence of the defect annealing rate on the temperature increase for different moments in time, that the defect annealing rate can increase with both temperature and time. This observation is in agreement with (5.3) and gives us a strong reason to include the time aspect in our investigation of heterogeneous annealing of defects especially at long transient times. Since the initial temperature of our the sample is uniform and above absolute zero, at long transient times the the spontaneous annealing of defects all over the whole sample may play significantly and its contribution increases with time increases with time. In the next section we investigate the heterogeneous annealing of defects for different initiation parameters and at different transient times.

5.3 Dependence of the Character of the Self-Sustained Annealing on the Initiating Temperature for a Given Heating Depth

In this section we investigate the self-sustained and self-propagating heterogeneous annealing of defects for different initiation temperatures for a heating depth of $\Delta x = 2\,\text{mm}$. More specifically, we investigate heterogeneous annealing for annealing initiation parameters given in Table 5.1. Furthermore, we clearly establish the conditions where the travelling wave regime of annealing is achieved and where it is not achieved (both in this section and in the next one, Section 5.4) from the analysis of the temperature and defect density profiles for the initiation parameters in Table 5.1. The maximum temperature increase is again selected so as to not exceed a final temperature that exceeds the melting temperature of aluminium whose physical parameters are used in our model.

Table 5.1: Energy values for different initiation parameters: the study of the dependence of the self-sustained annealing on the initiating temperature for a given heating depth.

Initiation energy, Q (kJ/m^2)	heating depth, Δx (mm)	temperature increase, ΔT (K)
412.64	2	80
618.96	2	120
825.28	2	160
1237.92	2	240
1444.24	2	280
2063.20	2	400

As observed and discussed in Section 5.2, the annealing rate has a temperature and time dependence. Consequently, a heterogeneous annealing of defects will not only vary in space but will also vary in time. Therefore, in order to facilitate the analysis of results, in our study here we choose different maximum transient times for studying the development of a self-sustained annealing process corresponding to different initiation distributions.

For initiation temperature increase of $\Delta T = 80\,\text{K}$ and $\Delta T = 120\,\text{K}$, with a heating depth of $\Delta x = 2\,\text{mm}$ the defect annealing rate is slow in the initial moments of the transient and is mostly determined by spontaneous annealing. The heterogeneous and self-sustained annealing is realised at long transient times close to 11.5 s in the first case and 10.0 s in the second one, as can be observed in Figures 5.6 and 5.7. For an initiation temperature increase of $\Delta T = 160\,\text{K}$ at the same heating depth the heterogeneous and self-sustained annealing regime is realised at transient times close to 7.4 s, as shown in Figure 5.8.

Unlike the profiles for the travelling wave of annealing shown in Figure 5.2 of Section 5.1 the temperature and defect density profiles in Figures 5.6 to 5.8 have dissimilar shapes in the interior region of the sample. The dissimilar profiles reflect the change in time of the manner of the heterogeneous annealing which is observable at long transient times. This also reflects/means that the travelling wave regime of annealing is not achieved. The damping effect on the temperature and defect density profiles is as a result of the spontaneous annealing of defects which starts to dominate at relatively long transient times closer to 13.63 s, as will be discussed in detail in Section 5.9.

For the initiation temperatures, $\Delta T = 240\,\text{K}$, $\Delta T = 280\,\text{K}$ and $\Delta T = 400\,\text{K}$, with a heating depth of $\Delta x = 2\,\text{mm}$, the temperature and defect density profiles look similar in the interior region of the sample and so the progress of heterogeneous annealing almost does not change in time, as can be seen in Figures 5.9 to 5.11. This means that the travelling wave regime has been achieved and

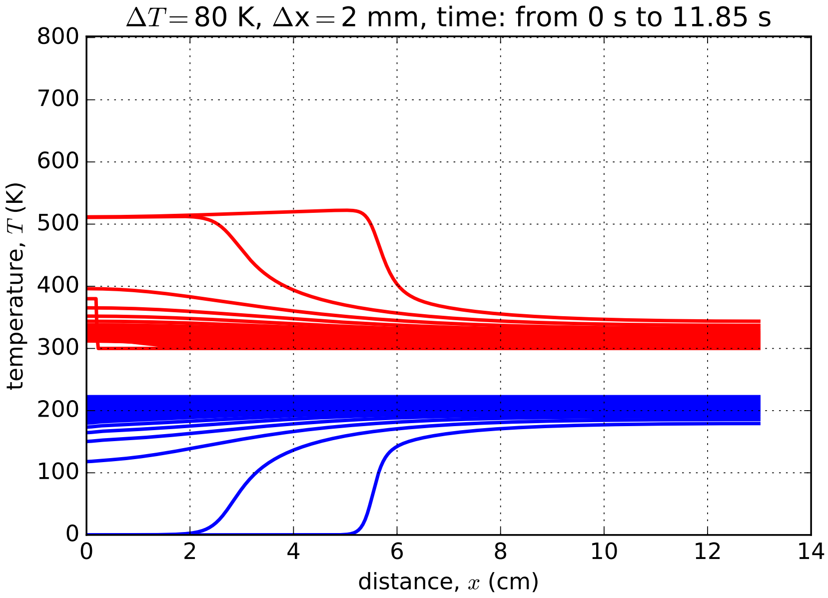

Figure 5.6: The temperature (top) and defect density (bottom) propagation fronts for an initiating temperature increase of $\Delta T = 80\,\mathrm{K}$, with a heating depth of $\Delta x = 2\,\mathrm{mm}$ for a maximum transient time interval of 11.85 s.

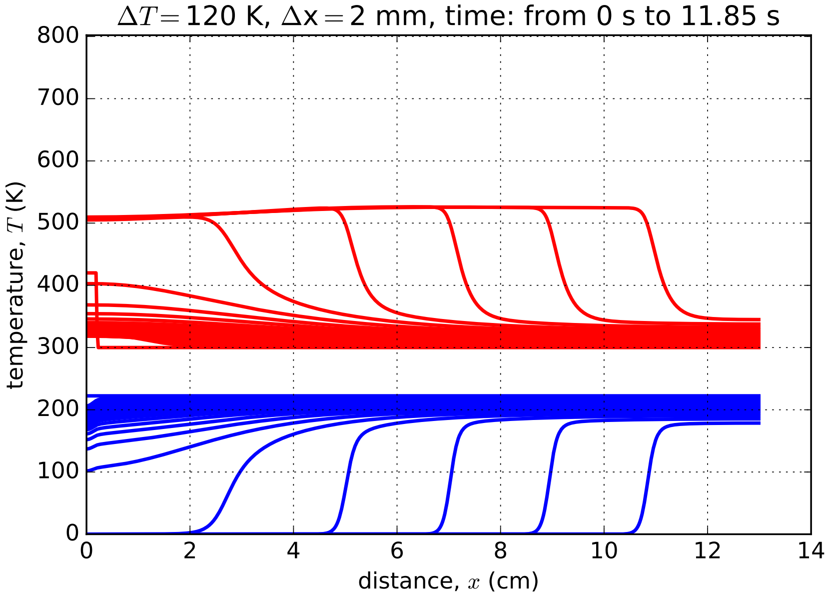

Figure 5.7: The temperature (top) and defect density (bottom) propagation fronts for an initiating temperature increase of $\Delta T = 120\,\mathrm{K}$, with a heating depth of $\Delta x = 2\,\mathrm{mm}$, calculated for a maximum transient time interval of 11.85 s.

the transient time at which the regime is observed, which is up to 1.85 s in Figures 5.9 to 5.11, is relatively earlier than the transient times at which spontaneous annealing starts to dominate.

The initiation energies corresponding to temperature increases 240 K, 280 K and 400 K, with a heating depth of 2 mm are shown in Table 5.1 and there we see that for our chosen initiation parameters, ΔT and Δx, the minimum initiation energy that leads to the development of the travelling wave is $1237.92\,\mathrm{J/m^2}$. The lowest initiation energy in Table 5.1 is $412.64\,\mathrm{J/m^2}$ and it

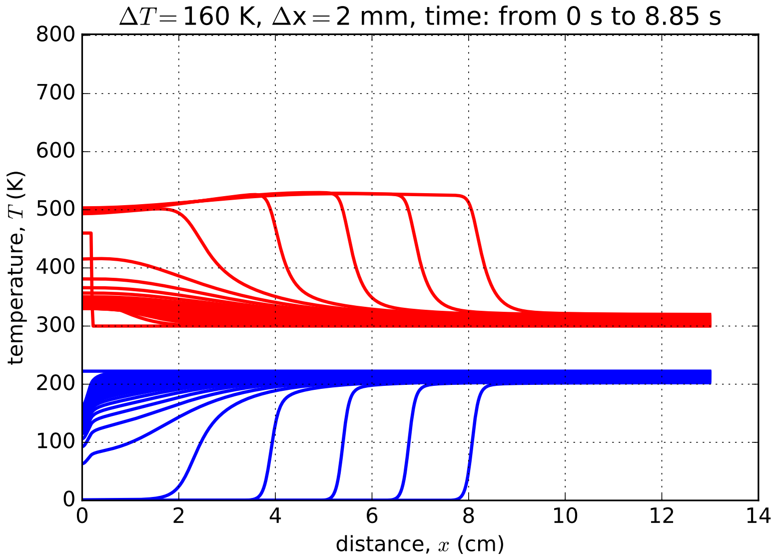

Figure 5.8: The temperature (top) and defect density (bottom) propagation fronts for an initiating temperature increase of $\Delta T = 160\,\mathrm{K}$, with a heating depth of $\Delta x = 2\,\mathrm{mm}$, calculated for a maximum transient time interval of 8.85 s.

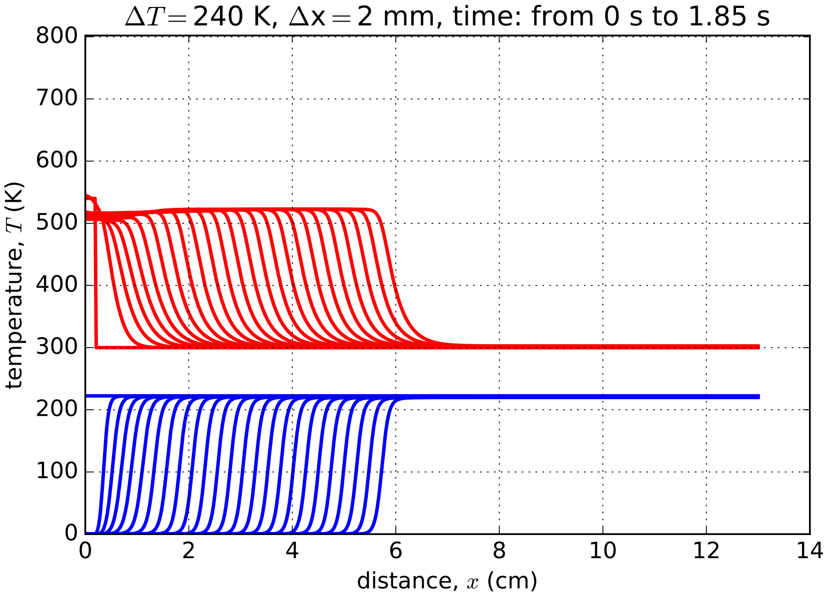

Figure 5.9: The temperature (top) and defect density (bottom) propagation fronts for an initiating temperature increase of $\Delta T = 240\,\mathrm{K}$, with a heating depth of $\Delta x = 2\,\mathrm{mm}$, calculated for a maximum transient time interval of 1.85 s.

corresponds to the initiation temperature of $\Delta T = 80\,\mathrm{K}$, with a heating depth of $\Delta x = 2\,\mathrm{mm}$. In the next section we increase the initiation energy corresponding to $\Delta T = 80\,\mathrm{K}$ by increasing the sample temperature by this amount over a larger volume, i.e. we increase Δx.

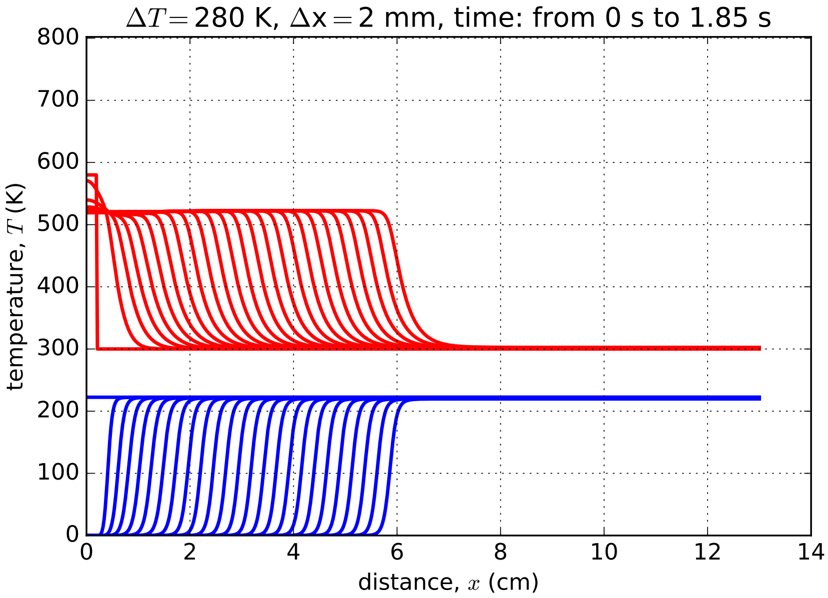

Figure 5.10: The temperature (top) and defect density (bottom) propagation fronts for an initiating temperature increase of ΔT = 280 K, with a heating depth of Δx = 2 mm, calculated for a maximum transient time interval of 1.85 s.

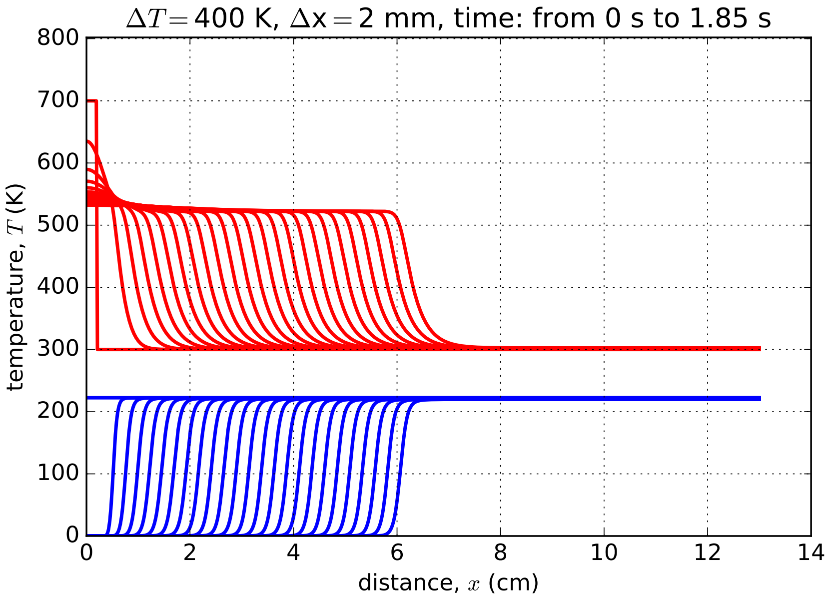

Figure 5.11: The temperature (top) and defect density (bottom) propagation fronts for an initiating temperature increase of ΔT = 400 K, with a heating depth of Δx = 2 mm, calculated for a maximum transient time interval of 1.85 s.

5.4 Dependence of the Character of the Self-Sustained Annealing on the Heating Depth for Given Initiating Temperatures

In this section we investigate the heterogeneous annealing of defects when the initiation temperature is increased by $\Delta T = 40\,\mathrm{K}$ and $\Delta T = 80\,\mathrm{K}$ in a localised region of the sample. As mentioned in Section 5.2, a higher temperature increase in a localised region of the sample (as long as it does not exceed the melting temperature of the sample) leads to a faster heterogeneous annealing of defects by means of a travelling wave. However, it is preferable to investigate a minimal initiating temperature increase which reduces the chance of damage of the material characteristic properties. The parameters of the initial heating selected to be used in the study discussed in this section are summarised in Table 5.2.

Table 5.2: Energy values for different initiation parameters: the study of the dependence of the self-sustained annealing on the heating depth for given initiating temperatures.

Initiation energy, Q (kJ/m^2)	heating depth, Δx (mm)	temperature increase, ΔT (K)
825.28	4	80
1237.92	6	80
1650.56	8	80
2475.84	12	80
3301.12	16	80
4126.40	40	40

After performing a simulation of annealing with parameters from Table 5.2, we have found that an initiation temperature increase of $\Delta T = 80\,\mathrm{K}$ is sufficient for the effective or fast annealing of defects by means of the travelling wave at heating depths of $\Delta x = 12\,\mathrm{mm}$ and higher, i.e. for $\Delta x = 16\,\mathrm{mm}$.

The initiation energies corresponding to a temperature increase of $\Delta T = 80\,\mathrm{K}$ at heating depths of $\Delta x = 8\,\mathrm{mm}$, $\Delta x = 12\,\mathrm{mm}$ and $\Delta x = 16\,\mathrm{mm}$ in our sample are $1650.56\,\mathrm{kJ/m^2}$, $2475.84\,\mathrm{kJ/m^2}$ and $3301.12\,\mathrm{kJ/m^2}$ respectively, as indicated in Table 5.2, studied in the previous section. These initiation energies are higher than the minimum initiation energy required for effective or fast annealing of defects when the initiation parameters are $T = 240\,\mathrm{K}$ and $\Delta x = 2\,\mathrm{mm}$, which is $1237.92\,\mathrm{kJ/m^2}$. The results of annealing modelling up to transient times close to 1.85 s is presented in Figures 5.12 to 5.14, respectively. One can notice in these figures the that heterogeneous annealing of defects by means of the travelling wave is already realised by this time in all these cases.

If we reduce the initiation temperature to $\Delta T = 40\,\mathrm{K}$, the heating depth has to be extended to $\Delta x = 40\,\mathrm{mm}$ for the travelling wave regime of annealing of defects to be realised at transient times close to 1.85 s, as it is illustrated in Figure 5.15.

For a heating depth of $\Delta x = 6\,\mathrm{mm}$ the travelling wave regime of heterogeneous self-sustained annealing is realised at a transient time of 4.85 s, as one can observe in Figure 5.16. At heating depths equal to or lower than $\Delta x = 4\,\mathrm{mm}$ the travelling wave regime is achieved at longer transient times of 8.85 s or greater, as can be seen in Figure 5.17.

In this section and in Sections 5.1 and 5.3 we investigated the heterogeneous annealing of defects for a chosen set of different initiation parameters ΔT and Δx and have shown that the shape of the temperature and defect density profiles changes in time, due to boundary and initial conditions and when the spontaneous annealing regime of defects (which occurs without initiation) starts to

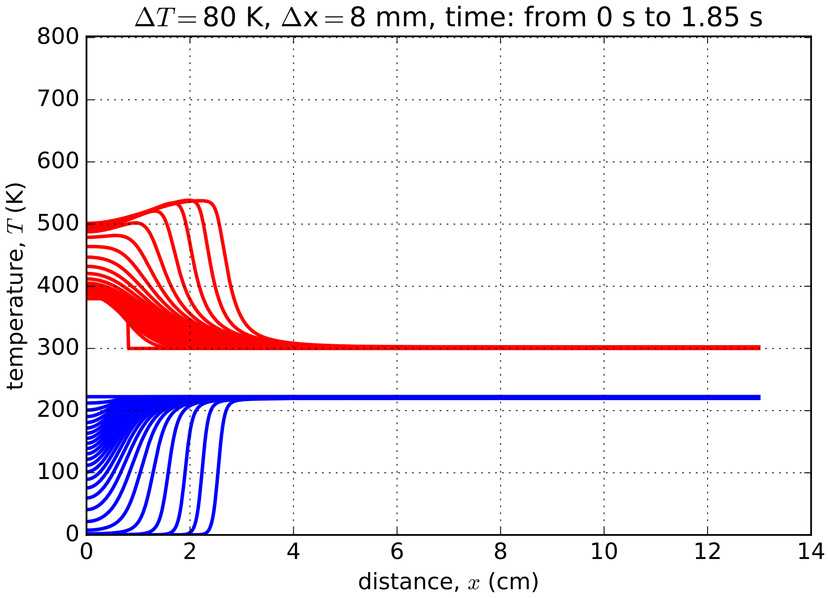

Figure 5.12: The temperature (top) and defect density (bottom) propagation fronts for an initiating temperature increase of ΔT = 80 K, with a heating depth of Δx = 8 mm, calculated for a maximum transient time interval of 1.85 s.

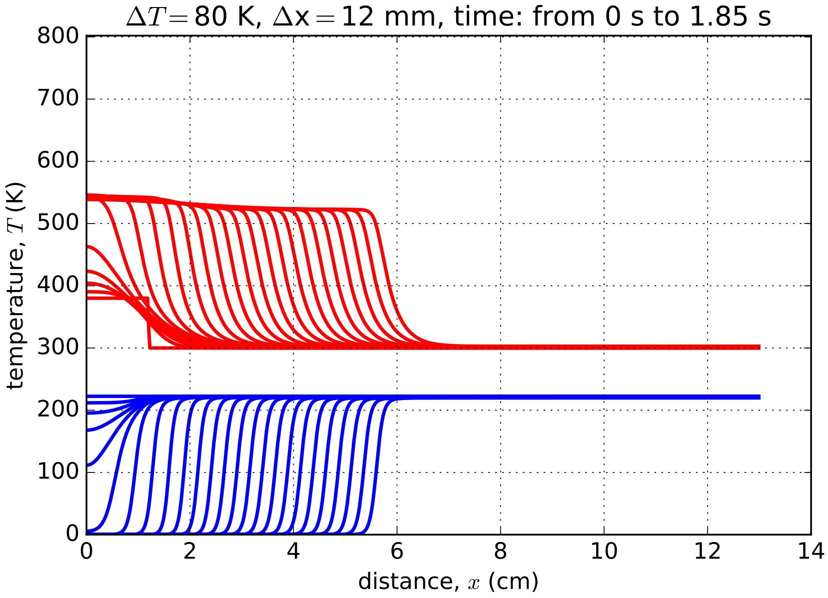

Figure 5.13: The temperature (top) and defect density (bottom) propagation fronts for a temperature increase of ΔT = 80 K, with a heating depth of Δx = 12 mm, calculated for a maximum transient time interval of 1.85 s.

dominate. In the next section, Section 5.5, we discuss in detail the shape of the temperature and defect density profiles in the annealing zone when the initial temperature and initial density of defects are changed.

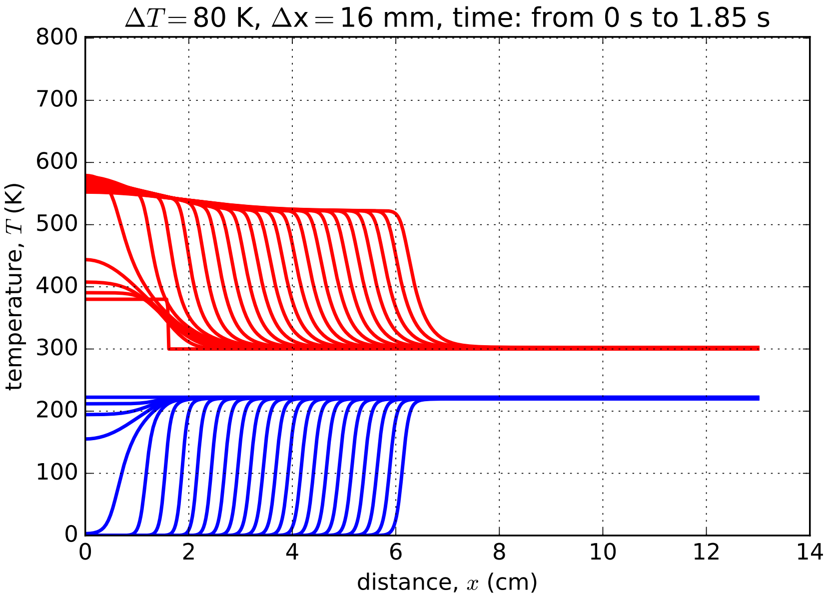

Figure 5.14: The temperature (top) and defect density (bottom) propagation fronts for a temperature increase of $\Delta T = 80$ K, with a heating depth of $\Delta x = 16$ mm, calculated for a maximum transient time interval of 1.85 s.

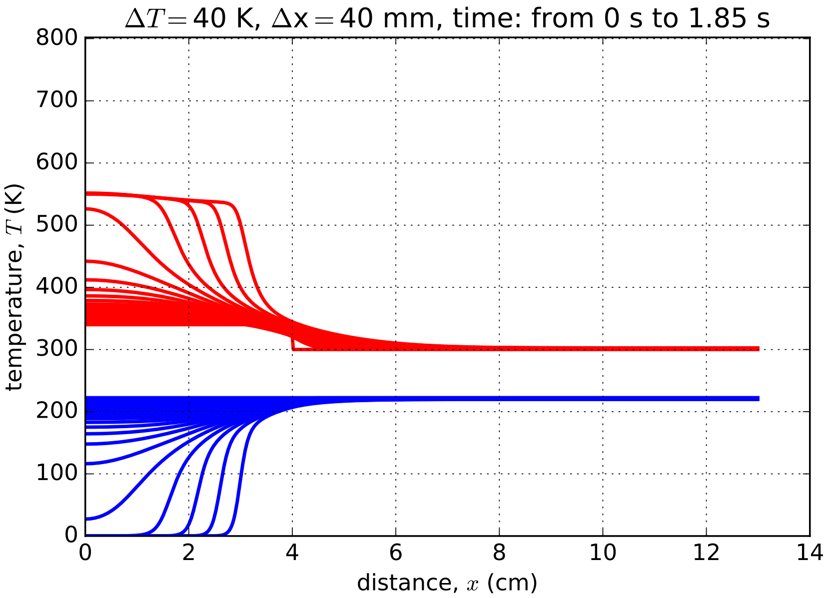

Figure 5.15: The temperature (top) and defect density (bottom) propagation fronts for a temperature increase of $\Delta T = 40$ K, with a heating depth of $\Delta x = 40$ mm, calculated for a maximum transient time interval of 1.85 s.

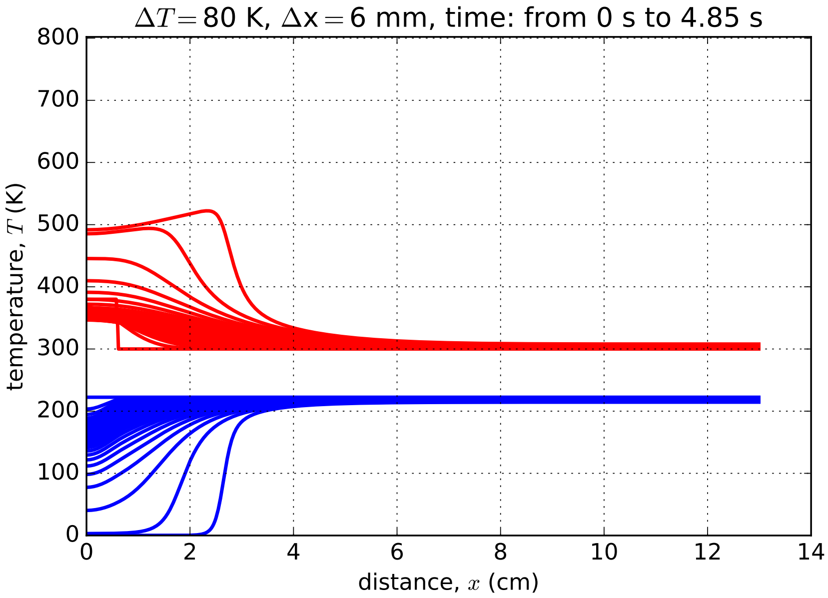

Figure 5.16: The temperature (top) and defect density (bottom) propagation fronts for a temperature increase of ΔT = 80 K, with a heating depth of Δx = 6 mm, calculated for a maximum transient time interval of 4.85 s.

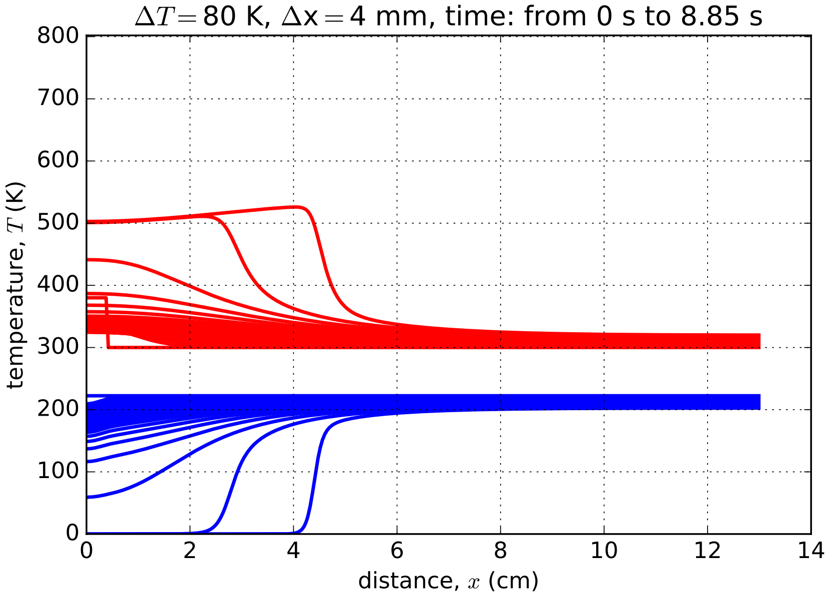

Figure 5.17: The temperature (top) and defect density (bottom) propagation fronts for a temperature increase of ΔT = 80 K, with a heating depth of Δx = 4 mm, calculated for a maximum transient time interval of 8.85 s.

5.5 Impact of the Initial Values of the Temperature and Defect Density on the Shape of the Annealing Zone

In this section we investigate the change in the shape of the annealing zone and the behaviour of the temperature and defect density profiles in the annealing zone when the initial defect density and initial temperature are changed.

An increase in the density of defects results in the decrease in the distance between them. Therefore, the width of the travelling wave annealing zone is expected to decrease when the defect density is increased. To confirm the validity of this hypothesis we studied the change in the width of the travelling wave annealing zone when the initial density of defects is increased from $n_0 = 6.63 \times 10^{26}$ defects/m^3 to $2n_0$ and then to $3n_0$. Temperature and defect density profiles calculated for these cases are presented in Figure 5.18. As can be seen in the figure, the width of the travelling wave annealing zone decreases when the density of defects is changed to magnitudes n_0, $2n_0$ and $3n_0$ as indicated by dashed lines bottom to top in Figure 5.18 (the values of the defect density, as previously, are expressed in units of temperature according to $\theta n_0/c$).

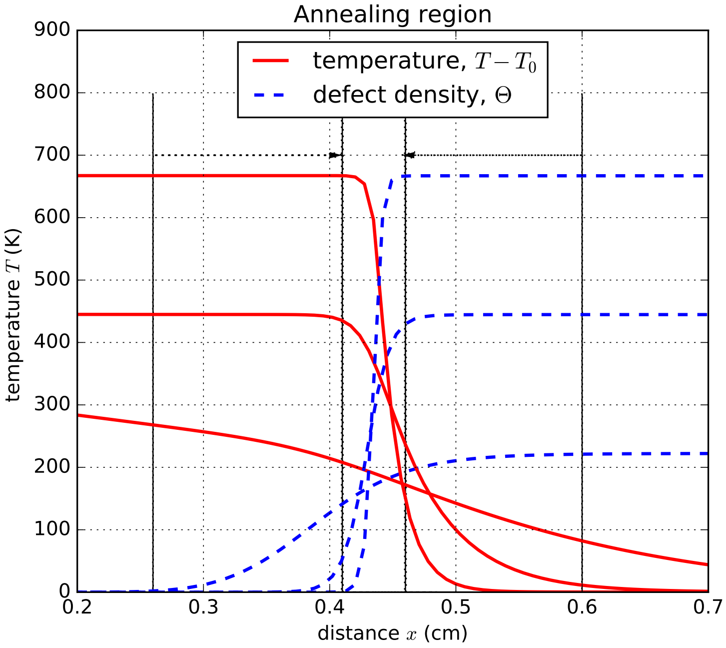

Figure 5.18: Results of our calculations showing that the annealing zone decreases in width when the initial defect density is increased.

We can recall from Section 2.10.1 that the final temperature of the sample with defects after the termination of the annealing process, denoted by T_f, is determined in the homogeneous case by the energy conservation condition:

$$T_\mathrm{f} = T_0 + \Theta_0, \tag{5.4}$$

where $\Theta_0 = \theta n_0/c$, is the *maximum thermal contribution* of annealed defects, which is the maximum temperature increase that results from a thermal energy density of θn_0 released into the sample of volumetric heat capacity c in the annealing process and thereby raising the sample temperature by an amount $\theta n_0/c$. In the case of heterogeneous annealing, the temperature in the annealing zone may under certain conditions temporarily exceed T_f.

Our calculations have shown that for sufficiently low temperatures of the sample (such that spontaneous homogeneous annealing is negligible) and for sufficiently high density of defects (such that the self-sustaining travelling wave of annealing can be initiated), the temperature front starts to propagate in a complex way such that the temperature change from the initial temperature $T - T_0$ is greater than the maximum thermal contribution Θ_0 near the travelling wave front in the annealing zone, i.e. $T - T_0 > \Theta_0$ in the annealing zone as shown in Figure 5.19, calculated for the initial temperature of $T_0 = 120\,\mathrm{K}$ and with maximum thermal contribution $\Theta_0 = 555.96\,\mathrm{K}$.

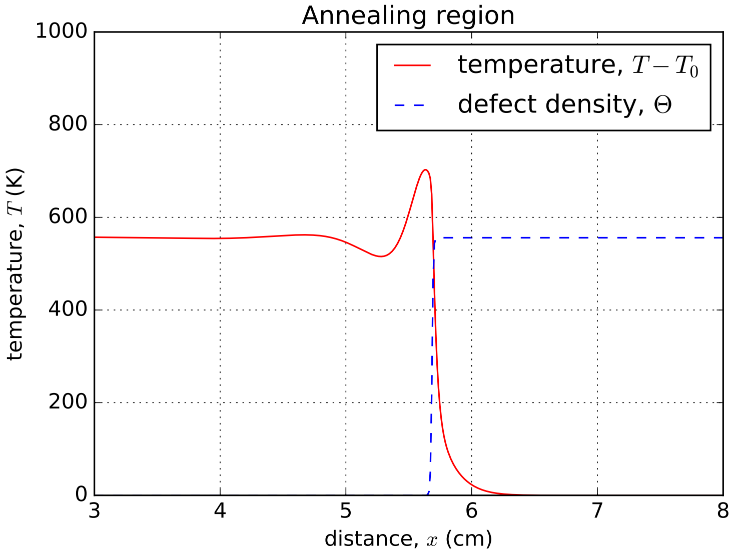

Figure 5.19: The temperature and defect density profiles in the annealing zone between the unannealed and annealed regions of the sample, calculated for $T_0 = 120\,\mathrm{K}$ and $\Theta_0 = 555.96\,\mathrm{K}$.

When the initial sample temperature is increased from $T_0 = 120\,\mathrm{K}$ to $T_0 = 300\,\mathrm{K}$ the final temperature change from the initial value becomes equal to the maximum thermal contribution from annealed defects in the annealing zone, i.e. $T - T_0 = \Theta_0$ as shown in Figure 5.20. The initiation temperature and heating depth for the profiles produced in Figures 5.19 and 5.20 are $\Delta T = 500\,\mathrm{K}$ and $\Delta x = 4\,\mathrm{mm}$, respectively.

Multiple temperature and defect density profiles for the case presented earlier in Figure 5.19, in which the initial temperature is $T_0 = 120\,\mathrm{K}$ and the maximum thermal contribution from annealed defects is $\Theta_0 = 555.96\,\mathrm{K}$, are shown in Figure 5.21 for a time interval from 0 s to 1.5 s. The temperature profiles in Figure 5.21 oscillate in a complex manner in the annealing zone.

When the initial temperature is increased to $T_0 = 300\,\mathrm{K}$ the temperature profiles no longer oscillate and the temperature gradient in the annealing zone becomes more steep compared to the oscillating temperature case, as shown in Figure 5.22. The same tendency is revealed by comparing Figure 5.19 and Figure 5.20.

Figures 5.21 and 5.22 represent temperature and defect density profiles at equal time intervals, therefore since the profiles in Figure 5.22 have larger spacing between successive profiles compared to the profiles in Figure 5.21 then the speed of the travelling wave in Figure 5.22 is greater than the speed of the travelling wave where the temperature profiles oscillate in the annealing zone in Figure 5.21. The increase in the speed of the travelling wave when T_0 is increased is an indication of the dependence of the annealing rate on temperature.

An increase of the initial temperature of the sample from $T_0 = 120\,\mathrm{K}$ to $T_0 = 166.67\,\mathrm{K}$ and a decrease in the initial defect density, such that the maximum thermal contribution from annealed

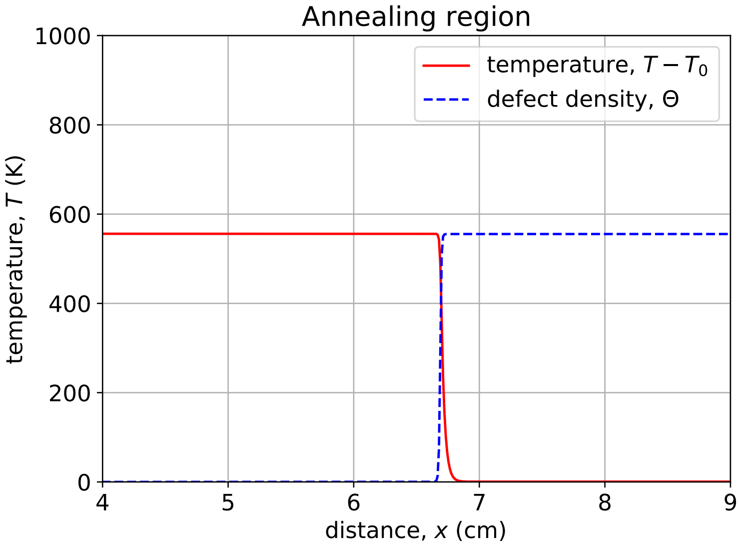

Figure 5.20: The temperature and defect density profiles in the annealing zone between the unannealed and annealed regions of the sample for T_0 = 300 K and Θ_0 = 555.96 K

.

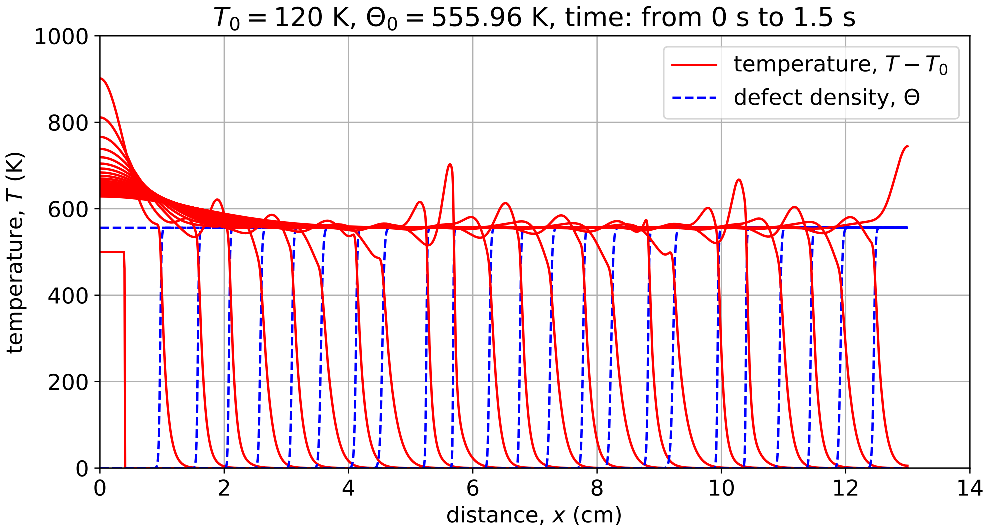

Figure 5.21: Temperature and defect density profiles when the temperature propagation front is oscillating and the initial sample temperature is 120 K.

defects reduces from Θ_0 = 555.96 K to Θ_0 = 333.58 K, leads to a more complex change of the temperature profiles, shown in Figure 5.23.

The corresponding defect density profiles in Figure 5.23 are shown to have irregular spacing in similar regions as the temperature profiles. Although the spacing of the defect density and temperature profiles is irregular, the time intervals between successive profiles are equal; this is an indication of different speeds of the propagation front for the defect density and temperature in different regions in the sample. In the regions where the defect density profiles are clustered the propagation front propagates at a slower speed than in the regions where the profiles have larger spacing. The defect density and temperature fronts propagate faster in regions where the temperature increases rapidly above the value of T_f, and they propagate slower in regions where the

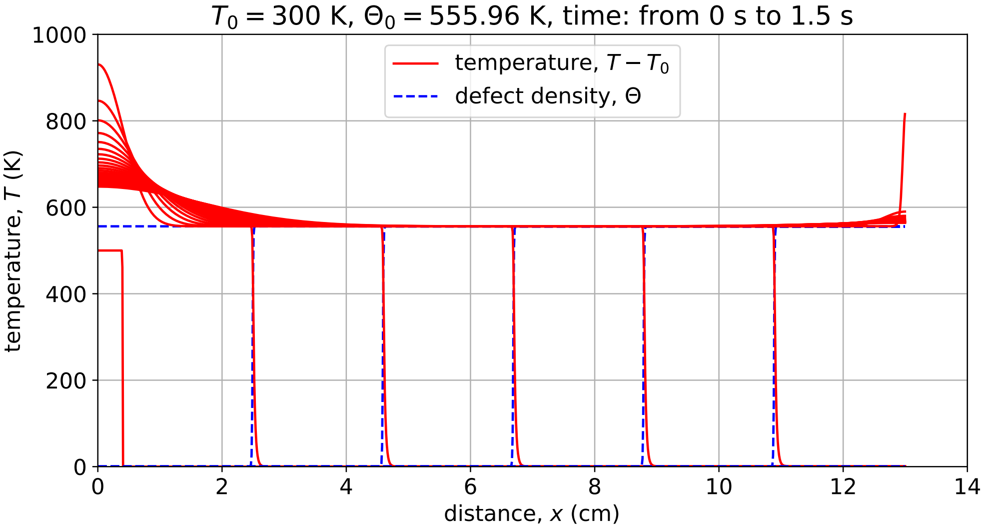

Figure 5.22: Temperature and defect density profiles for front for the non-oscillating temperature propagation front and for the initial sample temperature of 300 K.

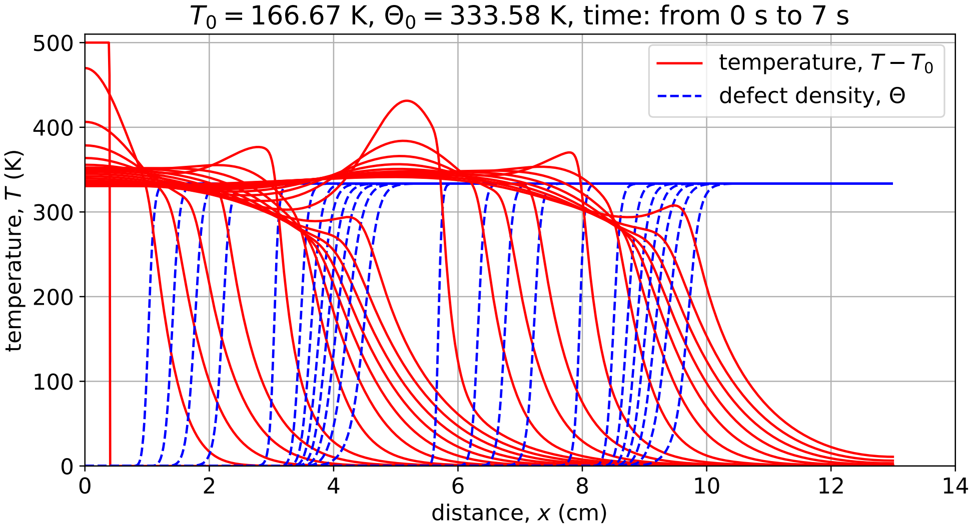

Figure 5.23: The temperature propagation front changes in a complex manner when the initial temperature is $T_0 = 166.67$ K and the maximum temperature increase from annealed defects is $\Theta_0 = 333.58$ K.

temperature decreases below T_f, as can be clearly seen in Figure 5.23. The initiation temperature and heating depth for profiles produced in Figure 5.23 are $\Delta T = 500$ K and $\Delta x = 4$ mm, respectively.

5.6 Annealing Time and Travelling Wave Velocity

In this work, we define the *annealing time* as the time at which less that 1 % of the initial total number of defects remains in the entire sample as a result of annealing process. We show that in the travelling wave regime, and for a fixed final temperature increase T_f, the annealing time of defects practically becomes a linear function of the heating depth. Lastly, in Section 5.6.3 we determine the velocity of the annealing front from the rate of annealing of the fraction of remaining defects and compare it to the velocity calculated from the linear relation of the annealing time to the heating depth.

5.6.1 Annealing time in the case of the homogeneous process

In the literature review, Section 2.10.1, we discussed the case of spontaneous and homogeneous annealing and gave the analytic implicit dependence of the defect density on time. We re-introduce the analytic formula, without the k index for indicating the defect type, for simplicity, as follows:

$$\frac{t}{\tau_0} = \mathrm{Ei}\left(\frac{T_\mathrm{a}}{T_\mathrm{f}-\Theta}\right) - \mathrm{Ei}\left(\frac{T_\mathrm{a}}{T_0}\right) + \exp\left(\frac{T_\mathrm{a}}{T_\mathrm{f}}\right)\left[\mathrm{Ei}\left(\frac{T_\mathrm{a}}{T_0}-\frac{T_\mathrm{a}}{T_\mathrm{f}}\right) - \mathrm{Ei}\left(\frac{T_\mathrm{a}}{T_\mathrm{f}-\Theta}-\frac{T_\mathrm{a}}{T_\mathrm{f}}\right)\right], \tag{5.5}$$

where $\Theta = \theta n/c$ is the sample temperature increase at any time as a result of the energy density of amount θn that is released into the sample of volumetric heat capacity c in the process of annealing and thereby raising the temperature of the sample by an amount $\theta n/c$. For a uniform initial temperature of $T_0 = 300\,\mathrm{K}$ and for a uniform initial defect density of $n_0 = 6.63\times10^{26}$ defects/m^3 the annealing time calculated with formula (5.5) is 13.63 s.

Let us introduce the fraction of defects remaining in the sample as the the number of defects N in the sample at any moment of time, t, divided by the initial total number of defects N_0:

$$F(t) = \frac{N(t)}{N_0} = \frac{1}{Ln_0}\int_0^L n(t,x)\,\mathrm{d}x. \tag{5.6}$$

In Figure 5.24, we present the calculation results for the time evolution of the fraction of remaining defects, $F(t)$, in the sample during homogeneous (and spontaneous) annealing for different values of the initial temperature, T_0. As one can see in Figure 5.24, for initial temperatures that are lower than the reference value of 300 K, the annealing time is larger than 13.63 s and lower than 13.63 s for initial temperatures that are greater than the reference value. For each curve corresponding to a different initial temperature T_0 in Figure 5.24, two stages of annealing can be distinguished: the first is "slow" one and the second is "fast" one. The slow stage lasts for the majority of the total transient time and the fast stage lasts for a relatively negligible part of the total transient time. For the calculated initial temperatures lower or equal to 300 K, i.e. $T_0 \le 300\,\mathrm{K}$, the transient time of the slow stage is greater than 13 s and the transient time for the fast stage ranges from close to zero to a few seconds, see Figure 5.24 for details. A similar proportionality of the fast and slow stage is true even for initial temperatures above 300 K Figure 5.24. Therefore, the annealing time for spontaneous homogeneous annealing, for the most part, depends on the slow stage, which depends on T_0. The fast stage is practically independent of T_0. For all studied values of parameters, the transition from the "slow" to the "fast" stage occurs when the fraction of remaining defects decreases to approximately 0.8 in the process of annealing, as one can observe in Figure 5.24.

The annealing time for spontaneous homogeneous annealing also changes when the initial density of defects in changed according, to (5.5). When the initial density of defects is increased for a sample of a constant volume, the total number of defects, N_0, is increased.

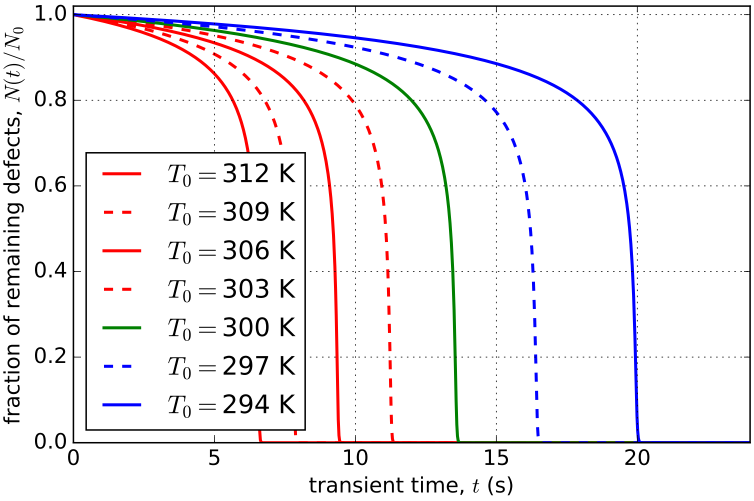

Figure 5.24: The time evolution of the fraction of remaining defects for some initial temperatures below and above the reference value of initial temperature of 300 K.

The dependence of the fraction of remaining defects on time when the total number of defects is increased is shown in Figure 5.25. Comparing 5.24 and Figure 5.25 we observe that in Figure 5.25 the value of the faction of remaining defects, at which the transition from the "slow" stage to the "fast" stage of annealing, changes when the initial density of defects is increased. When the initial density of defects is increased, the transition occurs at higher fraction of remaining defects,and changes from approximately 0.8 to close to 1 (see Figure 5.25).

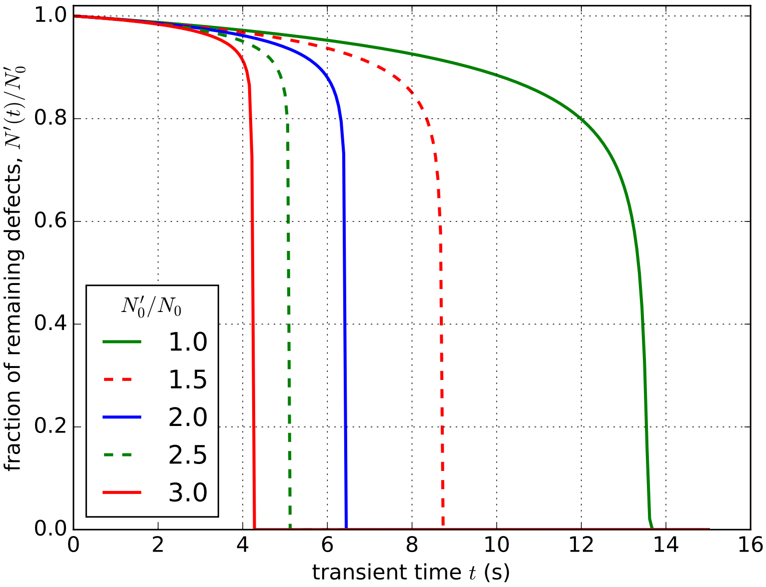

Figure 5.25: The time evolution of the fraction of remaining defects for different initial homogeneous defect density distributions. Here N' denotes the number of defects in the sample at any time for different initial defect densities, N'_0, and N_0 is the reference initial number of defects.

A comparison of Figure 5.24 and Figure 5.25 reveals a more sensitive dependence of the annealing time on temperature than on the initial defect density. For example, when the initial temperature of the sample with the reference initial defect density $n_0 = 6.63 \times 10^{26}$ defects/m^3 is increased from 300 K to 312 K (a factor increase of 1.04) the annealing time decreases from 13.63 s to a value close to 6 s, see Figure 5.24. Then again, when the density of defects in the sample with initial defect density $n_0 = 6.63 \times 10^{26}$ defects/m^3, and initial temperature $T_0 = 300$ K, is increased by a factor of 2, the annealing time decreases from 13.63 s to a value close to 6 s, see Figure 5.25.

Overall, the defect annealing time in the case of homogeneous annealing depends on temperature and the variables that affect the temperature of the sample in the process of annealing. For example, when the initial defect density is increased, the contribution from annealed defects to the temperature of the sample is $\theta n_0/c$ or Θ_0. Therefore a change of any of the parameters θ, n_0 and c can lead to a change in the annealing time of defects. In Section 5.7 we discuss the annealing time as a function of n_0.

5.6.2 Annealing time in the case of the heterogeneous process

In this section we study the annealing time in the case of the heterogeneous annealing of defects. We show that in the travelling wave regime the annealing time of the heterogeneous annealing of defects is a linear function of only one of the initiating parameters for heterogeneous annealing, namely the heating depth Δx.

We recall that in our study the initiating energy for heterogeneous annealing depends on the temperature increase, ΔT, and the heating depth, Δx, as defined by (5.1). This means that the triggering of the travelling wave depends on the combination of the initiating parameters ΔT and Δx. For instance, the initiating energy of 1444.24 kJ/m^2 corresponding to the initiating parameters: the heating depth of $\Delta x = 2$ mm and temperature increase of $\Delta T = 280$ K in the sample with initial temperature $T_0 = 300$ K and initial density of defects of $n_0 = 6.63 \times 10^{26}$ defects/m^3, was shown to be sufficient to trigger the travelling wave in Figure 5.10 of Section 5.3.

We extended this study for the same initial conditions, viz. $n_0 = 6.63 \times 10^{26}$ defects/m^3 and $T_0 = 300$ K, by considering various combinations of the initiating parameters Δx and ΔT and investigated the dependence of the annealing time on these initiating parameter combinations. We carried out the selection of the initiating parameters combinations in the following order. First we chose an initiating temperature increase of $\Delta T = 40$ K and then we select it with different heating depth values from $\Delta x = 0$ mm (for the sake of comparison with the case of homogeneous annealing) to $\Delta x = 14$ mm with a difference (step) between them of 1 mm. We followed the same procedure for initiating temperature values: $\Delta T = 80$ K, $\Delta T = 120$ K, $\Delta T = 160$ K, $\Delta T = 200$ K, $\Delta T = 240$ K and $\Delta T = 280$ K. The results of calculations of the dependence of the annealing time on these combinations of the initiating parameters are presented in Figure 5.26.

In this figure we see, that for heating depths closer to zero, the dependence of the annealing time, t^{a}, on the heating depth, Δx, is non-linear for all values of ΔT and the annealing time approaches the annealing time of spontaneous annealing of 13.63 s. For all values of ΔT the dependence of the t^{a} on the initiating parameters approaches linear one as Δx is increased, as can be seen in Figure 5.26. For initiating temperature increases of $\Delta T = 120$ K, $\Delta T = 160$ K, $\Delta T = 200$ K, $\Delta T = 240$ K and $\Delta T = 280$ K the linear dependence becomes more prominent at heating depths equal to or greater than 4 mm, i.e. $\Delta x \geq 4$ mm, as shown in Figure 5.27 which is a zoom-in of Figure 5.26 in the region from 4 mm to 14 mm. For an initiating temperature of $\Delta T = 280$ K the annealing time appears to have a linear dependence on the heating depth in the region where $\Delta x \geq 4$ mm as can be clearly seen in Figure 5.27.

As mentioned earlier, we already presented the temperature and defect density profiles for the initiating temperature increase $\Delta T = 280$ K at a heating depth of $\Delta x = 2$ mm in Figure 5.10 of

Section 5.3 and we observed that at this heating depth the travelling wave is triggered. More certainly at heating depths greater than $\Delta x = 2\,\mathrm{mm}$ for the same initiating temperature of $\Delta T = 280\,\mathrm{K}$ the travelling wave regime will be triggered since the initiating energy will be greater for $\Delta x > 2\,\mathrm{mm}$. Based on this observation we claim that the regime where the annealing time, t^{a}, has a linear dependence on Δx is the regime where the travelling wave regime of annealing is dominant.

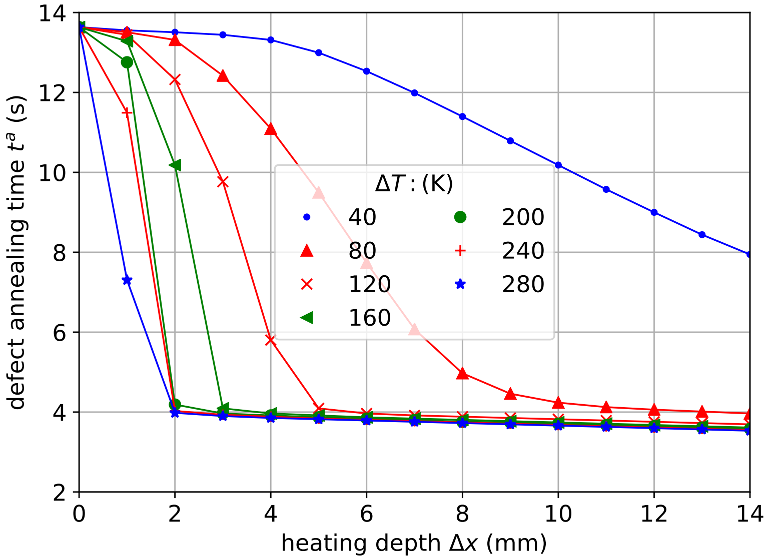

Figure 5.26: The annealing time dependence on the heating depth Δx for different initiation temperatures and for a sample of length $L = 13\,\mathrm{cm}$.

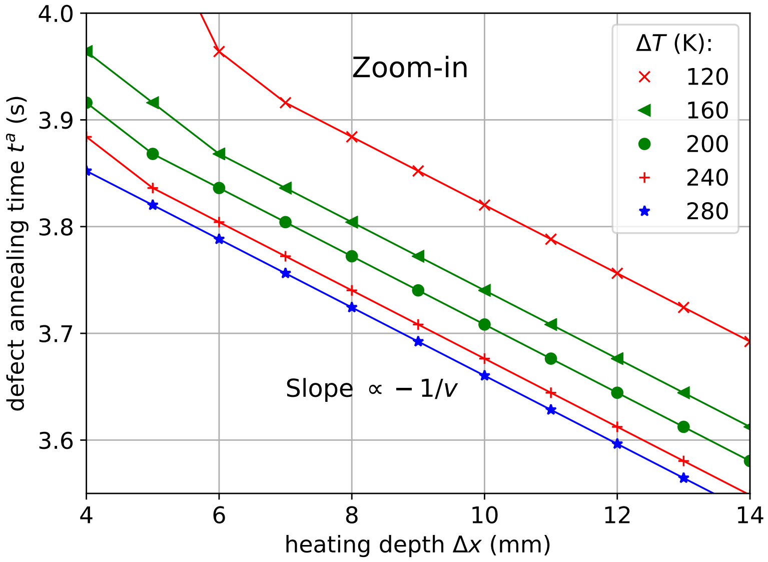

Figure 5.27: A zoom-in of Figure 5.26 at heating depths between 4 mm and 14 mm.

In Figure 5.2 of Section 5.1 we showed and discussed the influence of the initiation (left) boundary and the right boundary on the travelling wave. For the initiation boundary we discussed, in Section 5.2, the temperature and defect density profiles in the early moments of the transient for different distributions of the initiating temperature. We showed that the time at which the self-sustained self-propagating heterogeneous annealing process and therefore the travelling wave can develop depends on the initiating temperature distribution. For the right boundary, in Figure 5.2 of Section 5.1, we showed that the defects anneal rapidly at the right boundary because of the temperature increase near the boundary as a result of the boundary being thermally isolated and the generated heat "can not escape", hence the annealing rate in the vicinity of the boundary is higher due to the thermal-concentration feedback. Furthermore, in Section 5.6.3, we will show that if the interior region of the sample far from the boundaries is sufficiently long to render the influence of the boundaries to be negligible, then the time of annealing of defects at the boundaries has a negligible contribution to the total annealing transient time of heterogeneous annealing.

5.6.3 Velocity of the travelling wave

In this section we present a formula for determining the velocity of the travelling wave from the rate of defect annealing. We also compare the results of the velocity, calculated from the slope of the linear dependence of the annealing time on the heating depth in Figure 5.27, to the velocity calculated from the annealing rate.

In Section 5.6.2 we concluded that the travelling wave is initiated for initiating parameters $\Delta T = 280\,\mathrm{K}$ and $\Delta x = 2\,\mathrm{mm}$ in a sample with initial temperature $T_0 = 300\,\mathrm{K}$ and initial defect density $n_0 = 6.63 \times 10^{26}\,\mathrm{defects/m^3}$. We show in Figure 5.28 a schematic of the temperature and defect density profiles for these initiating parameters in a sample of length $L = 13\,\mathrm{cm}$ and indicate the time of the transient for the profiles in the travelling wave regime.

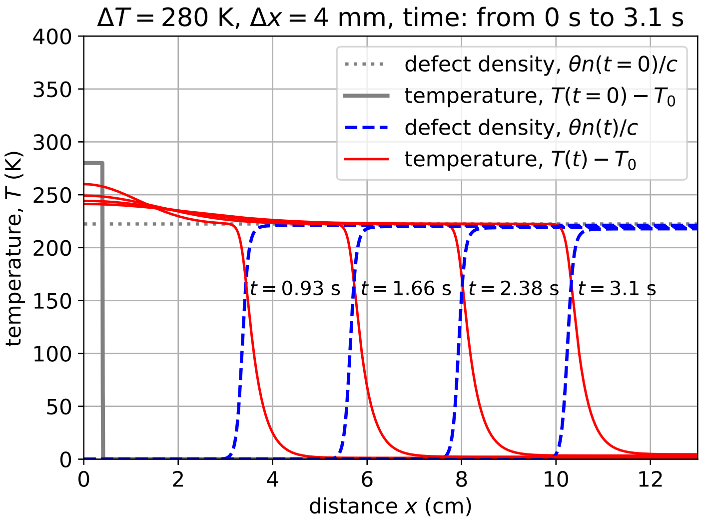

Figure 5.28: Schematic of annealing wave fronts, propagating from the annealed material to the damaged material in the travelling wave regime.

The corresponding time evolution of the fraction of defects remaining in the sample in the process of annealing, as determined by (5.6), is shown in Figure 5.29 (left). In the schematic of the temperature and defect density profiles in Figure 5.28 the fraction of remaining defects in time is the proportion of the un-annealed region ahead of the density propagation front in time to the initial defect density. From Figure 5.29 (right) we can see that the defects anneal at a constant rate in the travelling wave regime. In this figure we can also see that the transient time of the travelling wave dominates the total transient of the annealing process and therefore the annealing time in the travelling wave regime is approximately equal to the total transient time of the annealing process.

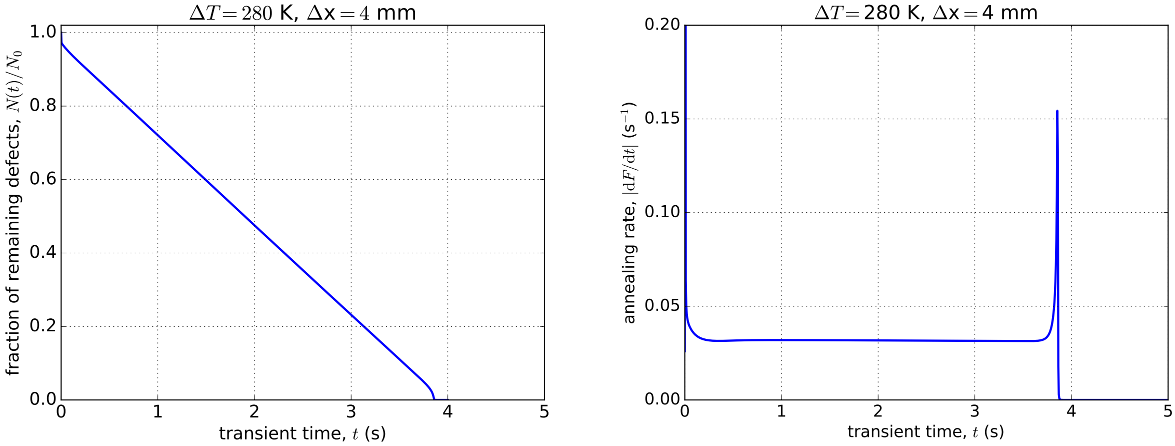

Figure 5.29: The time evolution of the fraction of remaining defects (left) and the corresponding obsolute time change of the fraction of remaining defects (right) with initiation temperature ΔT = 280 K and heating depth Δx = 4 mm for a sample of length L = 13 cm.

If we assume that the annealing of defects occurs in the travelling wave regime then the velocity of the travelling wave front, v, can be calculated from the annealing rate as follows:

$$v = -\frac{\mathrm{d}}{\mathrm{d}t}\int_0^L \frac{n(t,x)}{n_0}\,\mathrm{d}x \approx -L\frac{\Delta F}{\Delta t}, \tag{5.7}$$

and it is constant in this regime.

For initiation temperatures lower than ΔT = 280 K at a heating depth of Δx = 4 mm the contribution of the travelling wave regime to the total annealing time is less dominant as one may observe in Figure 5.30 (travelling wave regime corresponds to straight parallel sections of curves in the figure). Figure 5.30 also shows, for comparison, the time evolution of the fraction of remaining defects for the spontaneous annealing (i.e. when ΔT = 0 K). With the use of (5.7), we calculated the travelling wave velocity of v = 3.18 cm/s.

If the travelling wave regime is initiated in the early moments of the transient for a minimum heating depth of $\Delta x = \Delta x_{\mathrm{min}}$ and the defect annealing rate is constant for the most part of the annealing process, as in Figures 5.29 and 5.31, then the wave velocity can be approximated by dividing the length traveresed by the wave, $L - \Delta x$, by the annealing time as follows:

$$v \approx \frac{L - \Delta x}{t^{\mathrm{a}}}, \tag{5.8}$$

where $\Delta x \geq \Delta x_{\mathrm{min}}$. For the selected heating depth values for the calculations in Figure 5.31, Δx_{min} = 4 mm and ΔT = 200 K. At heating depths values Δx = 4 mm, Δx = 16 mm, Δx = 32 mm, Δx = 48 mm and Δx = 64 mm the annealling times are t^{a} = 3.90 s, t^{a} = 3.49 s, t^{a} = 3.00 s, t^{a} = 2.49 s and t^{a} = 2.00 s, respectively. Substituting these values in (5.8) we obtained an average velocity value v = 3.27 cm/s.

Alternatively, using Figure 5.27, we can also calculate the travelling wave velocity by considering the annealing time corresponding to any consecutive heating depths. In the travelling wave regime we found that the slope of the linear dependence of the annealing time on the heating depth

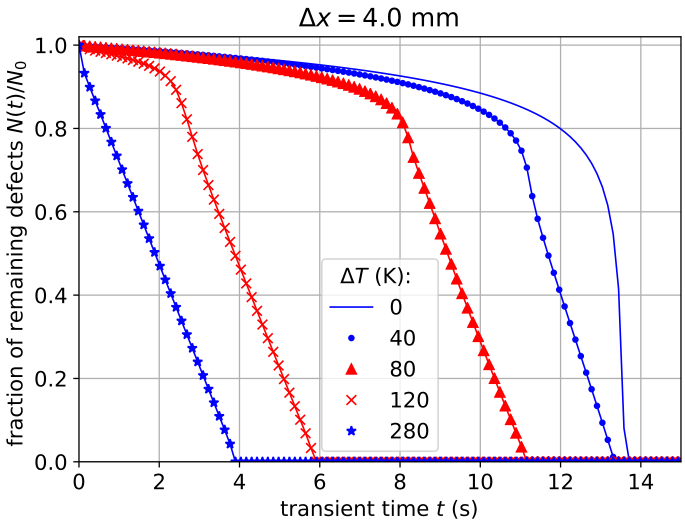

Figure 5.30: The time evolution of the fraction of remaining defects for different initiating temperatures at a heating depth $\Delta x = 4\,\mathrm{mm}$ in a sample of length $L = 13\,\mathrm{cm}$

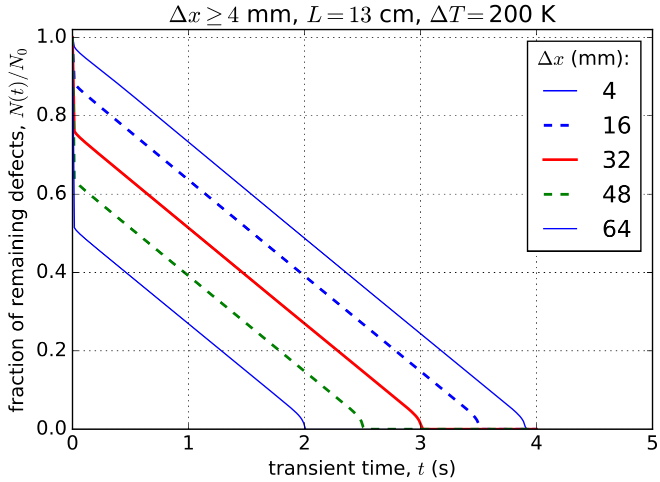

Figure 5.31: The time evolution of the fraction of remaining defects in a sample of length $L = 13\,\mathrm{cm}$ when the heating depth is increased in the travelling wave regime . The initiating temperature for the experiment is $\Delta T = 200\,\mathrm{K}$.

is proportional to the inverse of v (which is constant) i.e.

$$\text{slope} = \frac{t_2^{\mathrm{a}} - t_1^{\mathrm{a}}}{\Delta x_2 - \Delta x_1} \approx -\frac{1}{v}, \quad \text{and so} \quad v \approx -\frac{\Delta x_2 - \Delta x_1}{t_2^{\mathrm{a}} - t_1^{\mathrm{a}}}, \tag{5.9}$$

where Δx_1 and Δx_2 are any two heating depths such that $\Delta x_2 > \Delta x_1$ and t_1^{a} and t_2^{a} are the corresponding annealing times at the respective heating depths. For $\Delta x_1 = 4\,\mathrm{mm}$ and $\Delta x_2 = 14\,\mathrm{mm}$ the annealing times are $t_1^{\mathrm{a}} = 3.85\,\mathrm{s}$ and $t_2^{\mathrm{a}} = 3.28\,\mathrm{s}$, respectively, for an initiation temperature of $\Delta T = 280\,\mathrm{K}$. For this configuration, we calculated $v = 3.12\,\mathrm{cm/s}$.

The velocity calculated with formula (5.7) takes the average of all the numerically calculated data points where the annealing rate of defects $\Delta F/\Delta t$ is approximately constant as shown in Figure 5.29 (right). The velocity calculated with formula (5.7) considers far more data points than that calculated with formulae (5.8) and (5.9).

5.7 Dependence of Annealing Time on the Initial Defect Density

In this section we study how the annealing time, t^{a}, changes when the initial density of defects is modified (more specifically increased) from a reference initial density of $n_0 = 6.63 \times 10^{26}$ defects/m^3.

In the case of the spontaneous annealing of defects, when the initial density of defects is modified, t^{a} varies according to the analytic formula for the dependence of the defect density on time given by equation (5.5). The increase in the initial defect density, n_0, results in an increase in final temperature of the sample, T_{f}, which has the following dependence on n_0:

$$T_{\mathrm{f}} = T_0 + \Theta_0 = T_0 + \frac{\theta}{c} n_0, \tag{5.10}$$

as previously stated in (5.4). For a constant initial temperature T_0 and constant energy released per annealing of one defect θ and for a constant volumetric heat capacity c, this dependence of T_{f} on n_0 is linear as can be seen in (5.10).

Now, in our numerical calculations, t^{a} for the homogeneous spontaneous annealing was determined at the time when the defects anneal to 1 % of the initial defect density, i.e. t^{a} is defined such that $n(t^{\mathrm{a}}) = 0.01 n_0$. The numerically calculated annealing time was found to agree with the value determined by substituting $\Theta = 0.01\Theta_0$ (that corresponds to $n = 0.01 n_0$) to the analytic formula (5.5).

The results for our numerical calculations for the spontaneous annealing time when the initial defect density is increased are shown in Figure 5.32 for the curve corresponding to $\Delta T = 0$ K. It is the case of spontaneous homogeneous annealing. When annealing is initiated and develops heterogeneously, the dependence of t^{a} on n_0 becomes steeper, and the annealing time is decreased further, as illustrated by our results in Figure 5.32 with the curves corresponding to $\Delta T = 40$ K, $\Delta T = 80$ K, $\Delta T = 120$ K and $\Delta T = 160$ K, all calculated at heating depths of $\Delta x = 4$ mm.

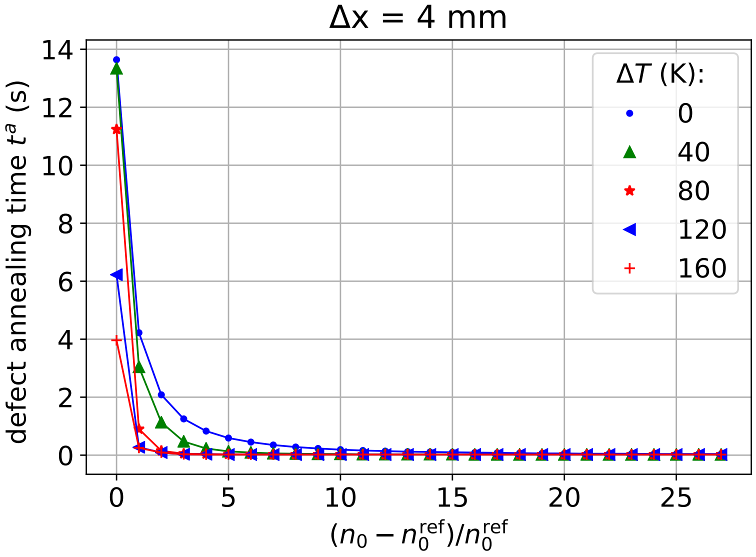

Figure 5.32: The defect annealing times for different initial defect densities. The reference value is $n_0^{\mathrm{ref}} = 6.63 \times 10^{26}$ defects/m^3.

The steep decrease in the annealing time as the initial density of defects is increased is as a result of a larger positive feedback from from the annealing of defects which, results in a larger maximum temperature increase. This positive feedback is enhanced further even when annealing is initiated heterogeneously by heating the sample in a localised region near the surface (since some amount of additional energy is added to the system).

For the spontaneous annealing case, where the defects anneal homogeneously, the annealing time does not depend on the length of the sample. For the heterogeneous annealing case, however, the annealing time also depends on the length of the sample (in addition to the dependence on n_0 shown in Figure 5.32). Therefore, although the shape of the curve corresponding to the spontaneous annealing case (i.e. the case $\Delta T = 0\,\mathrm{K}$ in Figure 5.32) will not change when the calculation of results presented in Figure 5.32 are repeated for different lengths of the sample, the shape of the curves corresponding to the heterogeneous annealing cases (i.e. in general for the cases $\Delta T > 0$ and $\Delta x > 0$) will depend on the length of the sample. The results presented in Figure 5.32 were produces for a sample length of $L = 13\,\mathrm{cm}$.

If in the process of heterogeneous annealing the travelling wave is initiated then the annealing time is reduced even further, since the heterogeneous annealing of defects in our calculations is fastest in the travelling wave regime. However, the annealing time in the travelling wave regime depends on the velocity of the travelling wave and the length of the sample traversed by the wave. Furthermore, if the length of the sample is long enough such that the annealing time in the travelling wave regime is sufficiently greater than the annealing time for spontaneous annealing, then if the calculations for results in Figure 5.32 are repeated, the shape of the curves for heterogeneous annealing cases would not deviated from the curve for the spontaneous annealing case.

The decrease in the annealing time when initial defect density is increased means that the annealing rate increases as well. In the travelling wave regime, therefore, the velocity of the travelling wave increases for higher initial defect densities, according to the formula for determining the velocity of the wave from the annealing rate (5.7). To investigate this, we calculated the time evolution of the fraction of remaining defects in the travelling wave regime when the initial density of defects is doubled from the reference value $n_0 = 6.63 \times 10^{26}\,\mathrm{defects/m^3}$. Calculations for n_0 and $2n_0$ were performed with initiating parameter values $\Delta T = 280\,\mathrm{K}$ and $\Delta x = 4\,\mathrm{mm}$ and in a sample of length $L = 13\,\mathrm{cm}$. The results for the calculation are presented in Figure 5.33 and from the slopes of the two lines in the figure we can see that the annealing rate increases when the initial density of defects is doubled. Using (5.7) we determined a velocity of $v = 54.07\,\mathrm{cm/s}$ for an initial defect density of $2n_0$, which is a factor of about 17 more than the velocity calculated for the reference initial defect density.

In Section 5.6.1 we showed that the annealing rate is more sensitive to the change in temperature than to the change in the density of defects. The results of this section have shown this sensitivity of the annealing rate when the temperature is increased in a localised region near the sample surface and when the density of defects is increased.

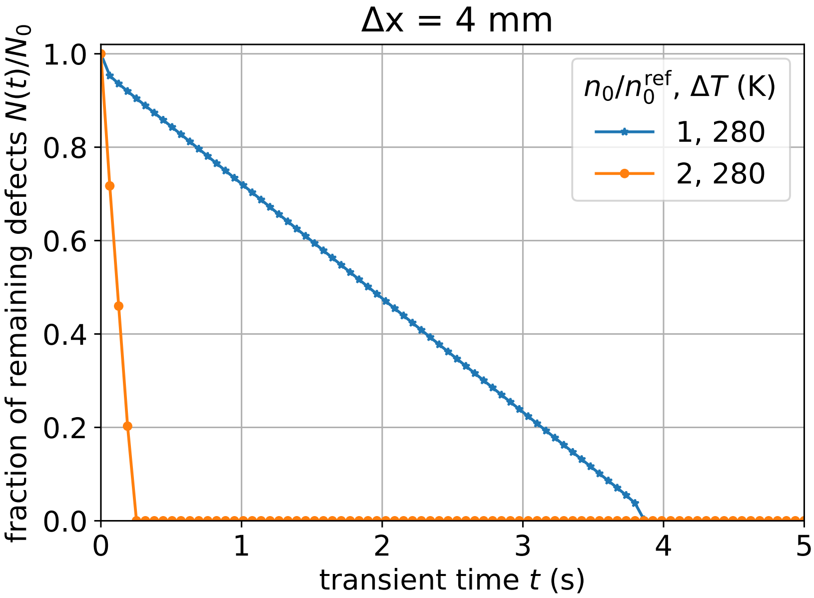

Figure 5.33: The evolution of the fraction of remaining defects in time for two different initial defect densities, n_0^{ref} and $2n_0^{\mathrm{ref}}$, with $n_0^{\mathrm{ref}} = 6.63 \times 10^{26}$ defects/m^3.

5.8 Influence of the Boundaries on the Travelling Wave

In this section we investigate, in detail, the effect of the boundary on the temperature and defect density propagation fronts and on the time evolution of the fraction of remaining defects. We have already discussed the annealing process near the initiation (or left) boundary in Section 5.2 and in this section we extend the heating depth region to $\Delta x = 40\,\text{mm}$ for a detailed analysis of the annealing process in the initiation region.

We have produced results for the travelling wave for the initiation temperature increase $\Delta T = 200\,\text{K}$ and for the heating depth $\Delta x = 40\,\text{mm}$, presented in Figure 5.34. In the figure, three regions corresponding to the three regimes of self-sustained annealing, can be distinguished, namely: the initiation region; the travelling wave regime region (away from the boundaries); and the near the right boundary. As it is clearly seen in Figure 5.34, for the aforementioned initiating parameters, the travelling wave is formed shortly after initiation.

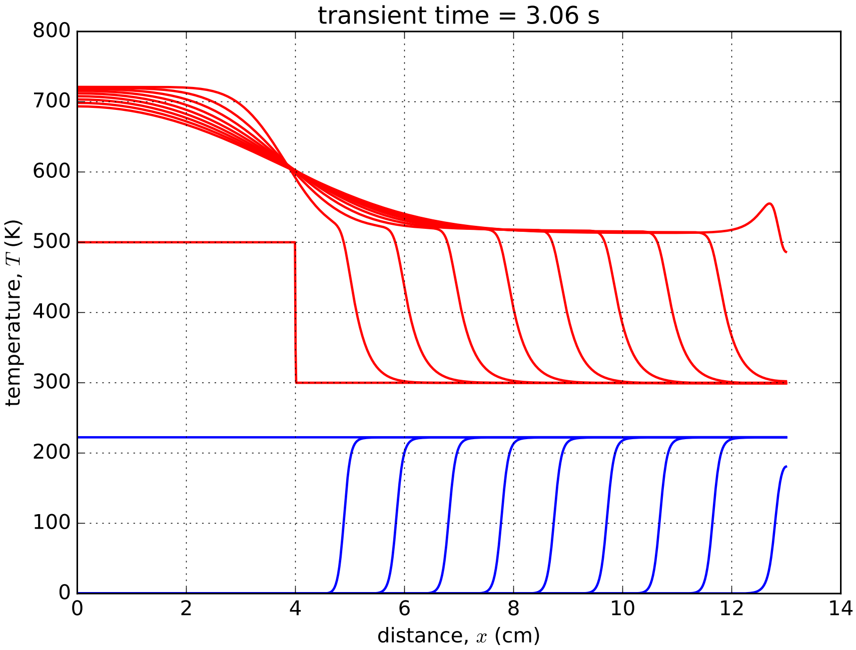

Figure 5.34: The temperature (top) and defects density (bottom) propagation fronts for a temperature increase of $\Delta T = 200\,\text{K}$, with a heating depth of $\Delta x = 40\,\text{mm}$ for a maximum transient time interval of 3.06 s.

The time evolution of the fraction of defects in the sample, corresponding to the profiles in Figure 5.34 is presented in Figure 5.35 (top picture). The defects in the region of x from 0 mm to 40 mm anneal almost instantaneously as can be seen in the figure. A zoom-in of Figure 5.35 (top picture) for the first 16 ms is given in Figure 5.35 (bottom picture) which shows in more detail the time evolution of the fraction of remaining defects in the beginning of the transient. As can be seen in Figure 5.35 (bottom picture) the annealing of defects in not completely instantaneous in the considered region from 0 mm to 40 mm, and the time evolution of the fraction of remaining defects resembles the case of homogeneous annealing in a closed system (adiabatic annealing). The reason for this similarity is that the system in this region resembles a half closed homogeneous annealing system. In addition, the temperature increase of $\Delta T = 200\,\text{K}$ reduces significantly the time of spontaneous annealing. As can be clearly seen in Figure 5.35 (bottom picture), approximately 30 % of defects in the entire sample are annealed in this region in first 12 ms.

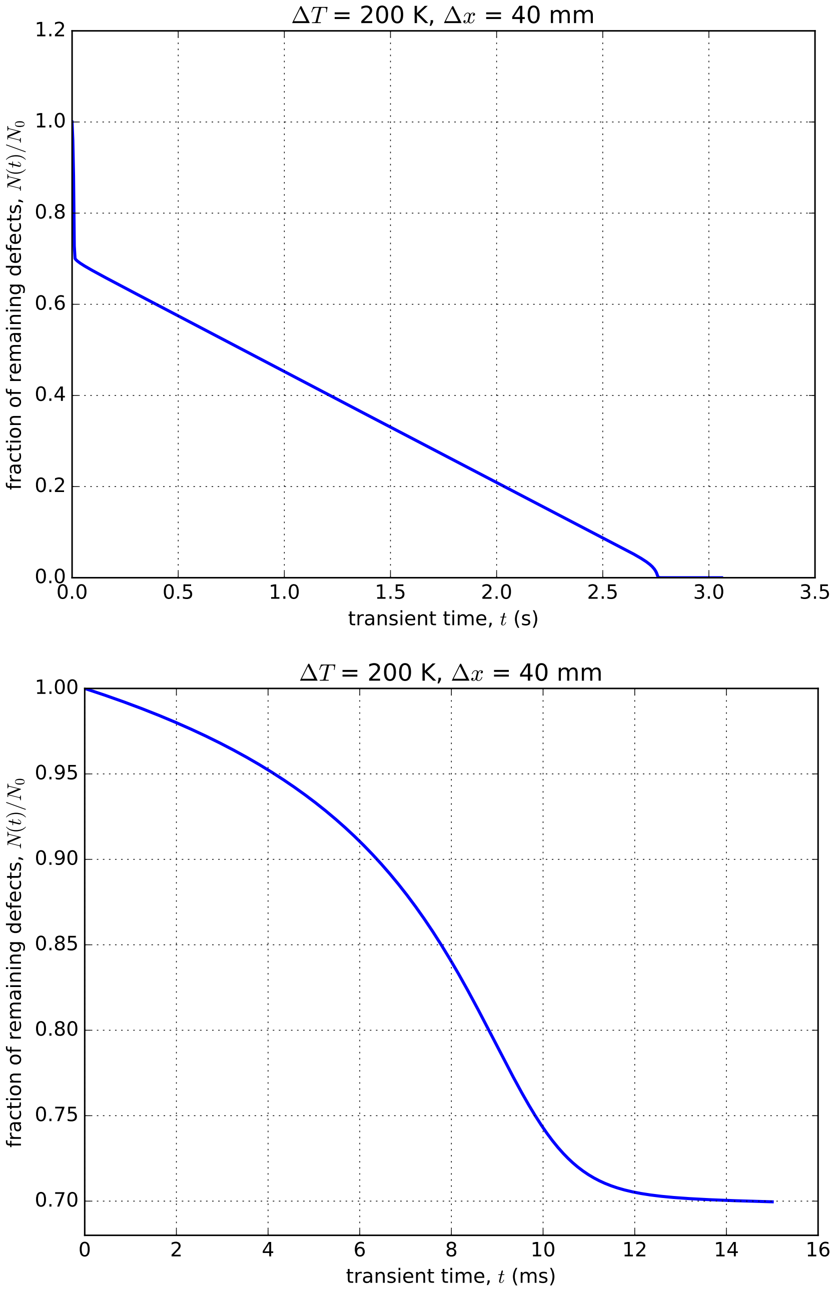

Figure 5.35: The time evolution of the fraction of remaining defects in the sample for the initiation parameters, Δx = 40 mm and ΔT = 200 K, (left) and the zoom-in of the fraction of remaining defects in the first 16 ms of the transient (right).

The temperature and defect density profiles for the first 15 ms of the transient in the spatial region from x = 4 mm to x = 40 mm are shown in Figure 5.36 and the defects are shown to anneal almost homogeneously, as can be clearly seen in this figure (bottom lines). This is indication that heat transfer effect is small as compared to spontaneous annealing in this time interval in the considered region.

At the right edge, as it was before discussed in Section 5.1, the temperature propagation fronts superimpose near the boundary when it reaches a halt and the temperature starts to increase because the heat generated in the annealing zone can not escape trough the thermally isolated boundary. This effect can be observed in Figure 5.34. The annealing rate of the remaining defects in the

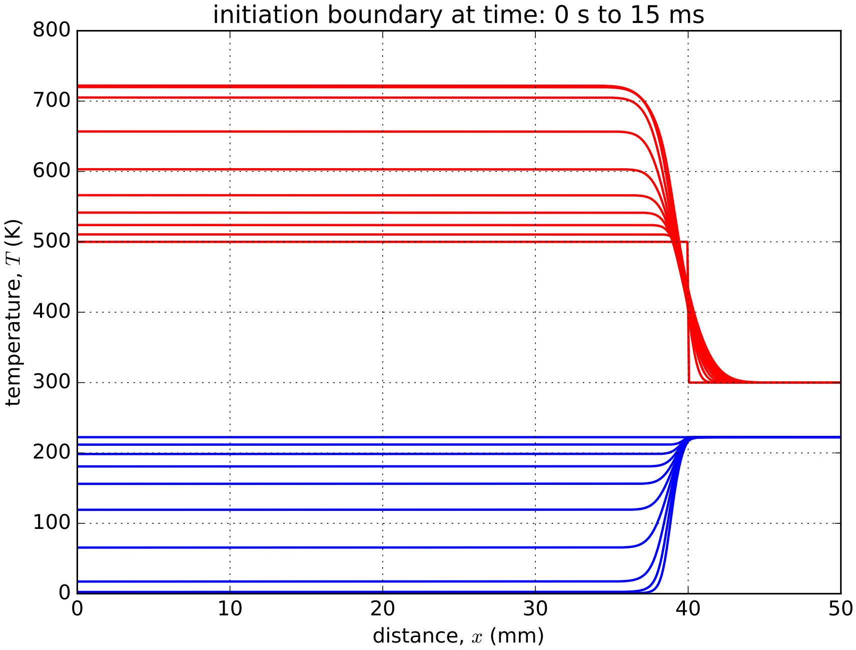

Figure 5.36: The initial moments of the transient at the initiation region for the temperature (top) and defects density (bottom) profiles for a temperature increase of $\Delta T = 200$ K, with a heating depth of $\Delta x = 40$ mm and at a maximum transient time interval of 15 ms.

region increases rapidly (because of the temperature increase) and the fraction of remaining defects at the right boundary also changes rapidly, as shown in Figure 5.37, which contains a zoom-in of the fraction of remaining defects at the right boundary of the sample in the last seconds before the annealing time is reached.

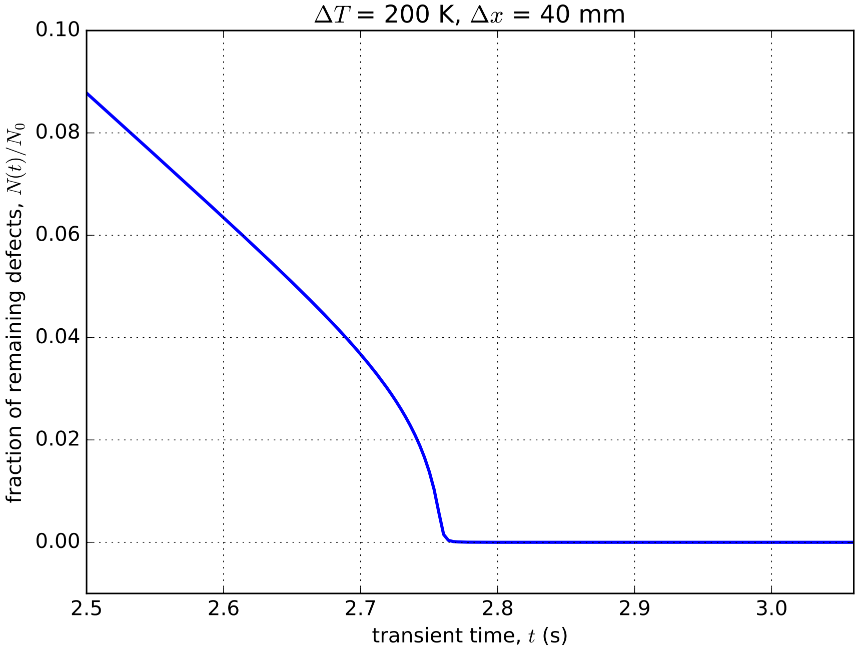

Figure 5.37: A zoom-in of the fraction of remaining defects at the right boundary of the sample in the last seconds before the annealing time is reached (right).

For lower initiation depths the influence of the left boundary on the travelling wave of annealing becomes smaller since less of the defects are annealed in the initiating region (Δx). This effect is illustrated with results of calculations for different Δx, presented in Figure 5.38. The figure displays in the top a zoom-in of the fraction of the remaining defects in the first few milliseconds of the transient (i.e. for the annealing in the vicinity to the initiation boundary) and a zoom-in of the fraction of remaining defects for the annealing at the right boundary of the sample in the last seconds before the annealing time is reached. One can observe that the fraction of defects in the sample annealed at the initiation boundary in the first 15 ms reduces from 15 % for Δx = 20 mm to less than 4 % for Δx = 4 mm.

Lastly, as can be seen by comparing Figure 5.38 (top) and Figure 5.38 (bottom), the length of the heating depth affects the annealing time in such a manner that when the heating depth is increased (decreased) the annealing time decreases (increases). This result was discussed before in Section 5.6.2 and shown in Figures 5.26 and 5.27.

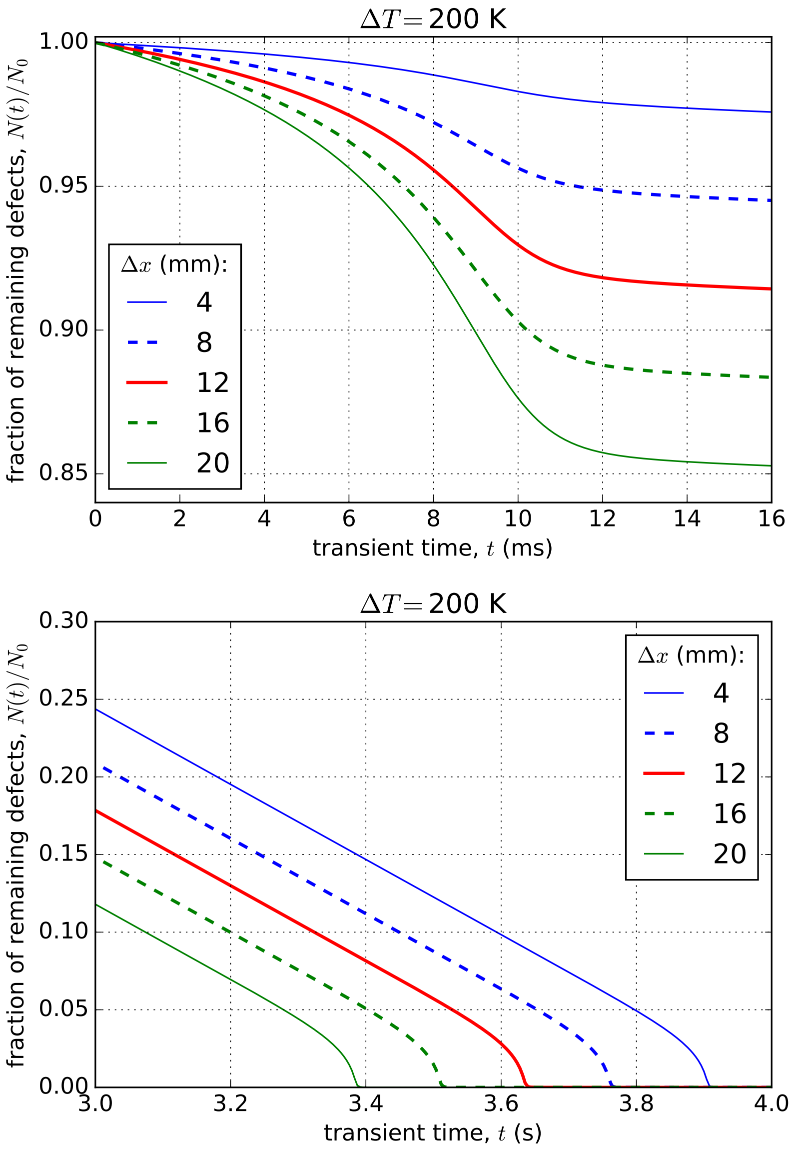

Figure 5.38: A zoom-in of the fraction of remaining defects in the first few milliseconds of the transient(top). A zoom-in of the fraction of remaining defects before the annealing time is reached (bottom).

5.9 The Travelling Wave at High Initial Temperatures

With an increase in the initial temperature of the sample, the rate of spontaneous annealing of defects as well as the rate of heat production, accompanying it, increases. In the case of initiation on a surface (heating of the sample from one side), the developing heterogeneous annealing resembles less and less a travelling wave. And, if the initial temperature is high enough, the annealing time of the initiated annealing approaches the annealing time of the spontaneous one. This seems to be obvious for a sufficiently long sample (the length of which is much greater than the product of the travelling wave velocity and the annealing time of spontaneous annealing). At the same time, in the case of initiated annealing, thermal energy is added to the sample due to surface heating and, in general, spontaneous annealing occurs at elevated temperatures. This means that the annealing time of activated annealing must always be shorter than the time of spontaneous homogeneous annealing. The validity of this statement is obvious under the assumption that the additional activation energy is uniformly "smeared" over the sample, but in reality the temperature distribution for activated annealing is not uniform, as well as the heterogeneous defect annealing and the accompanying heat release.

On the one hand, spontaneous annealing leads to a decrease in the density of defects in the region ahead of the propagating annealing front, and this leads to a decrease in the rate of its propagation. Simultaneously, the temperature increases in this area due to the spontaneous annealing, and this leads to a strong increase in the speed of propagating annealing. Impacts of these two factors, as well as the influence of annealing heterogeneity, are different, non-linear, and difficult to predict. Therefore, a numerical study of the dependence of initiated annealing on the initial temperature of the sample, when spontaneous thermal annealing cannot be neglected, is important. The relevance of the numerical analysis is due to the fact that, due to the non-linearity of the problem, its analytical analysis becomes extremely difficult.

Although we only vary the parameter of initial temperature, in general, the study can be carried out by varying other parameters which may contribute to the damping effect of spontaneous annealing. For example, this can be the sample length which affects the annealing time in the travelling wave regime. In the travelling wave regime the annealing time depends on the length of the sample and the velocity of the wave. Therefore, for sufficiently long sample lengths, the annealing time by means of the travelling wave can extend to long transient times where the spontaneous annealing regime starts to dominate.

The times at which the spontaneous annealing of defects starts to dominate can be determined by the formula for the implicit dependence of the defect density on time (5.5). This scenario was shown before in Figure 5.6 of Section 5.3, where the travelling wave regime of annealing is only realised at transient times that are closer to the annealing time of spontaneous annealing of 13.63 s, when $T_0 = 300\,\mathrm{K}$ and $n_0 = 6.63 \times 10^{26}$ defects/m^3.

When the initial temperature is increased from $T_0 = 300\,\mathrm{K}$ to higher temperatures, the annealing time for spontaneous annealing reduces and the damping effect of spontaneous annealing occurs at earlier times than in the case where $T_0 = 300\,\mathrm{K}$. We study this effect in detail in this section.

We already determined a spontaneous annealing time $t^{\mathrm{a}} = 13.63\,\mathrm{s}$ for initial temperature of $T_0 = 300\,\mathrm{K}$. We increased the initial temperature T_0 from 300 K and determined spontaneous annealing times $t^{\mathrm{a}} = 7.45\,\mathrm{s}$, $t^{\mathrm{a}} = 4.25\,\mathrm{s}$, $t^{\mathrm{a}} = 2.51\,\mathrm{s}$, $t^{\mathrm{a}} = 1.52\,\mathrm{s}$, $t^{\mathrm{a}} = 1.22\,\mathrm{s}$ and $t^{\mathrm{a}} = 0.97\,\mathrm{s}$ for the initial temperatures $T_0 = 310\,\mathrm{K}$, $T_0 = 320\,\mathrm{K}$, $T_0 = 330\,\mathrm{K}$, $T_0 = 340\,\mathrm{K}$, $T_0 = 345\,\mathrm{K}$ and $T_0 = 350\,\mathrm{K}$, respectively, as summarised in Table 5.3. In Table 5.3 we can see that the spontaneous annealing time is about three times bigger than the annealing time of activated heterogeneous annealing in the travelling wave regime when the initial temperature is $T_0 = 300\,\mathrm{K}$, however when the initial temperature is increased to $T_0 = 340\,\mathrm{K}$ the annealing time for activated heterogeneous annealing and spontaneous annealing is about the same. For further increases of $T_0 = 340\,\mathrm{K}$ the annealing times for the activated heterogeneous and spontaneous annealing process monotonously decrease.

Table 5.3: Initial temperature and the corresponding annealing times of the spontaneous homogeneous annealing and the activated heterogeneous annealing.

Initial temperature, T_0 (K)	Annealing time of homogeneous annealing (s)	Annealing time of heterogeneous annealing (s)
350	0.97	0.97
345	1.22	1.22
340	1.54	1.54
330	2.51	2.40
320	4.45	2.91
310	7.45	3.40
300	13.63	3.97

The influence of the initial temperature of the sample can be traced and analysed using Figures 5.39 to 5.45 where we present the development of heterogeneous annealing in a sample of length $L = 13\,\mathrm{cm}$ at a fixed initiating temperature $\Delta T = 300\,\mathrm{K}$ with heating depth $\Delta x = 2\,\mathrm{mm}$. The defect density profiles and corresponding temperature profiles are given on average at regular time intervals ($\Delta t = 0.160\,\mathrm{s}$ for $T_0 = 300\,\mathrm{K}$, $\Delta t = 0.142\,\mathrm{s}$ for $T_0 = 310\,\mathrm{K}$, $\Delta t = 0.125\,\mathrm{s}$ for $T_0 = 320\,\mathrm{K}$, $\Delta t = 0.097\,\mathrm{s}$ for $T_0 = 330\,\mathrm{K}$, $\Delta t = 0.062\,\mathrm{s}$ for $T_0 = 340\,\mathrm{K}$, $\Delta t = 0.05\,\mathrm{s}$ for $T_0 = 345\,\mathrm{K}$, and $\Delta t = 0.042\,\mathrm{s}$ for $T_0 = 350\,\mathrm{K}$).

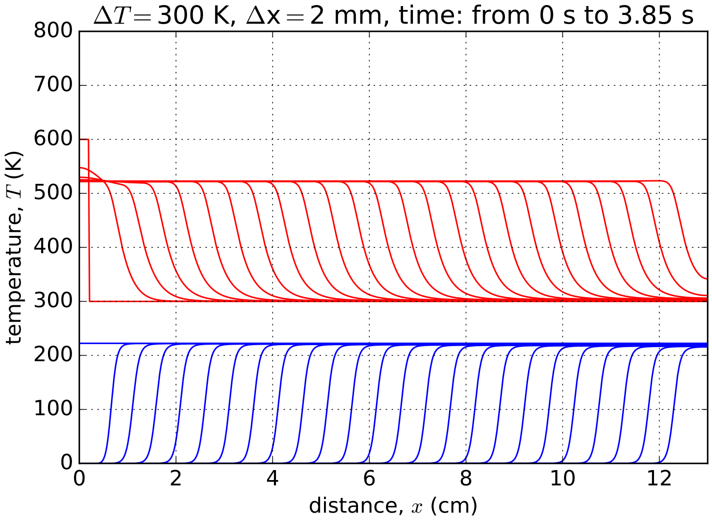

Figure 5.39: The temperature (top) and defect density (bottom) propagation fronts for initiating parameters $\Delta T = 300\,\mathrm{K}$ and $\Delta x = 2\,\mathrm{mm}$ for a maximum time of 3.85 s with regular time intervals between successive profiles of $\Delta t = 0.160\,\mathrm{s}$. The initial temperature is $T_0 = 300\,\mathrm{K}$.

The temperature distribution during heterogeneous annealing for the regime close to travelling wave mode is like a moving step (or step function). The height of the step behind the wave front is constant, the temperature at the front smoothly decreases (at first sharply, then slowly) running to a certain final value. Thereby the un-annealed region is still warmed. The thermal contribution from

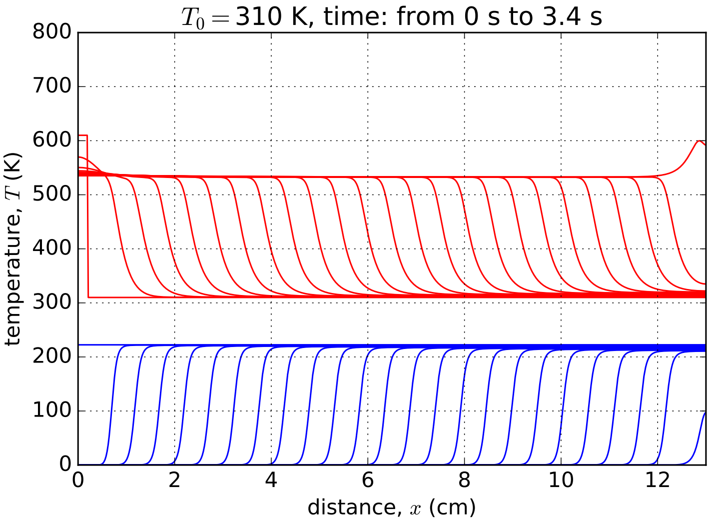

Figure 5.40: The temperature (top) and defect density (bottom) propagation fronts for initiating parameters $\Delta T = 300$ K and $\Delta x = 2$ mm for a maximum time of 3.4 s with regular time intervals between successive profiles of $\Delta t = 0.142$ s. The initial temperature is $T_0 = 310$ K.

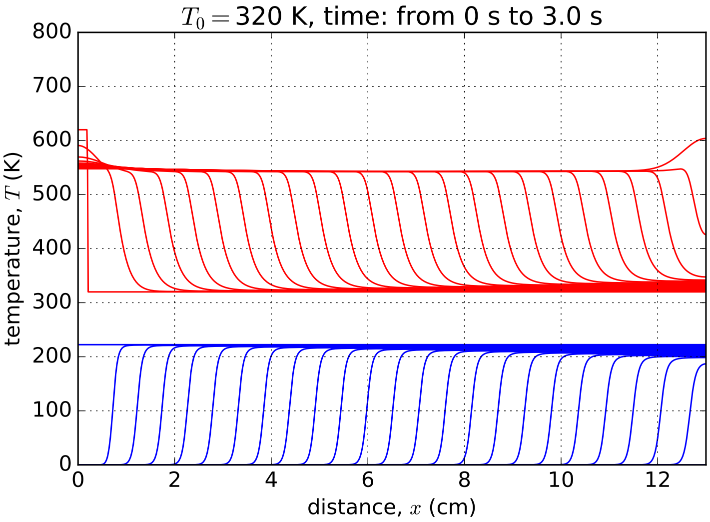

Figure 5.41: The temperature (top) and defect density (bottom) propagation fronts for initiating parameters $\Delta T = 300$ K and $\Delta x = 2$ mm for a maximum time of 3.0 s with regular time intervals between successive profiles of $\Delta t = 0.125$ s. The initial temperature is $T_0 = 320$ K.

the annealed defects, Θ (which depends on the defect density), on the contrary, increases at the wave front from almost zero to some final value. Of course, both the position of the temperature and defect density wave fronts and their propagation speeds coincide.

With increasing T_0, the magnitude of the temperature ahead of the propagation front begins to increase slightly (resulting in a decrease in the temperature gradient ahead of the temperature front), this effect starts to become visible when the initial temperature is increased to $T_0 = 330$ K as shown in Figure 5.42 close to the right boundary. The magnitude of the height of the thermal contribution of the annealed defects, Θ, decreases. The rate of propagation of annealing increases slightly. The slopes of the temperature and defect density profile fronts become less steep as the changes in temperature and density of defects at the wave front tend to zero, and heterogeneous

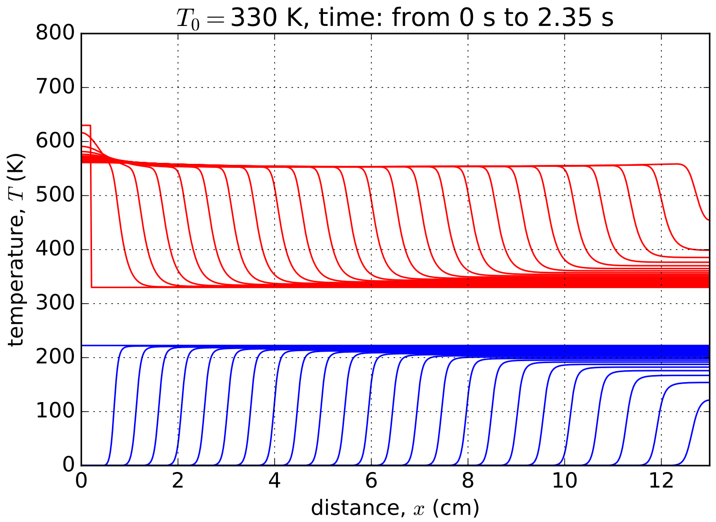

Figure 5.42: The temperature (top) and defect density (bottom) propagation fronts for initiating parameters $\Delta T = 300$ K and $\Delta x = 2$ mm for a maximum time of 2.35 s with regular time intervals between successive profiles of $\Delta t = 0.097$ s. The initial temperature is $T_0 = 330$ K.

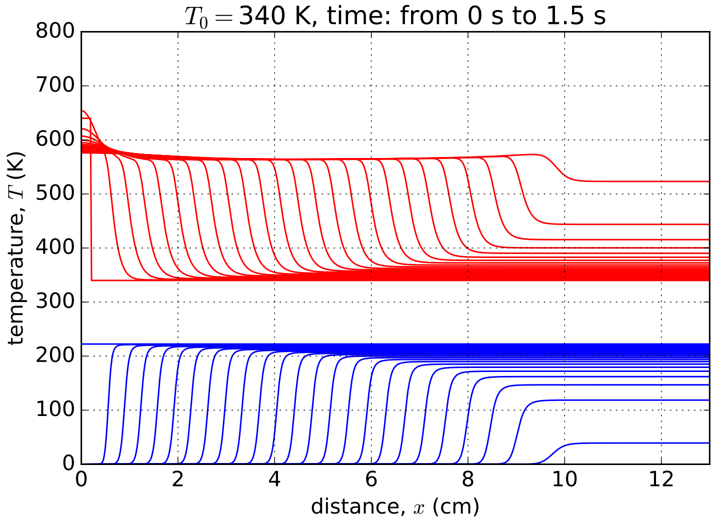

Figure 5.43: The temperature (top) and defect density (bottom) propagation fronts for initiating parameters $\Delta T = 300$ K and $\Delta x = 2$ mm for a maximum time of 1.5 s with regular time intervals between successive profiles of $\Delta t = 0.062$ s. The initial temperature is $T_0 = 340$ K.

annealing resembles more and more a heating of the sample through the heat conduction, when annealing of defects simply follows the change in temperature.

Thus the thermal concentration feedback ceases to be effective and the travelling wave disappears. Therefore, in the un-annealed region of the sample the annealing is almost uniform. For our studied case, this transition from heterogeneous annealing to homogeneous annealing happens most effectively at initial temperatures in the ranges $T_0 = 340$ K to $T_0 = 350$ K when the fraction of defects that were annealed before the arrival of the wave is about 30–35 % for a sample of length $L = 13$ cm as can be seen in Figures 5.43 to 5.45.

If an increase in the initial temperature, T_0, in studied cases, to values 310 K, 320 K and 330 K only causes a slight increase in temperature at the beginning of the front and an increase in the

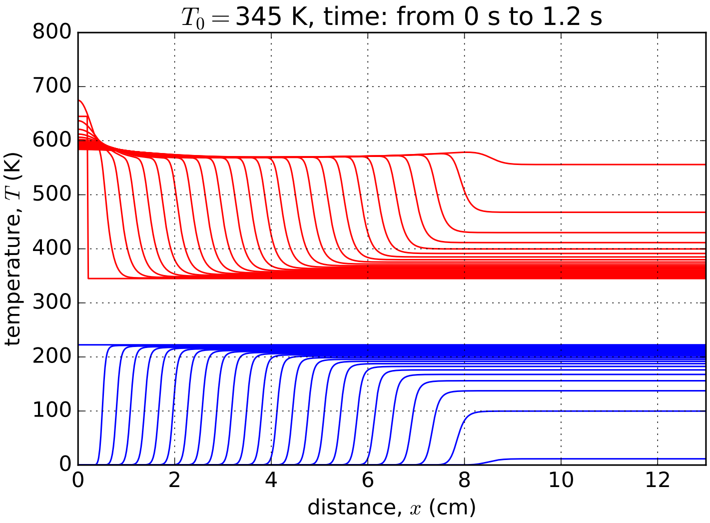

Figure 5.44: The temperature (top) and defect density (bottom) propagation fronts for initiating parameters $\Delta T = 300$ K and $\Delta x = 2$ mm for a maximum time of 1.2 s with regular time intervals between successive profiles of $\Delta t = 0.05$ s. The initial temperature is $T_0 = 345$ K.

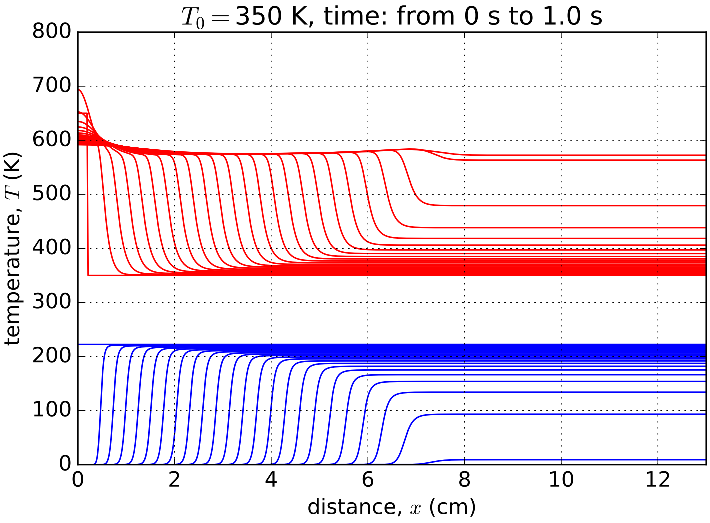

Figure 5.45: The temperature (top) and defect density (bottom) propagation fronts for initiating parameters $\Delta T = 300$ K and $\Delta x = 2$ mm for a maximum time of 1.0 s with regular time intervals between profiles of $\Delta t = 0.042$ s. The initial temperature is $T_0 = 350$ K.

annealing propagation speed, the deformation (or smoothing) of the shape of the temperature distribution (and defect density) becomes prominent at initial temperatures above 340 K, as can be seen by comparing Figures 5.39 to 5.45.

We also modelled the heterogeneous annealing for samples lengths above $L = 13$ cm for the initial temperature of 310 K, with all other control parameters fixed, the results of which are presented in Figures 5.46 to 5.48. It can be seen that with an increase in the sample length, as the travelling wave propagates, the following occurs: the density of defects ahead of the wave front decreases due to spontaneous homogeneous annealing and the travelling wave mode disappears. Of course, an increase of the sample length increases the number of defects in the sample and therefore the percentage of the remaining defects in the sample ahead of the disappearing travelling wave increases as well.

For a sample of length $L = 26$ cm the defects are still effectively annealed in the travelling wave regime, as can be seen in Figure 5.46 (left) which shows the temperature and defect density profiles and Figure 5.46 (right) which shows the fraction of remaining defects for the defect density profiles in Figure 5.46 (left) and compares them with the fraction of remaining defects for the homogeneous (and spontaneous) annealing process.

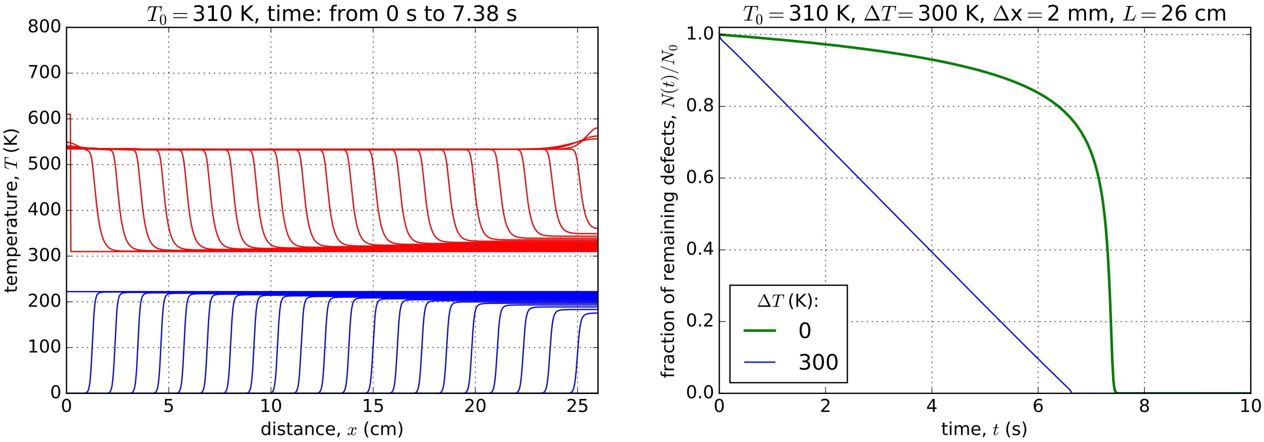

Figure 5.46: The temperature (top) and defect density (bottom) propagation fronts for initiating parameters $\Delta T = 300$ K and $\Delta x = 2$ mm with regular time intervals of $\Delta t = 0.307$ s between successive profiles (left). The corresponding fraction of remaining defects for the heterogeneous and homogeneous (and spontaneous) annealing cases (right). The initial temperature is $T_0 = 310$ K and sample length is $L = 26$ cm.

For sample lengths in the range $L = 39$ cm and $L = 52$ cm, the percentage of remaining defects ahead of the disappearing travelling wave is in the range of about 15 % in Figure 5.47 (left) and 30 % in Figure 5.48 (left), respectively. And this percentage of remaining defects un-annealed by the travelling wave can also be seen in Figures 5.47 (right) and 5.48 (right) which show the time dependence of the fraction of remaining defects (or normalised number of defect) for the defect density profiles shown in Figure 5.47 (left) and Figure 5.48 (left), respectively. Here the time evolution of the fraction of remaining defects in the heterogeneous annealing case deviates from an approximately linear decrease and merges with the time evolution of the fraction of remaining defects in the spontaneous and homogeneous annealing case when approximately 15 % in Figure 5.47 (right) and 30 % in Figure 5.48 (right) of defects remain in the sample.

The results presented in Figures 5.47 and 5.48 show the damping effect of homogeneous (and spontaneous) annealing on the heterogeneous annealing of defects, by means of the travelling wave, when both the initial temperature T_0 and the length of the sample L are increased from our selected base values of $T_0 = 300$ K and $L = 13$ cm.

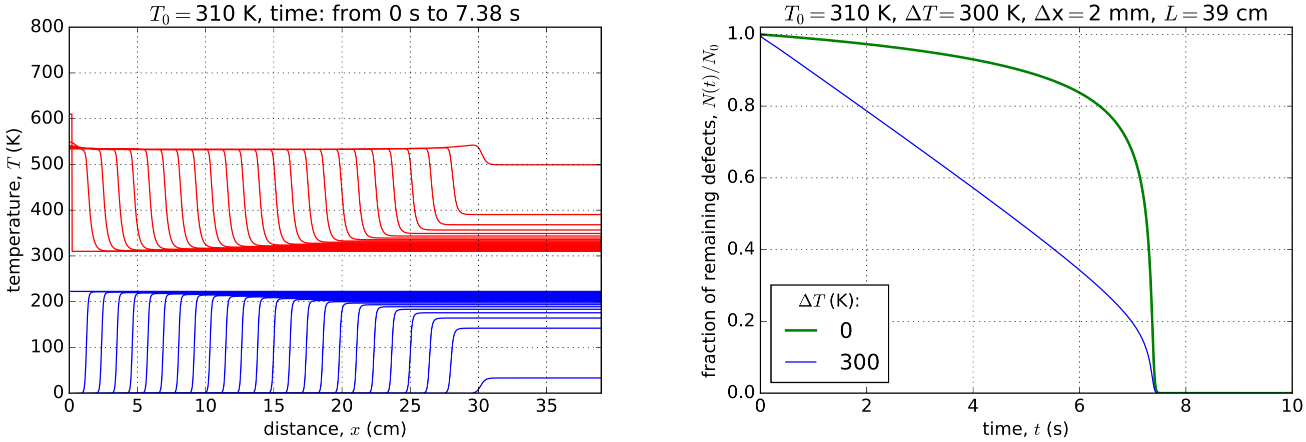

Figure 5.47: The temperature (top) and defect density (bottom) propagation fronts for initiating parameters $\Delta T = 300\,\mathrm{K}$ and $\Delta x = 2\,\mathrm{mm}$ with regular time intervals of $\Delta t = 0.307\,\mathrm{s}$ between successive profiles (left). The corresponding fraction of remaining defects for the heterogeneous and homogeneous (and spontaneous) annealing cases (right). The initial temperature is $T_0 = 310\,\mathrm{K}$ and sample length is $L = 39\,\mathrm{cm}$.

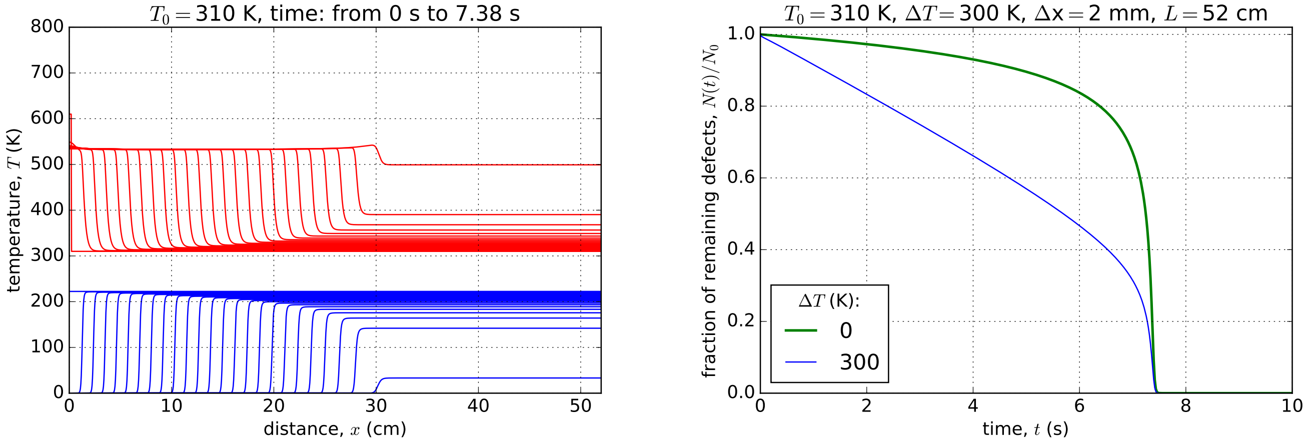

Figure 5.48: The temperature (top) and defect density (bottom) propagation fronts for initiating parameters $\Delta T = 300\,\mathrm{K}$ and $\Delta x = 2\,\mathrm{mm}$ with regular time intervals of $\Delta t = 0.307\,\mathrm{s}$ between successive profiles (left). The corresponding fraction of remaining defects for the heterogeneous and homogeneous (and spontaneous) annealing cases (right). The initial temperature is $T_0 = 310\,\mathrm{K}$ and sample length is $L = 52\,\mathrm{cm}$.

Chapter 6

Conclusion

In this dissertation we studied, by means of numerical simulation, homogeneous and heterogeneous self-sustained annealing of defects of a single type. We carried out numerical calculations using a finite difference scheme to obtain solutions for our coupled PDE problem used to model a self-sustained annealing of defects in a finite geometry. The calculations were carried out for a sample of a length of 13 cm and a uniform initial distribution of defects. We chose a base initial defect density of $n_0 = 6.63 \times 10^{26}$ defects/m^3 and base initial sample temperature $T_0 = 300\,\mathrm{K}$. Different aspects of our problem were investigated by varying the two parameters, n_0 and T_0.

Our simulations have showed that the annealing time decreases (increases) when both n_0 and T_0 are increased (decreased). We found that the annealing time is more sensitive to a change in the initial temperature, T_0, than a change in the initial defect density, n_0. According to our calculations, for our base initial temperature of 300 K, the defects anneal spontaneously with an annealing time of 13.63 s. We verified our numerically calculated solutions for spontaneous self-sustained annealing with the analytical solution found in literature and found both agree very well.

In the case of heterogeneous annealing, where annealing is initiated by adding heat to a localized region of the sample near the left surface, a self-sustained annealing wave, which we call the travelling wave, develops when a sufficient initiating energy is added. The wave travels from the initiation boundary to the opposite (right) boundary. We determined the velocity of the travelling wave from the constant annealing rate of defects in the travelling wave regime. The time of annealing in the travelling wave regime is always less than that of spontaneous homogeneous annealing. The spontaneous annealing of the defects has a damping effect on the travelling wave after some time. The time at which this damping effect dominates is close to the annealing time of spontaneous annealing. For our chosen parameter values of our problem, however, the damping effect becomes negligible even at temperatures a few degrees below 300 K (which is room temperature).

Our numerical study of heterogeneous annealing of defects demonstrates, therefore, the possibility of a self-sustained self-propagating way of annealing of defects in large samples where the common homogeneous annealing of defects is less convenient as the difficulty to maintain a homogeneous distribution of temperature increases. Our simple one dimensional model of heterogeneous annealing gives a strong basis for the study of future models of heterogeneous annealing that may incorporate higher dimensions and more variable parameters.

Bibliography

[1] Jeremiah Lethoba, Pavel M. Bokov, and Pavel A. Selyshchev. A numerical study of heterogeneous annealing in a finite one-dimensional geometry. In *63rd Annual Conference of The South African Institute of Physics*, 2018. (accepted for publication).

[2] Gennady G. Bondarenko. *Radiation physics, structure and strength of solids*. BKL Publishers, Moscow, 2016. (in Russian).

[3] Pavel A. Selyshchev and Pavel M. Bokov. Kinetics of annealing: Basic relationships and nonlinear effects. In Juan F. R. Archilla, Faustino Palmero, M. Carmen Lemos, Bernardo Sánchez-Rey, and Jesús Casado-Pascual, editors, *Nonlinear Systems, Vol. 2: Nonlinear Phenomena in Biology, Optics and Condensed Matter*, pages 283–314. Springer International Publishing, Cham, 2018.

[4] Gary S. Was. *Fundamentals of Radiation Materials Science: Metals and Alloys*. Springer Science & Business Media, Berlin Heidelberg New York, 2007.

[5] F. Kroupa. Dislocation dipoles and dislocation loops. *J. Phys. Colloques*, 27(C3):C3–154–C3–167, 1966.

[6] Zhanbing Yang, Norihito Sakaguchi, Seiichi Watanabe, and Masayoshi Kawai. Dislocation loop formation and growth under in situ laser and/or electron irradiation. *Scientific Reports*, 1:1–4, 11 2011.

[7] Joshua Pelleg. General mechanisms of creep. *Creep in Ceramics*, 241:11–23, 2017.

[8] Sinisa Dj. Mesarovic. Dislocation creep: Climb and glide in the lattice continuum. *Crystals*, 7:243, 08 2017.

[9] A. Seeger. Investigation of point defects in equilibrium concentrations with particular reference to positron annihilation techniques. *Journal of Physics F: Metal Physics*, 3(2):248, 1973.

[10] Naoki Suzuki, Yasuyoshi Nagai, Yoshiko Itoh, Akira Goto, Yasushige Yano, and Toshio Hyodo. Vacancy formation energy for indium determined by a positron annihilation technique. *Phys. Rev. B*, 63, 04 2001.

[11] David J. Bacon and Tomas Diaz de la Rubia. Molecular dynamics computer simulations of displacement cascades in metals. *Journal of Nuclear Materials*, 216:275–290, 1994.

[12] T. Jourdan, G. Bencteux, and G. Adjanor. Efficient simulation of kinetics of radiation induced defects: A cluster dynamics approach. *Journal of Nuclear Materials*, 444(1):298–313, 2014.

[13] Michael W. Thompson. *Defects and Radiation Damage in Metals*. Cambridge University Press, Cambridge, UK, 1969.

[14] C. Tög, P. Hähner, M. Zaiser, and W. Frank. Theory of radiation-induced self-organization of defect structures. *Applied Physics A*, 58(1):11–19, Jan 1994.

[15] V. A. Ivchenko. Atomic structure of cascades of atomic displacements in metals and alloys after different types of radiation. *IOP Conference Series: Materials Science and Engineering*, 110:012003, 02 2016.

[16] Xian-Ming Bai, Arthur F. Voter, Richard G. Hoagland, Michael Nastasi, and Blas Pedro Uberuaga. Efficient annealing of radiation damage near grain boundaries via interstitial emission. *Science*, 327(5973):1631–4, 03 2010.

[17] Stanisław Mrowec. *Defects and Diffusion in Solids: an Introduction*. Elsevier, New York, 1980.

[18] R. A. Adams and C. Essex. *Calculus: A Complete Course*. Pearson, 2003.

[19] William H. Press, Saul A. Teukolsky, William T. Vetterling, and Brian P. Flannery. *Numerical Recipes in C (2nd Ed.): The Art of Scientific Computing*. Cambridge University Press, New York, NY, USA, 1992.

[20] R. O. Weber, G. N. Mercer, H. S. Sidhu, and B. F. Gray. Combustion waves for gases ($\mathrm{Le} = 1$) and solids ($\mathrm{Le} \to \infty$). *Proceedings of the Royal Society of London A: Mathematical, Physical and Engineering Sciences*, 453(1960):1105–1118, 1997.

[21] A. C. McIntosh, R. O. Weber, and G. N. Mercer. Non-adiabatic combustion waves for general lewis numbers: wave speed and extinction conditions. *The ANZIAM Journal*, 46(1):1–16, 2004.

[22] J. F. R. Archilla, J. Cuevas, M. D. Alba, M. Naranjo, and J. M. Trillo. Discrete breathers for understanding reconstructive mineral processes at low temperatures. *The Journal of Physical Chemistry B*, 110(47):24112–24120, 2006.

[23] V. I. Dubinko, P. A. Selyshchev, and J. F. R. Archilla. Reaction-rate theory with account of the crystal anharmonicity. *Phys. Rev. E*, 83:041124, Apr 2011.

[24] Sergej Flach and Andrey V. Gorbach. Discrete breathers – advances in theory and applications. *Physics Reports*, 467(1-3):1–116, 2008.

[25] Francesco Piazza, Stefano Lepri, and Roberto Livi. Cooling nonlinear lattices toward energy localization. *Chaos*, 13(2):637–645, 2003.

[26] R. S. MacKay and Aubry S. Proof of existence of breathers for time-reversible or hamiltonian networks of weakly coupled oscillators. *Nonlinearity*, 7(6):1623–1643, nov 1994.

[27] A. J. Sievers and S. Takeno. Intrinsic localized modes in anharmonic crystals. *Phys. Rev. Lett.*, 61:970–973, Aug 1988.

[28] M. W. Finnis, P. Agnew, and A. J. E. Foreman. Thermal excitation of electrons in energetic displacement cascades. *Phys. Rev. B*, 44:567–574, Jul 1991.

[29] A. E. Volkov and V. A. Borodin. Heating of metals in swift heavy ion tracks by electron–ion energy exchange. *Nuclear Instruments and Methods in Physics Research Section B: Beam Interactions with Materials and Atoms*, 146(1):137–141, 1998.

[30] R. L. Fleisher, P. B. Price, and R. M. Walker. *Nuclear tracks in solids: Principles and applications*. University of California Press, 1975.

[31] V. A. Vasil'ev, Yu. M. Romanovskii, and V. G. Yakhno. Autowave processes in distributed kinetic systems. *Phys. Usp.*, 22(8):615–639, 1979.

[32] Yakov Borisovich Zeldovich, Grigory Isaakovich Barenblatt, V. B. Librovich, and G. M. Makhviladze. *Mathematical theory of combustion and explosions*. Springer US, 1985.

[33] Pavel A. Selyshchev. *Self-organization in radiation physics*. R&C Dynamics, Moscow, Izhevsk, 2008. (in Russian).

[34] Pavel M. Bokov. Finite-dierence method for modelling the self-sustained annealing of radiation defects. Technical Report RRT-FMR-REP-17001, Necsa, 2017.

[35] Robert J. Kee, Linda R. Petzold, Mitchell D. Smooke, and Joseph F. Grcar. Implicit methods in combustion and chemical kinetics modelling. In Jeremiah U. Brackbill and Bruce I. Cohen, editors, *Multiple Time Scales*, chapter 5, pages 113–144. Academic Press, Inc., Orlando, San Diego, New York, London, Toronto, Montreal, Sydney, Tokyo, 1985.

[36] Maplesoft. Maple online help: pdsolve. `https://www.maplesoft.com/support/help/maple/view.aspx?path=pdsolve`. Accessed: 2010-09-30.

[37] R. Courant and D. Hilbert. *Methods of Mathematical Physics*. New York Interscience, 1961.

[38] V. I. Smirnov. *A Course of Higher Mathematics IV: Integral Equations and Partial Differential Equations*. Pergamon Press, 1964.

[39] P. R. Garabedian. *Partial Differential Equations*. John Wiley & Sons, New York, 1964.

[40] E. S. Cheb-Terrab and K. von Bulow. A computational approach for the analytical solving of partial differential equations. *Computer Physics Communications*, 90(1):102–116, 1995.

[41] P. J. Olver. *Applications of Lie Groups to Differential Equations*. Springer–Verlag, 1986.

[42] Willard Miller. *Symmetry and Separation of Variables, Encyclopedia of Mathematics and its Applications*. Addison-Wesley Publishing Company, 1977.

[43] John C. Strikwerda. *Finite Difference Schemes and Partial Differential Equations*. Other Titles in Applied Mathematics. Society for Industrial and Applied Mathematics (SIAM, 3600 Market Street, Floor 6, Philadelphia, PA 19104), 2004.

[44] Eric Jones, Travis Oliphant, Pearu Peterson, et al. SciPy: Open source scientific tools for Python, 2001–. [Online; accessed 2018-06-09].

[45] Nikolay Kyurkchiev and Svetoslav Markov. *Sigmoid Functions: Some Approximation, and Modelling Aspects*. LAP Lambert Academic Publishing, 2015.

[46] Roumen Anguelov and Svetoslav Markov. Hausdorff continuous interval functions and approximations. In *Revised Selected Papers of the 16th International Symposium on Scientific Computing, Computer Arithmetic, and Validated Numerics - Volume 9553*, SCAN 2014, pages 3–13, Berlin, Heidelberg, 2016. Springer-Verlag.

[47] Pavel A. Selyshchev. Propagation of self-reinforcing annealing of radiation defects. In Gennady G. Bondarenko, editor, *Proceedings of the XXIV International Conference Radiation Physics of Solids*, pages 589–594, Moscow, 07–12 July 2014. GNU NII PMT. (in Russian).

[48] Pavel M. Bokov and Pavel A. Selyshchev. Propagating self-sustained annealing of radiation-induced interstitial complexes. *IOP Conference Series: Materials Science and Engineering*, 110(1):012055, 2016.